A few advances in biological modeling and asymptotic analysis

Clair Poignard

université de BORDEAUX

Thèse présentée en vue d'obtenir le diplôme

Habilitation à Diriger des Recherches

École doctorale de Mathématiques et d'Informatique
Spécialité Mathématiques Appliquées et Calcul Scientifique

par

Clair POIGNARD

A few advances in biological modeling and asymptotic analysis
Contribution en modélisation de phénomènes biologiques et en analyse asymptotique

Soutenue le 26 Septembre 2014, après avis favorable des rapporteurs :

M	Thierry	GOUDON,	Directeur de Recherche, Inria Sophia-Antipolis
M	Emmanuel	GRENIER,	Professeur des Universités, Ecole Normale Supérieure de Lyon
M	Roberto	NATALINI,	Dirigente di Ricerca, IAC-CNR

devant le jury suivant :

M	Thierry	COLIN,	Professeur des Universités, Institut Polytechnique de Bordeaux,	Examinateur
M	Frédéric	GIBOU,	Professeur, University of California,	Examinateur
M	Thierry	GOUDON,	Directeur de Recherche, Inria Sophia-Antipolis,	Rapporteur
M	Emmanuel	GRENIER,	Professeur des Universités, Ecole Normale Supérieure de Lyon,	Rapporteur
M	Angelo	IOLLO,	Professeur des Universités, Université de Bordeaux,	Examinateur
M	David	LANNES,	Directeur de Recherche, CNRS,	Examinateur
Mme	Marie-Pierre	ROLS,	Directrice de Recherche, CNRS,	Examinatrice

Remerciements

Tout manuscrit de thèse se doit de commencer par une traditionnelle page de remerciements. Bien que la forme puisse paraître convenue, les remerciements n'en demeurent pas moins sincères!

Je remercierai donc en tout premier lieu Thierry Colin. Merci pour la confiance que tu m'as accordée depuis mon recrutement au sein de l'équipe MC2. Merci au chercheur, que j'admire, merci au chef d'équipe, boute-en-train et plein d'idées, merci aussi de ton amitié. Ce travail te doit beaucoup!

Un grand merci aux rapporteurs de ce manuscrit: Thierry Goudon, Emmanuel Grenier et Roberto Natalini. J'ai été très honoré de l'intérêt que vous avez porté à mon travail. Merci à toi, Roberto pour nos discussions à Rome sur le transport d'ADN, j'espère qu'elles sont les prémices d'une longue collaboration! Je suis très touché que Marie-Pierre Rols et Frédéric Gibou aient accepté de faire partie de mon jury, malgré leur éloignement thématique pour l'une ou géographique pour l'autre. Je suis cependant certain que nos motivations scientifiques nous amèneront à collaborer, dans un futur que j'espère proche! Merci à Angelo Iollo et à David Lannes, deux grands chercheurs que l'IMB a la chance d'avoir, toujours prêts à discuter de sciences et d'autres sujets, d'avoir accepté de siéger dans mon jury.

Ronan, il s'en est passé du temps, depuis les cours de maths sup'! Je me souviens de septembre 2002, quand tu me disais que Michelle Schatzman cherchait un candidat pour une thèse MAPLY-CEGELY de l'époque... Merci à l'ami, merci au collègue, et au scientifique rigoureux : tu as contribué à une grande partie des travaux de cette thèse!

Merci aussi aux membres de l'ANR MEMOVE que j'ai la chance de coordonner. Otared, avec qui j'apprends toujours beaucoup, toujours plein d'idées et d'humour! Les membres du laboratoire de vectorologie physique: Marie et puis Lluis, bien sûr! Toujours enthousiaste, plein d'idées pour comprendre l'électroporation et ouvert à toutes les disciplines. Merci à toi de m'avoir fait découvrir ce phénomène il y a 6 ans, et d'avoir eu la patience d'expliquer à un pauvre mathématicien appliqué la complexité de la biologie et la difficulté des expériences! Il me revient nos discussions autour d'un verre de saké à Kumamoto, d'une bière slovène ou autour d'un hamburger de Nouvelle-Angleterre. A Aude, avec qui j'ai la chance de collaborer, un grand merci pour ta rigueur scientifique, ton ingéniosité et ta bonne humeur permanente! Que les membres du laboratoire Ampère soient sincèrement remerciés aussi : Damien, François, Laurent K et Riccardo, on se connaît depuis 8 ans déjà, mais j'ai toujours besoin de vous pour combler mes lacunes en électromagnétisme!

Je continuerai en remerciant chaleureusement les membres de l'IMB et plus particulièrement Cécile, Charles-Henri, Héloïse, Iraj, Mathieu, Michel, Pierre, Seb et Yves. Un petit clin d'oeil à Thomas, mélomane et éminent goûteur de vin, qui est désormais au TREFLE. Un remerciement spécial à Lisl grâce à qui j'ai pu mieux comprendre les méthodes cartésiennes, toujours avec le sourire malgré mes maniaqueries de stylo rouge!

Olivier, mon désormais compagnon de bureau, que je poursuis jusque dans la salle de gym! Merci pour les missions mémorables, et ton humour pince-sans-rire. Ca fait du bien de voir des chercheurs comme toi, qui ne cherchent pas à plaire, ni à se cacher dans une chapelle, mais seulement à faire de la bonne science, quitte à prendre des risques!

Michelle aimait cette maxime talmudique "*J'ai beaucoup appris de mes maîtres, plus encore de mes collègues, mais c'est de mes élèves que j'ai le plus appris*" : Michael, ce manuscrit et notamment le premier chapitre te doit beaucoup. Tu as su mener à bien ta thèse durant ces 3 ans, toujours avec le sourire et avec brio. Olivier et moi ne nous étions pas trompés il y a 4 ans et demi, lors de ton stage de M1: oui, il fallait te garder, absolument! Suivre au plus près un doctorant comme toi est une chance rare, d'autant plus comme premier élève. Tu as placé la barre très haut, mais je sais qu'Olivier, Thomas, Andjela et Manon sauront

relever le défi!

Julie, tu nous quittes pour d'autres aventures, pas très loin du laboratoire cependant! Je tiens à te remercier pour ces années passées, pour tes qualités scientifiques et ta conscience professionnelle, toujours souriante malgré les coups durs. Le chapitre 2 de ce manuscrit est en grande partie le fruit de ton travail.

La future équipe MONC a la chance de comporter nombre de doctorants et postdoctorants brillants et pleins de bonne humeur. En plus d'Olivier, Thomas et Manon précédemment cités, un grand merci à Etienne, Guillaume, Julien, Marie, Perrine, pour votre contribution non négligeable à une ambiance de travail agréable.

L'essentiel des résultats de ce manuscrit a été obtenu lorsque nous étions ensemble, Emilie: nos chemins de vie se sont désormais éloignés mais je tiens à te remercier du soutien que tu as su m'apporter durant nos années de complicité. J'ai rédigé cette thèse en pensant à ta maman, c'est en partie à elle que je la dédie.

Merci à mes amis, notamment les bordelais danseurs, Elsa, et puis Malia, Raph', Elo et Lolo, Meli, Marion et Edouard, les bordelais chanteurs aussi, notamment les copains d'Orfeo, d'Arpège et d'Easysingers et les copains pongistes Ju, Steste, Greg and co. C'est une chance de vous avoir!

Merci aussi aux "vieux compagnons", Antoine et Nico, amis de presque toujours.

Merci à ma famille, en particulier mes parents à qui je dois presque tout et mon cher frère qui termine ses aventures nippones à cette heure-ci.

Merci enfin à Toi, Chère Elodie: notre rencontre, récente mais si évidente déjà, m'a donné le courage de mener à bien cette seconde thèse. *J'espère m'aventurer longtemps à tes côtés.*

À Michelle, à Evelyne
deux scientifiques de renom, deux femmes d'exception

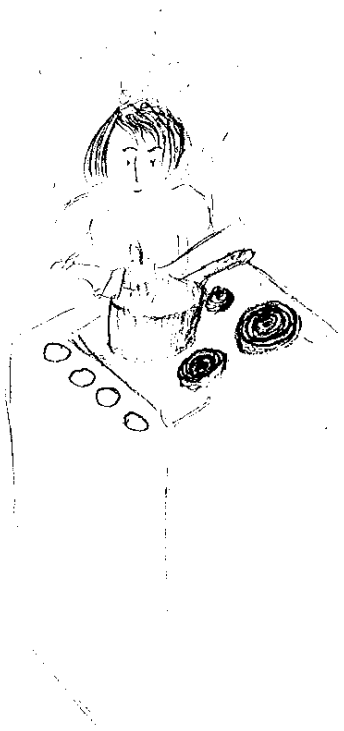

cuisinière destinée à cuire la cuisinière.

23/11/06

Contents

Introduction

Ohne musik wäre das leben ein irrtum

F. Nietzsche

Tanz, tanz sonst sind wir verloren

P. Bausch

This thesis consists of a synthetized presentation of my research in order to get the French diploma "Habilitation à diriger des recherches".

It is organized into four chapters that constitute the four main topics I focused on since I got my permanent position at Inria, in September 2008. These research axes have been developed within the framework of the Inria team MC2, leaded by T. Colin. This thesis is the result of collaborations with colleagues of Bordeaux and elsewhere (Karlsruhe, Lyon, Rennes, Villejuif) as well as with Phd students and postdoctoral fellows I co-supervised. Therefore I choose to use *we* to present the results.

Chapter 1 is devoted to cell electropermeabilization modeling. Electropermeabilization (also called electroporation) is a significant increase in the electrical conductivity and permeability of cell membrane that occurs when pulses of large amplitude (a few hundred volts per centimeter) are applied to the cells: due to the electric field, the cell membrane is permeabilized, and then nonpermeant molecules can easily enter the cell cytoplasm by transport (active and passive) through the electropermeabilized membranes. If the pulses are too long, too numerous or if their amplitude is too high, the cell membrane is irreversibly destroyed and the cells are killed. However, if the pulse duration is sufficiently short (a few milliseconds or a few microseconds, depending on the pulse amplitude), the cell membrane reseals within several tens of minutes: such a reversible electroporation preserves the cell viability and is used in electrochemotherapy to vectorize the drugs into cancer cells. In Chapter 1, I present the modeling we derived in tight collaboration with biologists, namely the L.M. Mir's group at the IGR, which is one of the world's leader in this field, as well as the numerical schemes and the comparisons of the numerical simulations with the experimental data. Interestingly, our modeling that uncouples electric and permeable behaviours of the cell membrane makes it possible to explain the strange observation of cell desensitization, that has been reported very recently by A. Silve *et al.* [100]. This desensitization consists of a less degree of cell permeabilization after a few successive electric pulses than for the same number of pulses but with a delay between each electric pulse delivery. This phenomenon is counter-intuitive and was not predictable by the previous models of the literature.

Chapter II is devoted to cell migration modeling and more precisely to the endothelial cell migration on micropatterned polymers. The goal is to provide models based on the experimental data in order to describe the cell migration on micropatterned polymers. The long–term goal is to provide tools for the optimization of such a migration, which is crucial in tissue engineering. We develop a continuous model of Patlak-Keller-Segel type, which makes it possible to provide qualitative results in accordance with the experiments, and we analyse the mathematical properties of this model. Then, we provide an agent-based model, based on a classical mechanics approach. Strikingly, this very simple model has been quantitatively fitted with the experimental data provided by our colleagues of the biological institute IECB, in terms of cell orientation and cell migration. I conclude the chapter by on-going works on the invadopodia modeling, in collaboration with T. Suzuki from Osaka University and M. Ohta from Tokyo University of Sciences.

Chapter III is devoted to a very recent activity I started in 2013 on tumor growth models, therefore this chapter is based on only one submitted preprint. I present the results on ductal carcinoma growth modeling. Originally confined to the milk duct, these breast cancers may become invasive and agressive after the degradation of the duct membrane, and the main features of our model is to describe the membrane degradation thanks to a non-linear Kedem–Katchalsky condition that describes the jump of pressure across the duct membrane. More precisely, the membrane permeability is given as a non-linear function of specific enzymes (MMPs) that degrade the membrane. We also provide some possible explanation of heterogeneity of tumor growth by modeling the influence of the micro-environment and the emergence of specific cell types.

I eventually conclude by Chapter IV, which consists of a few advances in asymptotics analysis for domains that are singular or asymptotically singular, in the following of my PhD thesis. The results can be split into two parts: first I present approximate transmission conditions through a periodically rough thin layer, and how we characterize the influence of such a layer on the polarization tensor in the sense of Capdeboscq and Voeglius [19]. Then I focus on the numerical treatment of the eddy current problem in domains with corner singularity.

Each chapter is organized into a description of the results, a few perspectives for forthcoming research and a list of the published papers related to the topic of the chapter. Before presenting the results we obtained, I give in the next part a brief summary in French.

Brief summary (in french)

Depuis mon recrutement en septembre 2008 en tant chargé de recherche Inria au sein de l'équipe MC2 commune à l'IMB et Inria et dirigée par T. Colin, j'ai axé mes principales activités de recherche autour de la modélisation de phénomènes non-linéaires issus de la biologie. Trois sujets de biomathématique ont été abordés : la modélisation de l'électroporation, l'étude de la migration cellulaire et la modélisation de la croissance tumorale. La philosophie générale des modèles consiste à partir des expériences et des observations des biologistes pour écrire des équations aux dérivées partielles les plus simples possible permettant d'une part de retrouver les observations expérimentales, et d'autre part d'être prédictif quant à l'évolution du phénomène lorsqu'on ne se place plus dans les conditions des expériences. Il s'agit d'obtenir des modèles rendant compte quantitativement des phénomènes, et pas uniquement qualitativement. L'analyse mathématique des modèles obtenus est effectuée dans la mesure du possible, mais ce n'est pas l'objectif prioritaire. Ainsi toute simplification des modèles est justifiée du point de vue biologique et non pas pour simplifier l'obtention d'un résultat théorique.

En parallèle à ces recherches, dans la suite de ma thèse et de mon postdoctorat, j'ai poursuivi des travaux autour de l'analyse asymptotique de problèmes issus de l'électromagnétisme pour des problèmes à couche mince rugueuse et des problèmes avec des singularités de coins, en collaboration avec M. Dauge, V. Péron et les électromagnéticiens : F. Buret, L. Krähenbühl, R. Perrussel et D. Voyer.

Avec T. Colin, j'encadre actuellement la thèse de M. Leguèbe sur la modélisation de l'électroporation à l'échelle de la cellule qui est en troisième année de thèse et soutiendra très probablement à l'automne 2014. Par ailleurs, en 2009-2010, j'ai encadré le postdoctorat de Victor Péron, Maître de conférences à l'Université de Pau depuis septembre 2010. Depuis 2011 j'encadre Julie Joie, sur la modélisation de la migration cellulaire d'une part puis la modélisation des méningiomes avec T. Colin et O. Saut. Depuis septembre 2013, j'encadre les thèses de T. Michel sur l'étude mathématique de problèmes d'advection pour la cancérologie avec T. Colin et celle d'O. Gallinato sur la modélisation de l'invadopodia, en collaboration avec T. Suzuki l'Université d'Osaka.

Ce chapitre constitue un résumé substantiel en français de mon habilitation à diriger des recherches. Dans la section 1, je présente les travaux que j'ai effectués en modélisation de l'électroporation à l'échelle de la cellule. La section 2 est dédiée à la migration cellulaire, effectuée en collaboration avec l'IECB de Bordeaux. En section 3, je présente la modélisation de la croissance tumorale d'un cancer du sein : le carcinome canalaire est un cancer des cellules endothéliales du canal galactophore qui présente deux formes, la forme *in situ*, qui reste confinée dans le canal mammaire et la forme invasive, qui dégrade la membrane du ductule et envahit les tissus voisins. Nous montrons comment notre modèle permet de décrire ces 2 formes en décrivant la densité d'enzymes dégradant la membrane (les MMPs) et leur action sur la porosité de la membrane du ductule. Enfin, je présente en section 4 les travaux en analyse asymptotique que j'ai poursuivis suite à mes travaux de thèse. Mon projet de recherche autour de la modélisation mathématique de problèmes issus de la biologie est présenté en section 5. Je conclus ce résumé par la liste de mes publications depuis la thèse, classées par thème. Toutes les parties abordées dans ce chapitre sont présentées plus précisément dans les chapitres suivants, écrits en anglais.

1. Modélisation de l'électroporation cellulaire

L'exposition d'une cellule à un champ électrique très intense et très bref (quelques centaines de V/cm pendant quelques dizaines de microsecondes) entraîne une déstructuration de la bicouche lipidique constitutive de la membrane cellulaire. Cette fragilisation de la membrane la rend plus perméable, on parle

d'électroperméabilisation ou encore d'électroporation membranaire. L'introduction de molécules extracellulaires dans le cytoplasme est alors possible [112, 102, 116]. Cette technique de "vectorisation" de molécules dans la cellule est utilisée en électrochimiothérapie, pour le traitement des tumeurs ou pour le transfert de gènes [69, 98]. Cependant le phénomène est mal compris à l'échelle cellulaire. En particulier, le passage de grosses molécules telles que l'ADN à travers la membrane pose de nombreuses questions et une modélisation précise et en accord avec les expériences reste à développer [105].

Le premier chapitre de ce manuscript propose quelques avancées dans la modélisation de l'électroperméabilisation cellulaire. Du point de vue électrique ([39], [40], [42], [101]), la cellule biologique est un milieu électriquement fortement hétérogène essentiellement constitué de deux compartiments supposés électriquement homogènes :

- L'intérieur de la cellule, appelé cytoplasme, dont les dimensions varient de 1 à quelques dizaines de micromètres (μm) suivant les cellules,
- La membrane, elle aussi homogène, dont l'épaisseur est de l'ordre de quelques nanomètres (nm).

Le cytoplasme et le milieu extérieur dans lequel est plongée la cellule sont des milieux ioniques. Les ions leur confèrent une conductivité relativement élevée, de l'ordre de 1 Siemens par mètre (S/m). A l'inverse, la membrane est composée d'une fine bicouche de phospholipides parsemée de protéines, qui en font un matériau diélectrique quasi-isolant : la conductivité de la membrane est de l'ordre de 10^{-7}S/m à 10^{-5}S/m, suivant le type de cellule, sa permittivité est de l'ordre de $10\varepsilon_0$. Ainsi les courants de conduction sont prépondérants devant les courants de déplacement dans le cytoplasme et le milieu extérieur, mais pas dans la membrane, qui se comporte comme une sorte de condensateur en parallèle d'une forte résistance. Du point de vue numérique, pour éviter de mailler la membrane, on la remplace par une interface Γ (*c.f.* figure 1) à travers laquelle on impose des conditions de transmission approchées[1].

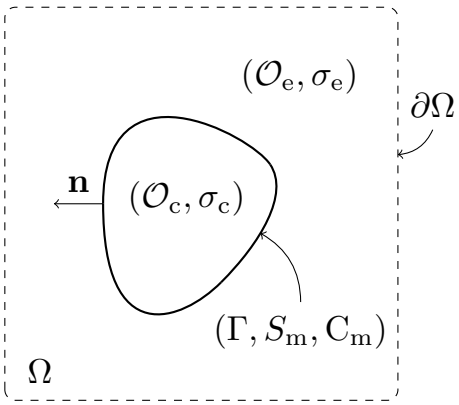

FIGURE 1. Modèle électrique de la cellule. La membrane est d'épaisseur nulle, on note $\mathrm{C_m}$ et S_m sa capacité et sa conductivité surfacique.

En notant $\mathrm{C_m}$ la capacité et S_m la conductivité surfacique de la membrane définies par

$$\mathrm{C_m} = \varepsilon_0 \varepsilon_\mathrm{m}/h, \quad S_\mathrm{m} = \sigma_\mathrm{m}/h,$$

où h est l'épaisseur de la membrane, de l'ordre de quelque nanomètres, le potentiel électrique U vérifie

$$\nabla \cdot (\sigma \nabla U) = 0, \quad \text{dans } \mathcal{O}_\mathrm{e} \text{ et } \mathcal{O}_\mathrm{c}, \tag{1a}$$

avec les conditions de transmission

$$\sigma_\mathrm{c} \partial_n U|_{\Gamma^-} = \sigma_\mathrm{e} \partial_n U|_{\Gamma^+}, \tag{1b}$$

$$\mathrm{C_m} \partial_t [U]_\Gamma + S_\mathrm{m} [U]_\Gamma = \sigma_\mathrm{c} \partial_n U|_{\Gamma^-}, \tag{1c}$$

[1]Une preuve de cette approximation dans le cadre statique est donnée dans [81].

et les conditions initiales et aux limites, par exemple de Dirichlet :

$$U|_{t=0} = V_0, \quad U(t,\cdot) = g, \qquad \text{on } \partial\Omega. \tag{1d}$$

Pour modéliser l'électroporation, Neu et Krassowska [72, 32] ont rajouté un courant d'électroporation $I_{\rm ep}$ à la loi de Kirchoff (1c) :

$$\mathrm{C_m}\partial_t[U]_\Gamma + S_{\rm m}[U]_\Gamma + I_{\rm ep}(t,[U]_\Gamma) = \sigma_{\rm c}\partial_n U|_{\Gamma^-},$$

avec

$$I_{\rm ep} \,:\, (t,\lambda) \longrightarrow I_{\rm ep}(t,\lambda) = i_{\rm ep}(\lambda) N_{\rm ep}(t,\lambda),$$

où $i_{\rm ep}$ est le courant à travers un pore de taille "$r_{\rm m}$", fonction non-linéaire de λ comportant beaucoup de paramètres non-mesurables, et $N_{\rm ep}$ est la densité de pores, qui satisfait à l'équation différentielle suivante :

$$\frac{dN_{\rm ep}}{dt}(t,\lambda) = \alpha e^{(\lambda/V_{\rm ep})^2}\left(1 - \frac{N_{\rm ep}}{N_o} e^{q(\lambda/V_{\rm ep})^2}\right), \quad N|_{t=0} = N_o.$$

Le problème de ce modèle est d'une part qu'il comporte trop de paramètres (environ une dizaine) pour pouvoir être calibré mais surtout la densité de pores $N_{\rm ep}$ n'est pas bornée *a priori*, et donc on peut créer plus de pores qu'il n'y a de place!

Pour éviter cela, avec O. Kavian et M. Leguèbe nous avons développé un modèle *ad hoc* de la conductivité surfacique $S_{\rm m}$ basé sur une analogie avec la modélisation de l'ouverture et la fermeture des canaux ioniques en électrophysiologie. On pose

$$S_{\rm m}(t,\lambda) = \mathrm{S_0} + \mathrm{S_1} X(t,\lambda),$$

où $\mathrm{S_1}$ est la conductivité surfacique de la membrane lorsqu'elle est complètement électroporée : $\mathrm{S_1} \gg \mathrm{S_0}$ et X est une fonction comprise entre 0 et 1 qui vérifie une équation de type "porte coulissante" :

$$\frac{dX}{dt}(t,\lambda) = \begin{cases} (\beta(\lambda) - X)/\tau_{\rm ep}, & \text{if } \beta(\lambda) \geq X, \\ (\beta(\lambda) - X)/\tau_{\rm res}, & \text{if } \beta(\lambda) \leq X, \end{cases}, \quad X|_{t=0} = X_0,$$

où β est une fonction de Heaviside régularisée, par exemple

$$\beta(\lambda) = \frac{1 + \tanh(k_{\rm ep}(|\lambda| - V_{\rm ep}))}{2}, \qquad \text{ou bien} \qquad \beta(\lambda) = \exp\left(-\left(\frac{V_{\rm ep}}{|\lambda|}\right)^{k_{\rm ep}}\right).$$

Les paramètres $\tau_{\rm res}$ et $\tau_{\rm ep}$ sont les temps caractéristiques respectivement de la fermeture et de l'ouverture de la porte X. On est donc passé d'un modèle à une dizaine de paramètres à un modèle à 4 paramètres. Par ailleurs, en récrivant le problème sur la surface Γ à l'aide des opérateurs de Steklov-Poincaré, on a démontré l'existence et l'unicité (*c.f.* Thm 10 de [56]) des solutions aux problèmes non-linéaires statique et dynamique.

Pour résoudre numériquement le problème, avec L. Weynans nous avons utilisé une méthode de différences finies d'ordre 2 sur une grille cartésienne, inspirée de la méthode de M. Cisternino et L. Weynans [22] développée au sein de l'équipe. L'interface de la cellule est repérée par une technique de fonction level-set. Loin de l'interface, une discrétisation classique centrée du second ordre pour le laplacien est utilisée. Lorsque l'interface coupe la grille par exemple entre les points M_{ij} et M_{i+1j}, on introduit le point d'interface $I_{i+1/2,j}$ commun au segment $[M_{ij}, M_{i+1j}]$. En ce point, on rajoute deux inconnues correspondant à la trace du potentiel du côté cytoplasme $\tilde{u}^{\rm c}_{i+1/2\,,j}$ et du côté milieu extérieur $\tilde{u}^{\rm e}_{i+1/2\,,j}$. Un exemple de la méthode de discrétisation est donné en figure 2. Un stencil de 5 points est utilisé aux points d'interface, comme indiqué en figure 2(a). Par exemple, on calcule le flux en $I_{i+1/2j}$ comme suit

$$\frac{\partial U}{\partial x}(\tilde{x}, y_j) \approx \frac{(u_{i-1j} - \tilde{u}^{\rm e}_{i+1/2\,,j})(x_i - \tilde{x})}{h_x(x_{i-1} - \tilde{x})} - \frac{(u_{ij} - \tilde{u}^{\rm e}_{i+1/2\,,j})(x_{i-1} - \tilde{x})}{h_x(x_i - \tilde{x})}, \tag{2}$$

où $\tilde{x}_{i+1/2\,,j}$ est remplacé par $\tilde{x}$. Notons que dans la dérivée suivant y ne peut pas être obtenue similairement car il n'y a pas de point de grille aligné avec l'interface. On utilise une combinaison linéaire de $(\partial_y U)_{ij}$ et de $(\partial_y U)_{i-1j}$:

$$\frac{\partial U^{\rm e}}{\partial y}(\tilde{x}, y_j) \quad \approx \quad \frac{\tilde{x} - x_{i-1}}{h_x}\,(\partial_y U)_{ij} - \frac{\tilde{x} - x_i}{h_x}\,(\partial_y U)_{i-1j}. \tag{3}$$

Le schéma est stabilisé en utilisant un stencil shifté si 2 points d'interface sont impliqués dans la même discrétisation du flux comme indiqué en figure 2(c). Dans sa thèse, M. Leguèbe a développé un code 2D et

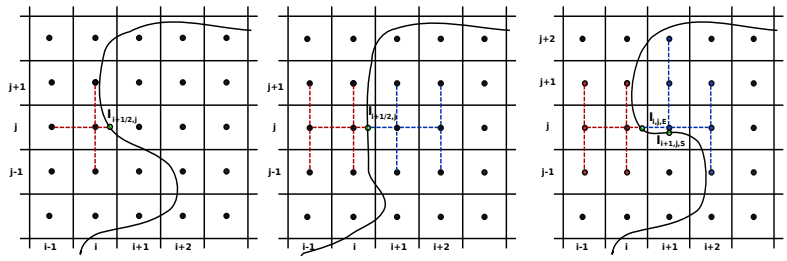

(a) Discrétisation du laplacien sur les points d'interface.

(b) Discrétisation de ∇U à l'interface : stencil non-stabilisé.

(c) Discrétisation de ∇U à l'interface : stencil stabilisé.

FIGURE 2. Discrétisations du laplacien et des gradients de U à l'interface.

3D en C^{++} basé sur la librairie eLyse développée au sein de l'équipe, permettant de simuler le modèle. Il a été testé sur différentes géométries de cellules, et donne des résultats qualitativement similaires au modèle de Krassowska et Neu avec beaucoup moins de paramètres pour les millipulses et micropulses. En outre, pour les pulses plus courts (de l'ordre de la nanoseconde) les résultats obtenus sont en accord avec les expériences à la différence du modèle de Krassowska et Neu. Ce point est détaillé en partie 3.5.b du Chapitre I.

Grâce à ce nouveau modèle, une calibration quantitative avec les expériences est envisageable. Un premier travail avec les expériences de patch-clamp du Karlsruhe Institute for Technology a été fait pendant le stage de Master 1 de F. Chaouqi (*c.f.* Chapitre I–subsubsection 3.5.a).

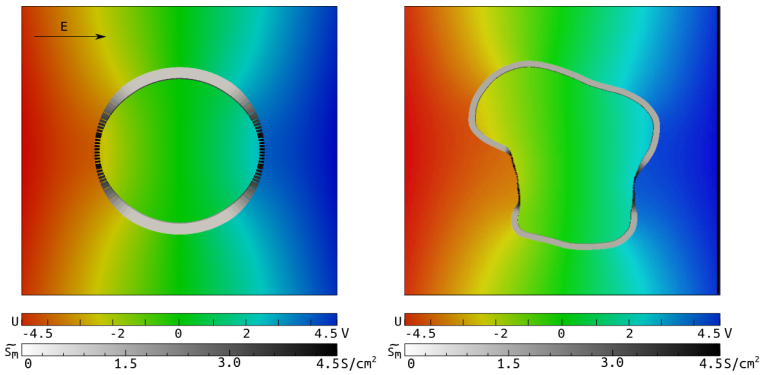

(a) Potentiel électroquasistatique pour une cellule circulaire.

(b) Potentiel électroquasistatique pour une cellule de forme non convexe.

FIGURE 3. Solution du potentiel U pour deux cellules de formes différentes à $t = 100$ μs. La figure 3(b) montre que la zone électroporée dépend de l'orientation du champ électrique et de la forme de la cellule.

Enfin nous avons développé un modèle d'électroporation décrivant la perméabilité de la cellule. Cette approche consiste à rajouter au modèle électrique de la cellule un modèle de transport des molécules à l'extérieur et dans la cellule qui tient compte du degré de perméabilité de la membrane cellulaire. Cette perméabilité est augmentée par l'application du champ électrique mais le temps caractéristique de l'état de haute perméabilité est plus long que la durée de l'état de haute conductivité, ce qui permet d'expliquer à la fois le caractère transitoire de l'état conducteur des membranes (quelques microsecondes selon les travaux

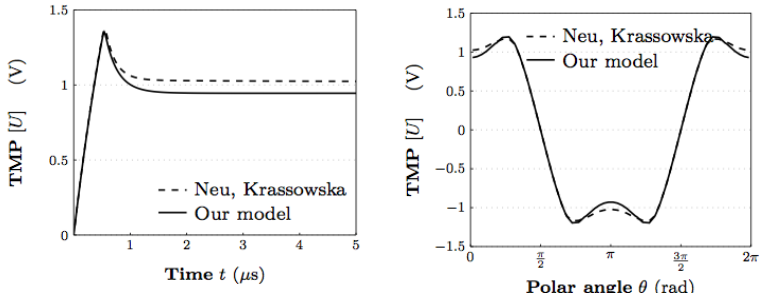

(a) Evolution du ΔTMP au pôle de la cellule.

(b) Valeurs du ΔTMP après 100 μs.

FIGURE 4. Comparaisons des modèles pour une cellule circulaire : les lignes continues sont les résultats de notre modèle, et les lignes pointillées sont obtenues avec le modèle de Neu, Krassowska (*c.f. [56]*).

de Zimmermann *et al.* [9]) et la longue durée de l'état perméable des membranes, plusieurs minutes comme observé par L.M. Mir [71]. Cette partie est précisément décrite en Section 4.2 du Chapitre I.

2. Modèles de migration cellulaire

Depuis 2011, avec T. Colin et O. Saut, je me suis intéressé à la migration cellulaire à travers une collaboration avec M.C. Durrieu de l'IECB de Bordeaux, pendant le postdoctorat de J. Joie. L'objectif est de décrire la migration de cellules endothéliales sur des surfaces striées avec des polymères bioactifs afin d'optimiser cette migration en jouant sur l'épaisseur des stries et leur espacement.

2.1. Modèle macroscopique continu. Nous avons tout d'abord écrit un modèle macroscopique continu décrivant l'évolution des cellules sur la surface considérée. Le modèle est de type Patlak-Keller-Segel pour décrire le phénomène de chimiotaxie. La particularité est que le comportement des cellules est très différent suivant qu'elles ont adhéré ou non au substrat de polymères :

- En dehors du substrat les cellules semblent s'attirer entre elles, probablement grâce à un chimioattractant qu'elles produisent.
- Dès qu'elles sont sur le substrat, elles semblent y être piégées : elles se déplacent plus lentement et uniquement sur la zone de polymères.

Nous avons donc considéré un domaine Ω composé du domaine avec polymères $\widetilde{\Omega}$ et du milieu sans polymère $\Omega \setminus \widetilde{\Omega}$. Deux populations de cellules sont utilisées : l'une, notée u_1 , se déplace dans tout le domaine Ω, et l'autre, notée u_2, a son domaine de définition égal à $\widetilde{\Omega}$. Le passage de u_1 vers u_2 est décrit par la pénalisation $\lambda \mathbb{1}_{\widetilde{\Omega}} u_1(1-u_2)$. Le chimioattractant produit par les cellules pour s'attirer entre elles est noté v et est régi par une équation de diffusion classique avec terme source et dégradation. Le système s'écrit

$$\partial_t u_1 = d_1 \Delta u_1 - \lambda \mathbb{1}_{\widetilde{\Omega}} u_1(1-u_2) - \nabla.\left(\chi(u_1,v) u_1 \nabla v\right), \qquad \text{in } \Omega, \tag{4a}$$

$$\partial_t u_2 = d_2 \Delta u_2 + \lambda \mathbb{1}_{\widetilde{\Omega}} u_1(1-u_2), \qquad \text{in } \widetilde{\Omega}, \tag{4b}$$

$$\partial_t v = \Delta v - \eta v + \gamma_1 u_1 + \gamma_2 u_2, \qquad \text{in } \Omega, \tag{4c}$$

avec les conditions de Neumann homogènes aux bords des domaines

$$\partial_{\mathbf{n}} u_1|_{\partial\Omega} = 0, \quad \partial_{\mathbf{n}} u_2|_{\partial\widetilde{\Omega}} = 0, \quad \partial_{\mathbf{n}} v|_{\partial\Omega} = 0, \tag{4d}$$

et les conditions initiales $(u_1^0, u_2^0, 0)$:

$$u_1|_{t=0} = u_1^0, \quad u_2|_{t=0} = u_2^0, \quad v|_{t=0} = 0. \tag{4e}$$

En utilisant les propriétés du noyau de la chaleur étendues à un domaine borné (*c.f.* Proposition 1. [27]), nous avons démontré l'existence globale et l'unicité de la solution du système différentiel ci-dessus (*c.f.* Thm 2.1. [27]) pour $(u_1^0, u_2^0) \in L^\infty(\Omega) \times L^\infty(\widetilde{\Omega})$. Par ailleurs, les simulations numériques effectuées avec la librairie eLyse nous ont permis de prédire deux faits observés expérimentalement :

- Etant donnée une surface du milieu bioactif, le processus de migration est plus efficace avec un grand nombre de fines bandes de polymères qu'avec un petit nombre de larges bandes.
- La quantité de cellules initialement présentes sur le principe actif est un facteur déterminant de la vitesse de migration vers le polymère.

2.2. Modèle discret de migration. Afin d'utiliser au mieux les données expérimentales disponibles, pour avoir des résultats quantitativement en accord avec les expériences, et pas seulement qualitativement comme le modèle continu, nous avons écrit un modèle discret de migration.

Le système différentiel est décrit dans [54] : chaque cellule est une ellipse de grand axe Λ et de petit axe λ. Pour éviter de décrire le changement de forme pendant la migration, les axes Λ et λ sont fixes et mesurés à la fin de l'expérience. Nous décrivons la position M_i de chaque cellule i suivant une variante de la loi de Newton, en faisant le bilan des forces auxquelles est soumise chaque cellule :

- Une attraction de longue portée F_c entre les cellules, générée par le chimioattractant,
- Une répulsion de faible distance pour éviter que les cellules ne se chevauchent,
- Une force de friction F_f, qui décrit l'adhérence de chaque domaine : le substrat est nettement plus adhérent que le domaine sans polymère,
- Une force d'attraction F_a du patch, qui attire la cellule dès que celle-ci a commencé à le toucher, ceci traduit l'attraction des cellules pour les nutriments.

Nous avons décrit aussi l'orientation de chaque cellule, selon 3 phénomènes :

- L'alignement le long du champ de vitesse de la cellule,
- L'alignement de chaque cellule suivant l'orientation de ses voisins,
- L'orientation des cellules du patch le long de la tangente au domaine patché, pour maximiser la surface en contact avec le polymère.

Qualitativement, nous retrouvons le fait que pour une aire totale de polymères donnée, la migration est meilleure pour un grand nombre de patches fins. Le résultat marquant de ce travail est qu'avec un jeu de paramètres bien choisi, nous avons réussi à obtenir des résulats quantitativement en accord avec les mesures sur l'orientation des cellules suivant la largeur des patches.

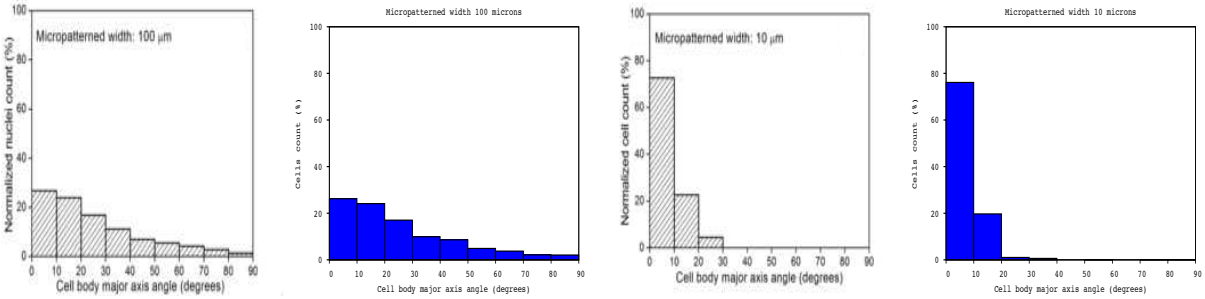

(a) 100 μm experiments (b) 100 μm simulations (c) 10 μm experiments (d) 10 μm simulations

FIGURE 5. Alignement des cellules sur des bandes de 100μm et 10μm. Les simulations et les expériences sont quantitativement similaires [54].

3. Modélisation de la croissance tumorale

Depuis 2013, je me suis intéressé à la modélisation de la croissance tumorale, en collaboration avec T. Colin et O. Saut. Dans le cadre de la thèse d' O. Gallinato, nous nous sommes intéressés à la modélisation du carcinome canalaire, une forme particulière du cancer du sein.

La particularité de ce cancer est qu'il est initialement confiné dans les canaux galactophores, on parle de DCIS pour ductal carcinoma in situ. Cependant certains types de carcinome canalaire produisent des enzymes qui dégradent la membrane du canal galactophore (MMPs) et le cancer devient invasif, on parle de IDC (Invasive Ductal Carcinoma).

Le modèle est subdivisé est 3 sous-partie, comme décrit en figure 6. Le sous-modèle central décrit

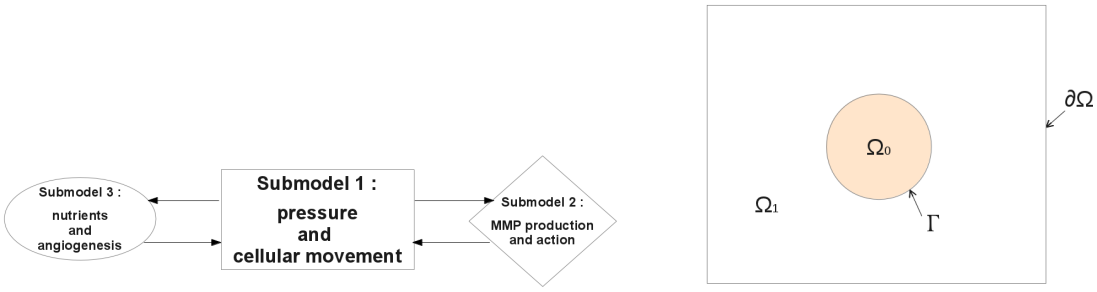

(b) Geometry

FIGURE 6. Schema de la structure du modèle.

l'influence de la tumeur sur le tissu environnant. En raison de la prolifération tumorale, une pression est exercée, qui entraîne un déplacement des densités cellulaires P, N, S et L, respectivement pour cellules proliférantes, nécrotiques, saines et cellules du lumen. Dans la même veine que les travaux de Bresch, Colin, Grenier, Saut et Ribba [92, 14, 15], on écrit dans le domaine Ω de la figure 6(b) :

$$\partial_t P + \nabla \cdot (\mathbf{v}P) = (\alpha_P - \alpha_N)P, \tag{5a}$$

$$\partial_t N + \nabla \cdot (\mathbf{v}N) = \alpha_N P, \tag{5b}$$

$$\partial_t S + \nabla \cdot (\mathbf{v}S) = 0, \tag{5c}$$

$$\partial_t L + \nabla \cdot (\mathbf{v}L) = 0, \tag{5d}$$

où les taux de prolifération et de nécrose α_P et α_N dépendent de la quantité de nutriments Θ et de la pression Π dont dérive la vitesse v :

$$\alpha_P = \alpha\, f_P, \qquad \alpha_N = \alpha\, f_N,$$

avec

$$f_P(\Theta, \Pi) = \alpha_G \frac{1 + \tanh\left[\Lambda_P(\Theta - \Theta_H)\right]}{2} \frac{\Pi^{max} - \Pi}{\Pi^{max}},$$
$$f_N(\Theta) = \frac{1 - \tanh\left[\Lambda_N(\Theta - \Theta_N)\right]}{2}.$$

la particularité de la modélisation réside dans la description de la pression, qui présente une discontinuité à travers la membrane du ductule. Ceci ce traduit par une condition de transmission de type Kedem-Katchalsky :

$$-\nabla \cdot (k\nabla\Pi) = \alpha_P P \qquad \text{in} \quad \Omega_0 \cup \Omega_1, \tag{6}$$

$$[\![k\partial_n \Pi]\!] = 0, \tag{7}$$

$$\kappa_m [\![\Pi]\!] = k\partial_n \Pi|_{\Gamma^+}, \tag{8}$$

$$\Pi|_{\partial\Omega} = 0, \tag{9}$$

où

- La perméabilité domaine dépend des densités cellulaires :
$$k = k_L L + k_S S + k_N N + k_P P,$$
- κ_m représente la perméabilité surfacique de la membrane.

L'idée est de faire dépendre cette perméabilité membranaire de quantité de MMPs produite :

$$\kappa_m(t,x) = \kappa^0 + (\kappa^{max} - \kappa^0) \sup_{s\in[0,t]} \left(\frac{1 + \tanh\left[\Lambda_M (M(s,x) - M_{th})\right]}{2} \right),$$

où

- κ^0 est la perméabilité membranaire lorsque la membrane est intacte,
- κ^{max} représente la perméabilité de la membrane dégradée,
- Λ_M est la pente pour passer de l'état intact à l'état dégradé,
- M_{th} est le seuil de MMPs nécessaire pour dégrader la membrane.

La concentration M de MMPs satisfait une équation de réaction–diffusion dont le terme source est proportionnel à la densité de cellules proliférantes.

La quantité de nutriments est régie par une équation de Poisson à l'extérieur du ductule :

$$\begin{aligned} &-\nabla \cdot (D_\theta \nabla \Theta) = S_{angio} + S_{memb} - \lambda \alpha_P P \Theta, \qquad \text{on} \quad \Omega, \\ &\Theta|_{\partial\Omega} = 0, \quad \partial_n \Theta|_{\partial\Omega} = 0, \end{aligned}$$

tandis que dans le ductule on impose

$$\Theta(x) = \begin{cases} \Theta|_\Gamma \, \exp\left(-\frac{\text{dist}(x,\Gamma)}{\delta_0 - \text{dist}(x,\Gamma)} \right), & \text{if dist}(x,\Gamma) < \delta_0, \\ 0, & \text{otherwise,} \end{cases}$$

ce qui permet d'éviter de considérer une diffusion non-linéaire difficile à paramétrer. Le point faible de ce genre de modèle est qu'il a tendance à donner des résultats trop symétriques par rapport aux observations et il ne peut tenir compte de l'hétérogénéité de la croissance tumorale, à moins d'introduire un biais peu réaliste dans les données initiales. Pour pallier à cela, nous avons modélisé l'influence du microenvironnement et plus particulièrement le rôle des fibroblastes qui produisent eux aussi des MMPs sous l'action d'un signal chimique Z produit par les cellules cancéreuses, comme schématisé en figure 7(a). Nous avons donc divisé

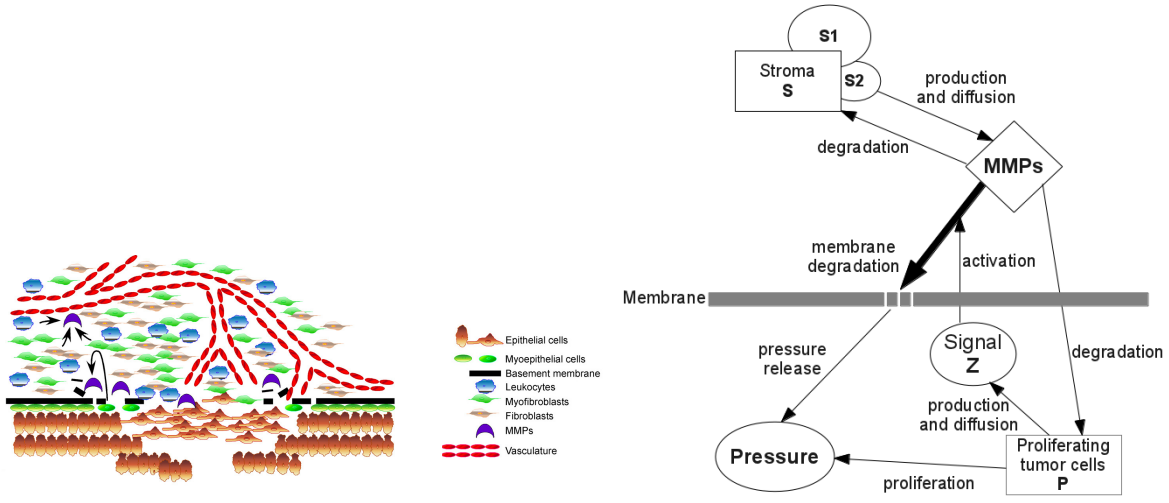

(a) Role of stroma in membrane degradation

(b) Schematic diagram of MMP production

FIGURE 7. Rôle du stroma dans la production de MMP, et schéma de la modélisation [49].

la population des cellules saines en 2 sous-populations : une population S_1 qui ne produit pas de MMP, et

une population S_2 qui correspond aux fibroblastes :

$$\begin{aligned}
&\partial_t S_1 + \nabla \cdot (\mathbf{v} S_1) = 0,\\
&\partial_t S_2 + \nabla \cdot (\mathbf{v} S_2) = 0,\\
&S = S_1 + S_2.
\end{aligned}$$

L'équation sur les MMP est alors remplacée par

$$\begin{aligned}
&\partial_t M - \nabla \cdot (D_M \nabla M) = \gamma S_2 - \mu M,\\
&\partial_t Z - \nabla \cdot (D_M \nabla Z) = \alpha_z P - \mu Z,\\
&Z|_{t=0} = 0, \quad M|_{t=0} = 0, \quad Z|_{\partial\Omega} = 0, \quad M|_{\partial\Omega} = 0
\end{aligned}$$

où

$$\gamma(Z) = \alpha_M \left(\frac{1 + \tanh\left[\Lambda_z (Z - Z_{th})\right]}{2} \right).$$

En partant de conditions initiales S_2^0 distribuées aléatoirement autour du ductule, nous avons obtenu la figure 8(a), qui montre un point de rupture de la membrane très localisé, qui est en accord avec les observations. A la fin de cette section, d'autres sources possibles d'hétérogénéité sont présentées, comme la production de

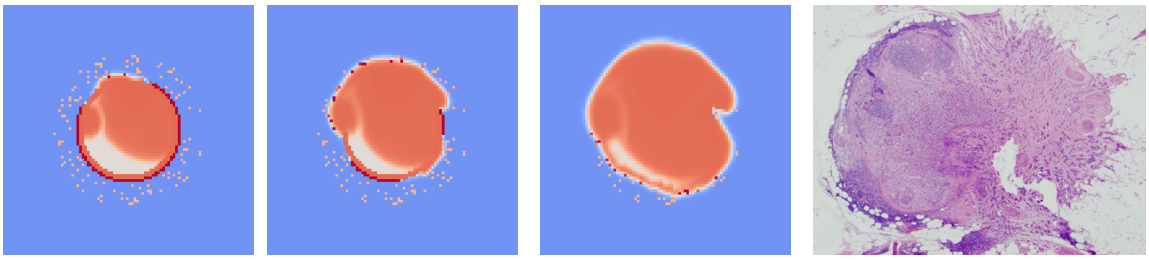

(a) $t = 11$ (b) $t = 12$ (c) $t = 13$ (d) Biopsie [75]

FIGURE 8. Modèle amélioré du carcinome canalaire invasif.

TNF, où l'existence de différents types de cellules cancéreuses (l'un produisant des MMPs, l'autre pas). Ce chapitre se conclut par les travaux en cours sur l'étude mathématique d'un modèle simplifié de croissance tumorale d'une part et la modélisation à partir de l'imagerie médicale de la croissance d'une métastase d'un GIST située au foie.

4. Analyse asymptotique de problèmes issus de l'électromagnétisme

Par ailleurs, j'ai poursuivi mes travaux en analyse asymptotique pour le problème de conductivité d'une part, et le problème des courants de Foucault d'autre part, dans des milieux singuliers ou asymptotiquement singuliers.

4.1. Transmission à travers une couche mince rugueuse pour le problème de conduction. L'objectif de ce travail est d'une part de caractériser la transmission du potentiel électrostatique à travers une couche mince rugueuse (voir figure 9(a)), en la remplaçant par des conditions de transmission adéquates. D'autre part, il s'agit de caractériser explicitement le tenseur de polarisation généralisé, introduit par Y. Capdeboscq et M. Vogelius [19], qui permet de décrire l'influence d'une inhomogénéité sur le potentiel électrique loin de cette inhomogénéité.

En paramétrisant par Ψ la courbe Γ, on décrit Γ^α à l'aide d'une fonction "épaisseur" périodique[2] f :

$$\Gamma_\varepsilon^\alpha = \partial \mathcal{D}_\varepsilon^m \setminus \Gamma = \left\{ \Psi(\theta) + \varepsilon f(\theta/\varepsilon^\alpha) n(\theta), \quad \theta \in \mathbb{T} \right\},$$

[2]On peut étendre les résultats à une fonction quasi-périodique. Le cas d'une rugosité aléatoire n'a pas été considéré.

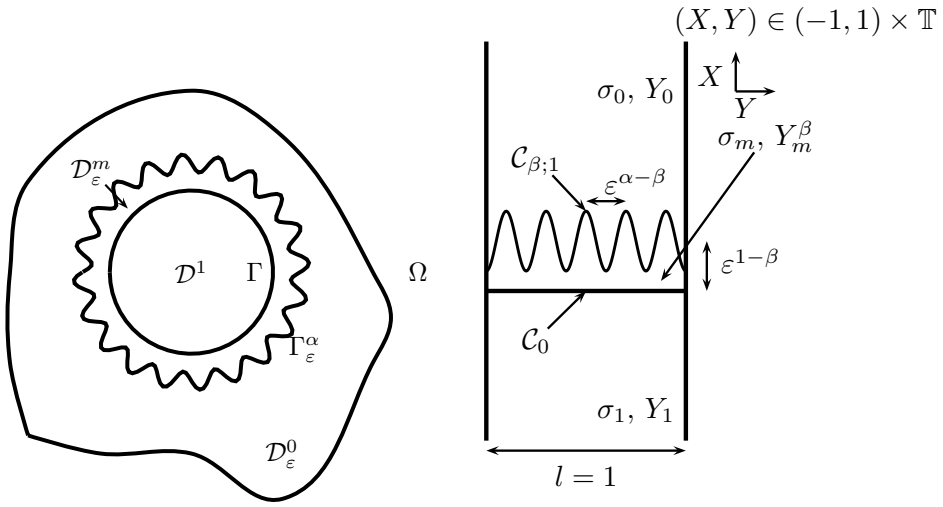

(a) Géometrie du problème

(b) Bande infinie de largeur 1. $\beta = \min(1, \alpha)$.

ε représente l'épaisseur de la membrane, et le paramètre α mesure le degré de rugosité. La carte de conductivité du domaine perturbé σ^ε et du domaine non-perturbé σ sont données par

$$\sigma^\varepsilon(z) = \begin{cases} \sigma_1, \text{ if } z \in \mathcal{D}^1, \\ \sigma_m, \text{ if } z \in \mathcal{D}^m_\varepsilon, \\ \sigma_0, \text{ if } z \in \mathcal{D}^0_\varepsilon, \end{cases} \qquad \sigma(z) = \begin{cases} \sigma_1, \text{ if } z \in \mathcal{D}^1, \\ \sigma_0, \text{ if } z \in \mathcal{D}^0, \end{cases}$$

où σ_1, σ_m et σ_0 sont strictement positives. Pour g assez régulière sur $\partial\Omega$, on définit u^ε et u^0 par :

$$\nabla \cdot (\sigma^\varepsilon \nabla u^\varepsilon) = 0, \text{ in } \Omega, \tag{10a}$$
$$u^\varepsilon|_{\partial\Omega} = g, \tag{10b}$$
$$\nabla \cdot \left(\sigma \nabla u^0\right) = 0, \text{ in } \Omega, \tag{11a}$$
$$u^0|_{\partial\Omega} = g. \tag{11b}$$

Une simple estimation d'énergie nous montre que lorsque g est dans $H^{1/2}(\partial\Omega)$, u^ε converge en norme H^1 vers u^0. Pour construire les termes suivants du développement asymptotique de u^ε, en posant $\beta = \min(1, \alpha)$, il est utile de construire des correcteurs de couche limite définis dans une bande infinie de taille 1, figure 9(b). La construction de ces correcteurs se fait similairement à celle de Allaire et Amar [3], en faisant attention à ce que les problèmes des correcteurs soient bien posés : il faut en effet introduire les moyennes des traces des fonctions oscillantes qui appraîssent pour définir la correction loin de la membrane, pour que les correcteurs soient bien définis.

Le résultat principal de ces travaux est que l'on a la formule de représentation suivante :

$$u^\varepsilon(y) - u^0(y) = \varepsilon(\sigma_m - \sigma_0) \int_\Gamma \mathcal{M}_\alpha \begin{pmatrix} \partial_n u^0 \\ \nabla_\Gamma u^0 \end{pmatrix} \cdot \begin{pmatrix} \partial_n G \\ \nabla_\Gamma G \end{pmatrix} (\cdot, y)\, \mathrm{d}s + o(\varepsilon),$$

où G est la fonction de Dirichlet :

$$\begin{cases} \nabla_x \cdot \Big(\sigma \nabla_x G(x,y) \Big) = -\delta_y, \text{in } \Omega, \\ G(x,y) = 0, \quad \forall x \in \partial\Omega. \end{cases}$$

La matrice $\mathcal{M}_\alpha$ est symétrique, définie positive. De plus, elle est diagonale si $\alpha \neq 1$.

$$\text{Si } 0<\alpha<1: \quad \mathcal{M}_\alpha = \int_{\mathbb{T}} f(\tau)\mathrm{d}\tau \begin{pmatrix} \sigma_0/\sigma_m & 0 \\ 0 & 1 \end{pmatrix},$$
$$\text{Si } \alpha>1: \quad \mathcal{M}_\alpha = \begin{pmatrix} -\int_0^{+\infty} q(s)(\sigma_0/\overline{\sigma}^\sharp(s))\mathrm{d}s & 0 \\ 0 & D_\infty \end{pmatrix},$$

où q est la fonction de répartition de f [85] :

$$q(x) = \int_{\mathbb{T}} \mathbb{1}_{0<x<f(\tau)}\, d\tau, \quad \sigma^\sharp(X,\tau) = \begin{cases} \sigma_0, & \text{in } \{(X,\tau), \quad \tau\in\mathbb{T},\ X>f(\tau)\}, \\ \sigma_m, & \text{in } \{(X,\tau), \quad \tau\in\mathbb{T},\ 0<x<f(\tau)\}, \\ \sigma_1, & \text{in } \{(X,\tau), \quad \tau\in\mathbb{T},\ X<0\}. \end{cases}$$

Si $\alpha=1$, le tenseur de polarization est une matrice pleine explicitement donnée en fonction du correcteur de couche limite (*c.f.* Section 1 du Chapitre I).

4.2. Modèle des courants de Foucault dans des domaines à coins. La dernière partie de ce résumé de mes travaux de recherche porte sur le modèle des courants de Foucault dans un domaine à coin. En présence d'un matériau fortement conducteur à bord régulier plongé dans un milieu diélectrique, on peut remplacer le domaine conducteur par une condition d'impédance sur le bord du milieu conducteur pour calculer le champ électromagnétique. Cette condition généralement appelée condition de Leontovitch, n'est plus valide lorsque le domaine conducteur présente une singularité géométrique telle qu'un coin par exemple. Pour étudier ce type de problème, en collaboration avec M. Dauge, L. Krähenbühl, V. Péron et R. Perrussel, nous avons considéré d'abord le problème des courants de Foucault : pour $\delta>0$, le potentiel magnetique

$$\mathcal{A}_\delta \text{ satisfait } \begin{cases} -\Delta\mathcal{A}_\delta^+ = \mu_0 J \text{ in } \Omega_+, & \\ -\Delta\mathcal{A}_\delta^- + \dfrac{2i}{\delta^2}\mathcal{A}_\delta^- = 0 \text{ in } \Omega_-, & [\mathcal{A}_\delta]_\Sigma = 0, \text{ on } \Sigma, \\ \mathcal{A}_\delta^+ = 0 \text{ on } \Gamma, & [\partial_n\mathcal{A}_\delta]_\Sigma = 0, \text{ on } \Sigma. \end{cases}$$

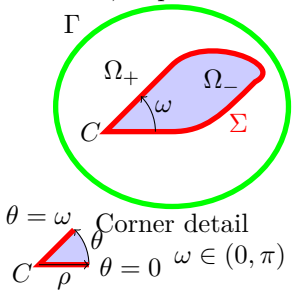

Le principe du développement asymptotique de $\mathcal{A}_\delta$, lorsque δ tend 0 est de localiser l'effet de la singularité à l'aide d'une fonction de troncature qui s'annule à distance inférieure à δ et vaut 1 au delà de 2δ. Ainsi, loin du coin, $\mathcal{A}_\delta$ est approché comme dans le cas de domaines réguliers, et près du coin on fait une remise à l'échelle qui permet de résoudre un problème profil avec un seul coin dans tout le plan. La difficulté est que, contrairement au cas lisse où l'on peut construire le développement asymptotique pas à pas, dans le cas de singularités il faut déterminer à l'avance l'ordre d'approximation désiré. Par exemple, pour les premiers termes de l'expansion, on procède comme suit. $\mathcal{A}_0$ est le potentiel lorsque "$\delta=0$" :

$$\begin{cases} -\Delta\mathcal{A}_0^+ = \mu_0 J \text{ in } \Omega_+, & \\ \mathcal{A}_0^+ = 0 \text{ on } \Sigma, & \mathcal{A}_0^- = 0, \text{ in } \Omega_-. \\ \mathcal{A}_0^+ = 0 \text{ on } \Gamma, & \end{cases}$$

A l'aide d'une fonction de troncature radiale φ au voisinage du coin, on approche $\mathcal{A}_\delta$ loin du coin

$$\mathcal{A}_\delta = \varphi(\cdot/\delta)\mathcal{A}_0 + r_\delta^0.$$

r_δ^0 est alors solution d'un problème qui se localise près du coin. En utilisant le développement de Kondratiev de $\mathcal{A}_0$ en fonctions singulières au voisinage du coin :

$$\mathcal{A}_0^+ \sim_{\rho\to 0} a_1\rho^\alpha \sin(\alpha(\theta-\omega)), \quad \text{with} \quad \alpha=\pi/(2\pi-\omega),$$

on fait apparaître le problème profil V_α dans le plan $\mathbb{R}^2$:

$$
\begin{aligned}
&-\Delta_X V_\alpha = [\Delta_X;\varphi]\,(R^\alpha \sin(\alpha(\theta-\omega))), \text{ in } S_+,\\
&-\Delta_X V_\alpha + 2\mathrm{i}V_\alpha = 0, \text{ in } S_-,\\
&[V_\alpha]_{\mathcal{G}} = 0, \quad \left[\frac{1}{R}\partial_\theta V_\alpha\right]_{\mathcal{G}} = \alpha\varphi R^{\alpha-1},\\
&V_\alpha \to_{|X|\to+\infty} 0,
\end{aligned}
$$

et on obtient l'approximation de $\mathcal{A}_\delta$:

$$\mathcal{A}_\delta = \varphi\left(\frac{\cdot}{\delta}\right)\mathcal{A}_0 + (1-\varphi)a_1\delta^\alpha V_\alpha\left(\frac{\cdot}{\delta}\right) + r_\alpha^\delta.$$

En figure 9, on voit que l'impédance "classique" qui est une constante donne une mauvaise approximation

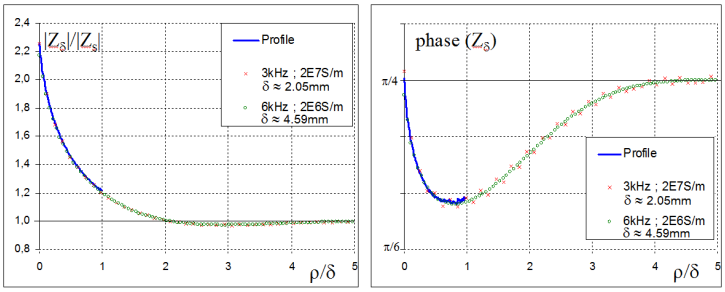

FIGURE 9. Impédance calculée sur un maillage fin comparée au rapport $\sqrt{2}iV_\alpha/\partial_n V_\alpha$

près du coin, alors que l'impédance "profile", tracée en bleu, donne le bon comportement.

La justification du développement à tout ordre est actuellement en cours.

5. Projet de recherche

J'envisage de poursuivre, au moins à court et moyen terme, l'orientation vers la modélisation mathématique de problèmes issues de la biologie et la médecine.

5.1. Electroporation : vers des modèles tissulaires. J'envisage de développer un modèle d'électroporation tissulaire pour modéliser le transport de plasmide dans un muscle après l'application du choc électrique. Une collaboration avec R. Natalini et E. Signori de l'Université de Tor Vergata a débuté à ce sujet. A plus long terme, un enjeu important du point de vue clinique est de proposer un outil numérique basé sur l'imagerie médicale qui permet de donner la zone électroporée sur l'image en fonction du placement des électrodes et des paramètres du pulse d'une part, et de présenter une optimisation possible pour l'application du pulse, d'autre part.

5.2. Modélisation de l'invadopodia. Avec le laboratoire de T. Suzuki, je m'intéresse depuis un peu plus d'un an à la modélisation de l'invadopodia, un processus de migration des cellules cancéreuses. Le challenge de la modélisation est de bien prendre en compte la déformation de la cellule due à la polymérisation de l'actine à l'intérieur de la cellule, ce qui entraîne une pression sur la membrane ainsi que la formation de podosome à la surface de la cellule (cf figure 10).

Un premier modèle à frontière libre décrivant la polymérisation de l'actine et la migration cellulaire qui en découle a été développé, il est donné en conclusion du chapitre III. Son analyse mathématique et numérique est actuellement en cours, en collaboration avec T. Suzuki (Osaka University) et M. Ohta (Tokyo University of Science). Ce modèle, succintement présenté en conclusion du chapitre II, est un premier pas dans la compréhension du phénomène, et je projette de poursuivre l'activité de modélisation en collaboration avec Osaka University. La thèse d'O. Gallinato, que j'encadre en co-tutelle avec T. Colin et T. Suzuki vient de débuter en septembre 2013 sur cette thématique.

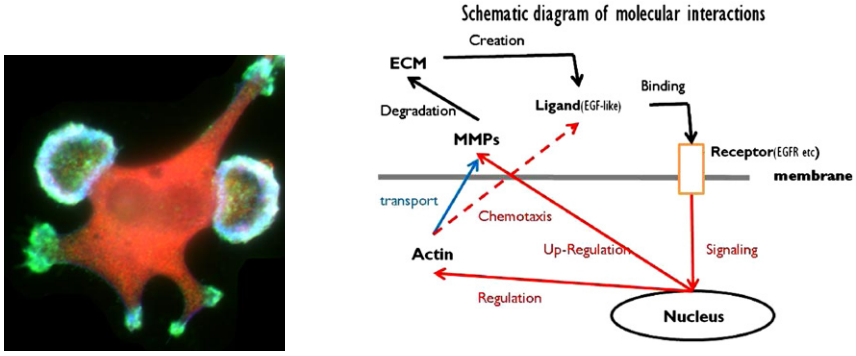

(a) Formation de protusions (b) Cascade des réactions chimiques dans la cellule

FIGURE 10. Principes généraux du processus d'invadopodia

5.3. Modélisation de la croissance tumorale. Je compte poursuivre les travaux autour de la modélisation de la croissance tumorale en m'intéressant à la modélisation des sphéroïdes qui est un bon modèle biologique *in vitro* de tumeur, dans le cadre de la thèse de T. Michel. Ce travail, en collaboration avec l'ITAV de Toulouse permettrait d'apporter une meilleure compréhension de la croissance tumorale et notamment de la répartition des cellules proliférantes et quiescentes dans la tumeur en fonction des gradients de concentrations de nutriments et de facteurs de croissance. En outre, un projet de couplage entre croissance de sphéroïdes et électroporation est envisagé avec l'IPBS de Toulouse : cela permettrait de faire le lien entre la partie modèle d'électroporation d'une part et la partie croissance tumorale pour évaluer la réponse thérapeutique de certains cancers à un traitement par électrochimiothérapie.

Par ailleurs, dans le cadre du postdoctorat de J. Joie, avec T. Colin et O. Saut, nous nous intéressons à la modélisation de la croissance des méningiomes, en collaboration avec G. Kantor de l'Institut Bergonié et H. Loiseau de l'Hôpital Pellegrin. Cette modélisation s'inscrit dans la philosophie des modèles de croissance de tumeurs métastatiques développés au sein de l'équipe MC2 : la croissance de la tumeur est décrite à l'aide d'équations d'advection, la vitesse dérivant d'un gradient de pression obtenue par une loi de Darcy.

Les méningiomes sont des tumeurs non-infiltrantes de la duremère, la membrane rigide qui entoure le cerveau. Le méningiome est généralement une tumeur à croissance lente qui exerce une pression sur le tissu noble avoisinant, sans l'envahir. Le traitement généralement appliqué est la radiothérapie, qui semble avoir un double effet : tuer les cellules proliférantes et remettre les cellules quiescentes dans un cycle normal. Le challenge de la modélisation est d'apporter des outils numériques qui permettent de prédire la réponse au traitement spécifique à chaque patient à l'aide de l'imagerie médicale. Pendant le postdoctorat de J. Joie, nous avons développé un modèle de croissance qui reproduit bien les données d'imagerie médicale qui sont à notre disposition (cf figure 11). La modélisation de l'effet de la radiothérapie est actuellement en cours.

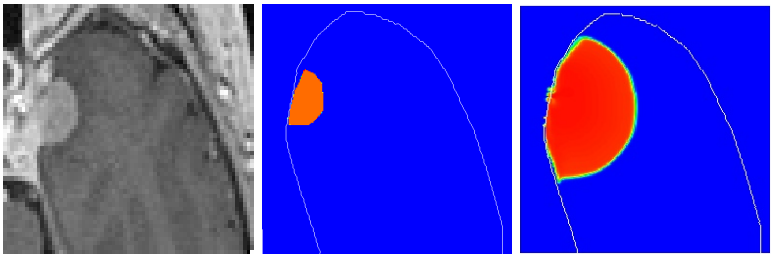

FIGURE 11. CT scan et simulation de la croissance du meningiome

6. Liste complète des publications depuis la thèse

Publications autour de l'électroporation.

- **Poignard, C.** (2009), *About the transmembrane voltage potential of a biological cell in time-harmonic regime*, ESAIM: Proceedings, 26:16-179.
- Cindea, N.; Fabrèges, B.; De Gournay, F. & **Poignard, C.** (2010), *Optimal placement of electrodes in an electroporation process*, ESAIM: Proceedings, 30:34-43.
- Duruflé, M.; Péron, V. & **Poignard, C.** (2011), *Time-harmonic Maxwell equations in biological cells. The differential form formalism to treat the thin layer*, Confluentes Mathematici, 3(2): 325-357.
- **Poignard, C.**; Silve, A.; Campion, F.; Mir, L., M.; Saut, O. & Schwartz, L. (2011), *Ion flux, transmembrane potential, and osmotic stabilization: A new electrophysiological dynamic model for Eukaryotic cells*, European Biophysics Journal, 40(3): 235-246.
- Kavian, O.; Leguèbe, M.; **Poignard, C.** & Weynans, L. (2012), *"Classical" electropermeabilization modeling at the cell scale*, Journal of Mathematical Biology.
- Perrussel, R. & **Poignard, C.** (2013), *Asymptotic Expansion of Steady-State Potential in a High Contrast Medium with a Thin Resistive Layer*, Applied Mathematics and Computation, 221:48-65.
- **Poignard, C.** & Silve, A. (2014), *Différence de potentiel transmembranaire des cellules biologiques*, Revue 3EI, n^{o}75.
  - Leguèbe, M., **Poignard, C.** & Weynans, L., (2013), *"A second Order Cartesian Method for the simulation of electropermeabilization cell models*, Inria Research Report RR-8302, Submitted.
- Duruflé, M., Péron, V. & **Poignard, C.** (2014), *Thin layers in electromagnetism*, Published on-line in CiCP. http://www.dx.doi.org/10.4208/cicp.120813.100114a.
- Leguèbe, M., Silve, A., Mir, L.M, & **Poignard, C.**, (2014) *Conducting and Permeable States Membrane Submitted to High Voltage Pulses. Mathematical and Numerical Studies Validated by the Experiments*, Published on-line in Jnl. Th. Biol. http://www.dx.doi.org/10.1016/j.jtbi.2014.06.027.

Publications autour de la migration cellulaire.

- Colin, T.; Durrieu, M.-C.; Joie, J.; Lei, Y.; Mammeri, Y.; **Poignard, C.** & Saut, O. (2013), *Modelling of the migration of endothelial cells on bioactive micropatterned polymers*, Math. BioSci. Eng., 10(4):997-1015.
  - Joie, J.; Y. Lei; Colin, T.; Durrieu, M.-C.; **Poignard, C.** & Saut, O. (2013), *Modeling of migration and orientation of endothelial cells on micropatterned polymers*, Inria-RR 8252, Submitted.

Publications autour de la croissance tumorale.

  - Colin, T., Gallinato, O., **Poignard, C.**, Saut, O. (2014), *Tumor growth model for ductal carcinoma: from* **in situ** *phase to stroma invasion.* Inria Research Report RR–8502, Submitted.

Publications autour des couches rugueuses.

- **Poignard, C.** (2009), *Approximate transmission conditions through a weakly oscillating thin layer*, Math.Meth.Appl.Sci., 32(4):435-453.
- Ciuperca, I. S.; Perrussel, R.; **Poignard, C.** & Saut, O. (2010), *Influence of a Rough Thin Layer on the Potential*, IEEE Trans. on Mag., 46(8):2823-2826.
- Ciuperca, I. S.; Perrussel, R.; **Poignard, C.** & Saut, O. (2010), *Approximate Transmission Conditions through a rough thin layer. The case of the periodic roughness*, EJAM, 21(1):51-75.
- Ciuperca, I. S.; Perrussel, R.; **Poignard, C.** & Saut, O. (2011), *Two-scale analysis for very rough thin layers. An explicit characterization of the polarization tensor*, JMPA, 95(3):227-295.
- **Poignard, C.** (2011), *Explicit characterization of the polarization tensor for rough thin layers*, EJAM, 22:1-6.
- **Poignard, C.** (2013), *Boundary Layer Correctors and Generalized Polarization Tensor for Periodic Rough Thin Layers. A Review for the Conductivity Problem*, ESAIM:Proceedings, 37:136-165.

Publications autour des singularités de coins.

- Krähenbühl, L.; Buret, F.; Perrussel, R.; Voyer, D.; Dular, P.; Péron, V.; **Poignard, C.** (2011) *Numerical treatment of rounded and sharp corners in the modeling of 2D electrostatic fields*, J.Microwaves and OptoElectroMag. , 10(1):66-81.
- Buret, F, Dauge, M.; Dular, P.; Krähenbühl, L.; Péron, V.; Perrussel, R.; **Poignard, C.**; Voyer, D. (2012) *Eddy currents and corner singularities*, IEEE Trans. on Mag., 48(2):679-682.
- Dauge, M.; Dular, P.; Krähenbühl, L.; Péron, V.; Perrussel, R.; **Poignard, C.** (2013) *Corner asymptotics of the magnetic potential in the eddy-current model*, Math.Meth.Appl.Sci., published on-line.

CHAPTER I

Modeling electroporation in a single cell

Eukaryotic cell is a complex biological entity, which is the main constituent of any biological tissues: it is somehow the base unit of any living organism. These cells are generically composed of cytoplasm, which includes nucleus, mitochondria and other organelles that are necessary to life. This cytoplasm is protected from the extracellular stress by the plasma membrane, which is a phospholipid bilayer. This barrier plays a double role of protecting and filtering the exchanges between the cytoplasm and the extracellular medium. In the 70's, it has been observed that electric shock may change transiently the membrane porosity, allowing the entrance of usually non-permeant molecules into the cytoplasm. This phenomenon, called electroporation or electropermeabilization has then been studied for cancer treatments, by coupling a cytotoxic drug – such as bleomycin or cisplatin – with high voltage pulses [71]. Electrochemotherapy is now used in more than 40 Cancer Institutes in Europe for cutaneaous tumors and several clinical studies are driven for deep located tumors. Even though the bases of cell electroporation are well-known, several experimental observations are still unexplained and the modeling of the phenomenon suffers from a lack of accuracy. The aim of this chapter consists in providing new models of cell electroporation that corroborate the experimental results, with the long-term goal to make the pulse delivery optimization possible, in order to widen the use of electrochemotherapy among cancer treatments.

The chapter is organized into 6 sections. We first present the linear electric model of Schwan *et al.* [42] in which the cell is composed of a conducting cytoplasm surrounded by a resistive thin layer. We present briefly asymptotic results that made it possible to approach the electric potential in such a high contrast medium with thin layer by imposing equivalent transmission conditions across the interface between the cytoplasm and the outer medium. We then focus on the electroporation phenomenon. In Section 2, we describe the models that have been derived at the end of the 90's and we present the KDN-model, which is considered as the most achieved description of electroporation. Then, we discuss their main drawbacks, that justify the derivation of new models. In Section 3, we present our conducting model of cell membrane, and we provide preliminary results of its fitting with patch–clamp experiments. We show how this new electrical model avoids the drawbacks of the other models and we then present in Section 4.2 our model of permeable state of the membrane. This way to model electroporation as the coupling of conducting and permeable states of the membrane is new and it yields the main insight of this chapter. Section 5 is devoted to numerical results in 3D that corroborate the experimental data, and we conclude by forthcoming research on electroporation.

It is worth noting that part of the results of Section 3 to Section 5 reflects the work of M. Leguèbe, a PhD candidate I am supervising with T. Colin, whose PhD defense is scheduled for september 2014.

1. Cell electrical modeling in the linear regime

In the Schwan model [39, 42], the cell is composed by a homogeneous conducting cytoplasm, whose diameter is about tens of micrometers, surrounded by a very insulating membrane a few nanometers thick (see Figure 1). The simplest way to model the cell is to derived an electric circuit model in which the cell cytoplasm is described as by a resistivity $\mathrm{R_c}$, the cell membrane is identified to a capacitor whose capacitance equals $\mathrm{C_m}$ and the ambient medium is described by a resistivity $\mathrm{R_e}$ as given by Figure 2. Kirchhoff 's circuit law writes then

$$V_{cell} = V_{\mathrm{m}} + \mathrm{R_c C_m} \frac{dV_{\mathrm{m}}}{dt}.$$

If a static electric field of magnitude E is applied to the cell of diameter R we get

$$2RE = V_{\mathrm{m}} + \mathrm{R_c C_m} \frac{dV_{\mathrm{m}}}{dt},$$

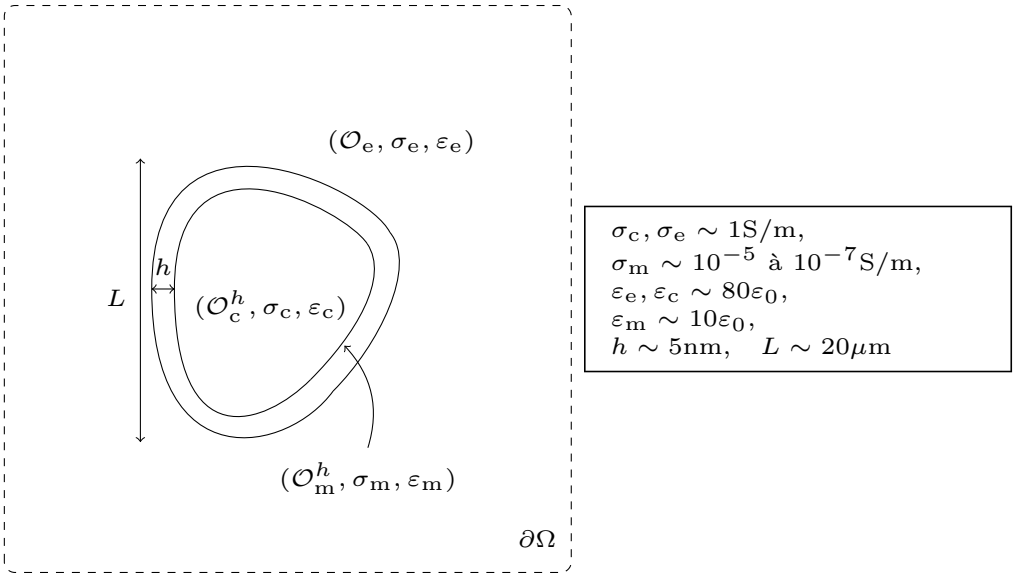

FIGURE 1. Electrical model of biological cell by Schwan, Fear, Stuchly, *et al.* [39, 42]. The cytoplasm $\mathcal{O}_\mathrm{c}$ is protected thanks to the thin membrane $\mathcal{O}_\mathrm{m}$, whose thickness h is about a few nanometers. The cell is embedded in an extracellular medium denoted by $\mathcal{O}_\mathrm{e}$. We denote by Ω the whole domain.

or in terms of conductivity:

$$2\sigma_\mathrm{c} RE = \sigma_\mathrm{c} V_\mathrm{m} + \mathrm{C_m}\frac{dV_\mathrm{m}}{dt}. \tag{12}$$

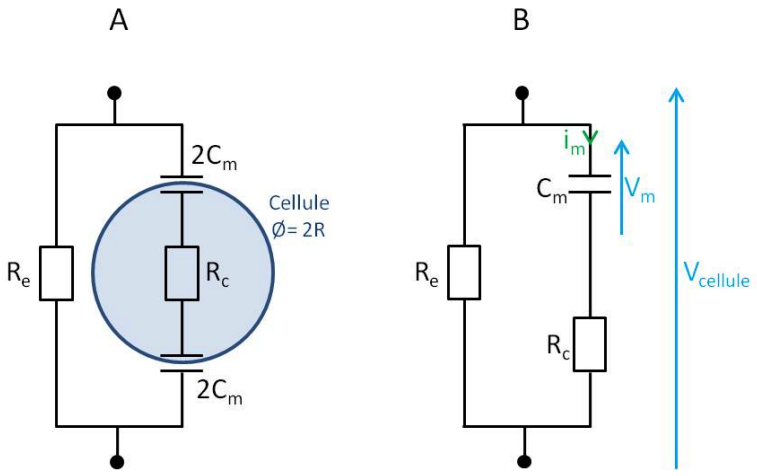

FIGURE 2. Electric circuit equivalent to the Schwan model [42].

However this equivalent model is too rough, and in particular it cannot describe the influence of the cell shape or the effect of the direction of the electric field on the membrane voltage. Therefore, it is necessary to use partial differential equations (PDE), which describe the electric field in the whole cell.

In the electroquasistatic approximation, the time variations of the magnetic induction are neglected and the electric field is derived from the electric potential $E = -\nabla V$. Taking the divergence of the Maxwell-Ampère law, as descibed in [86], we obtained the following time-dependent equation on the electric potential:

$$\begin{aligned}&\partial_t \nabla \cdot (\varepsilon \nabla V) + \nabla \cdot (\sigma \nabla V) = 0, \quad \text{in } \Omega,\\ &V|_{\partial\Omega} = g, \quad V|_{t=0} = V_0,\end{aligned}$$

where g and V_0 are given. For the inner and the outer domains, the ratio ε/σ is about $10^{-9}s$, meaning that up to several mega-hertz, the displacement currents can be neglected in these media. However, due to the high resistivity of the membrane, these currents have to be accounted for in the thin layer [82]. The electric potential is the continuous solution to

$$\begin{aligned}&\nabla \cdot (\sigma \nabla V) = 0, \quad \text{in } \mathcal{O}_{\mathrm{c}}^h \cup \mathcal{O}_{\mathrm{m}}^h \cup \mathcal{O}_{\mathrm{e}},\\ &(\sigma \partial_{\boldsymbol{n}} V)\,|_{\Gamma^+,\Gamma_h^-} = \varepsilon_{\mathrm{m}} \partial_t \partial_{\boldsymbol{n}} V|_{\Gamma^-,\Gamma_h^+} + \sigma_{\mathrm{m}} \partial_{\boldsymbol{n}} V|_{\Gamma^-,\Gamma_h^+}, \quad \text{on } \Gamma \text{ and } \Gamma_h \text{ respectively},\\ &V|_{\partial\Omega} = g, \quad V|_{t=0} = V_0,\end{aligned}$$

where Γ_h and Γ are the respective outer and inner boundaries of the cell membrane, and the normal vectors are taken from the inner to the outer part of the cell. Even though this equation is a rough simplification of the Maxwell vector equations, ∇V describes quite precisely the electric field at low frequency and thus it is widely used in the electrical bioengineering community. However, due to the high resistivity and the small thickness of the membrane, it is still complex to solve accurately the above equation on V.

To perform computations on realistic cell shapes without meshing the cell membrane, Pucihar *et al.* [89] propose to replace the membrane by an equivalent condition on the boundary of the cytoplasm, see Figure 3. Denoting by S_{m}^0 the surface conductivity and by $\mathrm{C_m}$ the capacitance of the membrane defined as

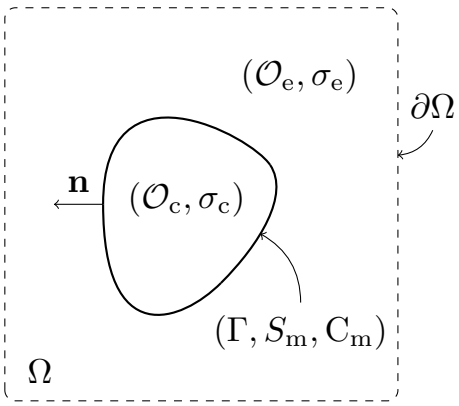

FIGURE 3. Cell model with a zero-thickness membrane. The influence of the membrane is described through its capacitance $\mathrm{C_m}$ and its surface conductivity S_{m}.

$$\mathrm{C_m} = \varepsilon_{\mathrm{m}}/h, \quad S_{\mathrm{m}}^0 = \sigma_{\mathrm{m}}/h,$$

and denoting by $\mathcal{O}_{\mathrm{c}}$ the whole cell

$$\mathcal{O}_{\mathrm{c}} = \overline{\mathcal{O}_{\mathrm{c}}^h} \cup \mathcal{O}_{\mathrm{m}},$$

the electric potential V is approached by U, the solution to

$$\Delta U = 0, \quad \text{in } \mathcal{O}_{\mathrm{c}} \cup \mathcal{O}_{\mathrm{e}}, \tag{13a}$$

$$\sigma_{\mathrm{e}} \partial_{\boldsymbol{n}} U|_{\Gamma^+} = \sigma_{\mathrm{c}} \partial_{\boldsymbol{n}} U|_{\Gamma^-}, \tag{13b}$$

$$\mathrm{C_m} \partial_t V_{\mathrm{m}} + S_{\mathrm{m}}^0 V_{\mathrm{m}} = \sigma_{\mathrm{c}} \partial_{\boldsymbol{n}} U|_{\Gamma^-}, \quad \text{where } V_{\mathrm{m}} = U|_{\Gamma^+} - U|_{\Gamma^-}, \tag{13c}$$

$$U|_{\partial\Omega} = g, \quad U|_{t=0} = V_0. \tag{13d}$$

It is worth noting that unlike V, the approximate potential U is discontinuous across the interface: this is the effect of the high resistivity and the small thickness of the membrane. Condition (13c) corresponds to a

contact resistance model, and equation (13) is a generalization of (12). In time-harmonic regime, we have proven in [82, 81] that far from the membrane, the following estimates holds, which ensures that the electric field is accurately approached by ∇U.

THEOREM 1.1 (Theorem 1.3 [81]). *Let $g : (t, x) \to e^{2i\pi ft} G_H(x)$, and write the electric potentials V and U as*

$$V(t, x) := e^{2i\pi ft} V_H(x), \quad U(t, x) := e^{2i\pi ft} U_H(x).$$

If G_H belongs to $H^{5/2}(\partial\Omega)$, then for any domain ω compactly embedded in $\mathcal{O}_e$ or in $\mathcal{O}_c$, for h small enough

$$\|\nabla(V_H - U_H)\|_\omega \leq Ch \, |G_H|_{H^{5/2}(\partial\Omega)},$$

where C is a constant independent of h.

In Theorem 1.3 of [81], we provide the rigorous expansion at any order and we present numerical results that illustrate the theoretical results, but we focus on this first order approximation in this thesis, since it is the most relevant from the modeling point of view.

In the following sections, we use (13) to model the electroporation phenomenon. Roughly speaking, we add a non-linear law on the membrane conductivity in the Kirchhoff law. The description of the non-linear behaviour of the cell membrane is the main topic of this chapter, therefore we do not extensively present the asymptotic analysis in smooth domains that made possible the derivation of the above theorem. The reader may refer to [81, 82] for more details.

It is worth noting that the electroquasistatic formulation is an approximation of the full Maxwell equations, however the influence of the magnetic field on biological tissues and more precisely on cells is still unclear. In particular, it seems that the electroquasistatic potential describes the electrical behaviour of the cell with a good accuracy, and therefore it is relevant to model electroporation from this formulation. Let us mention however that in the linear regime, we have studied in [36, 37] the effect of the cell membrane on the electromagnetic field solution to time-harmonic Maxwell equations. Here again the high resistivity and the small thickness of the membrane make appear a discontinuity in the tangent trace of electric field, which is proportional to the surface gradient of the normal trace, as stated in equation 3.5 of [37] . For the sake of conciseness, we do not present the results and we refer the reader to [36, 37] .

2. Basic concepts in biophysics for pore formation in liposomes

The creation and growth of single pore in vesicles have been studied for many years by biophysicists [119, 96, 60, 94]. At the end of the 90's, Sandre *et al.* [96] have studied the pore creation in vesicles embedded in a high viscous fluid. The high viscosity of the ambient medium made possible the real–time visualization of the "pore life" of stretched vesicles, and thus the comparison of the theory with the experiments. In this section, we present the different models that have been developed to describe the pore radius evolution. We also describe briefly how the pore density evolution, which is probably the most currently used model, has been derived, and we conclude by important drawbacks of this modeling that justify the derivation of new models.

2.1. Single pore models. Generally speaking, pore radius models are based on the description of the free–energy of membranes, thanks to which Langevin–type equation provides the pore radius evolution. Once the membrane free–energy E is known, the time–evolution of the single pore radius r behaves as follows [119]:

$$\frac{dr}{dt} = -\frac{D}{k_B T} \partial_r E, \tag{14}$$

where D, k_B and T hold respectively for the diffusion coefficient, the Boltzmann constant and the temperature. However the derivation of the membrane free–energy is still quite controversial, and we present in the two next subsections the two main models that describe the single pore radius, that we call respectively BGS–CW model and DAV–model.

From these models, Smoluchowski equation, which is a drift–diffusion equation on the distribution function of pores of radius r, is derived in Subsection 2.2. This partial differential equation has been approached by an ordinary differential equation on the total pore density, thanks to a subtle asymptotic analysis done by Neu and Krassowska [72]. It is worth noting that according to Kroeger *et al.* [60], both BGS–CW model and DAV–model of pore radius lead to the same ordinary differential equation.

2.1.a. *The classical BGS–CW model.* Brochart–Wyart, de Gennes and Sandre [96] on one side and Chizmadzhev and Weaver [119] on the other side proposed a quite similar membrane energy E_f given by:

$$E_f(r) = 2\pi\gamma r - \pi r^2\sigma_0 + \frac{C_s}{r^4},$$

where γ is the line tension, which tends to shrink the pore, while σ_0 is the surface tension of the stretched vesicles. The term C_s/r^4 holds for the steric repulsion of the lipids. It ensures that a small space r_0 between the phospholipids remains at rest, and has a very low influence for pore radii above r_0.

In order to model the electroporation phenomenon, Chizmadzhev and Weaver added the electrostatic energy E_p, which describes the fact that the membrane behaves as a capacitor:

$$E_p(r) = a_p\pi r^2 V_{\rm m}^2,$$

where a_p is the membrane capacitance and $V_{\rm m}$ is the transmembrane voltage. The total membrane energy reads then

$$E(r) = E_f(r) + E_p(r) = 2\pi\gamma r - \pi r^2\left(\sigma_0 + a_p V_{\rm m}^2\right) + \frac{C_s}{r^4}.$$

The pore radius evolution, which is called here *BGS–CW model*, is then derived thanks to (14) into

$$\frac{dr}{dt} = -\frac{D}{k_B T}\left(2\pi\gamma - 2\pi r\left(\sigma_0 + a_p V_{\rm m}^2\right) - \frac{4C_s}{r^5}\right).$$

Stokes–Einstein relation links the diffusion coefficient to the membrane viscosity $\eta_{\rm m}$ as

$$\frac{D}{k_B T} = \frac{1}{2\pi\eta_{\rm m}\delta},$$

where δ is the membrane thickness, such that

$$\frac{dr}{dt} = -\frac{1}{\eta_{\rm m}\delta}\left(\gamma - r\left(\sigma_0 + a_p V_{\rm m}^2\right) - \frac{C_s}{r^5}\right), \tag{15}$$

where C_s has been adequately modified. This model, which is the basis used by Neu and Krassowska [72] to derive the pore density evolution has two main drawbacks. The first one lies in the fact that the pore expansion is exponentially fast if the critical radius r_c given by

$$r_c \sim \frac{\gamma}{\sigma_0 + a_p V_{\rm m}^2},$$

is overcome, which is hardly defensible since the pore radius should be bounded at least by half of the membrane circumference. On the other hand, if the membrane voltage is stoppped, the pore shrinks, but the shrinkage is linear as soon as the radius is smaller than γ/σ_0, whereas Sandre *et al.* have reported an acceleration of the shrinkage for small radii.

Very recently, Kroeger, Ryham, *et al.* [60, 94] have pointed out that experiments are at odds with the linear closure, and they derived in two different ways a curvature–driven pore model, without accounting for the electroporation force.

2.1.b. *Curvature–driven pore closure: the role of aequous viscosity.* In [94], Ryham *et al.* suggested that the aequous viscosity of the ambient medium impacts the pore dynamics. They derived the Dominant Aequous Viscosity (DAV) model by adding a force F_s, which accounts for the lateral stresses generated on the bilayer:

$$F_s = C\eta_s r\frac{dr}{dr},$$

where C is a non–dimension constant, whose value is around $C \sim 8$ according to [94], and η_s is the viscoity of the solution. Summing up all the forces, the following O.D.E on the pore radius evolution in membrane submitted to a transmembrane voltage holds:

$$C\eta_s r\frac{dr}{dt} + \eta_{\rm m}\delta\frac{dr}{dt} = -\gamma + r\left(\sigma_0 + a_p V_{\rm m}^2\right) + \frac{C_s}{r^5}.$$

Note that the steric repulsion C_s/r^5 is not given in the DAV model as written in [94], however it is necessary to prevent non–positive radii. The main insight of this model, which fits very well the experiments of Portet and Dimova [87], as shown by Figure 5 of [94], is the predominance of the aequous viscosity. Actually even

if η_s is much smaller than the lipid viscosity, for pore radii bigger than 1μm, the term $C\eta_s r$ plays a crucial role in the pore closure since the membrane thickness h is very small of order 10nm. The term

$$\eta_{\text{eff}}(r) = \eta_{\text{m}} h + Cr\eta_s,$$

can be seen as the effective membrane viscosity, which increases linearly with respect to the pore radius. Ryham *et al.* pointed out that due to the membrane thinness, the aequous viscosity cannot be neglected, explaining the curvature–driven pore closure. Kroeger *et al.* used another reasoning based on the electrochemical potential to obtain a similar equation (see equation (7) of [60]).

2.2. From one pore to the total pore density. From these descriptions of single pore evolution, Neu and Krassowska [72], and Kroeger *et al.* [60] used the Smoluchowski equation to describe the number of pores of radius r at time t by the function n satisfying:

$$\partial_t n = D\frac{\partial}{\partial r}\left(\frac{1}{k_B T} n \partial_r E + \partial_r n\right) + S(t,r). \tag{16}$$

The coefficient D is a diffusion coefficient of the pore distribution, and the source term describes the fluctuation in the number of pores due to pore creation and pore destruction [60]. The choice of the source term, which is crucial in the asymptotic analysis of Neu and Krassowska [72] is quite unclear, and contains some parameters, whose value are arbitrarily fixed:

$$S(r,t) = \frac{\nu_c \delta}{k_B T}\partial_r U e^{-U/(k_B T)} - \nu_d n H(r - r_\star),$$

where $r_\star$ is the "critical radius" of the pore[1], ν_c and ν_d denote the fluctuation rates per unit volume and molecule respectively, U is the energy function of non–conducting pores:

$$U(r) = \frac{r^2}{r_\star^2} F_\star - \pi r^2 a_p V_{\text{m}}^2,$$

where $F_\star$ is the energy associated to the critical radius $r_\star$. We emphasize that the boundary conditions at $r = 0$ and $r = +\infty$ are not precisely given but homogeneous Dirichlet boundary conditions seem to be imposed. Thanks to a tricky rescaling, and a subtle asymptotic analysis, Neu and Krassowska derived the following ordinary differential equation on the total number of pores N_{ep} [72, 32]:

$$\frac{dN_{\text{ep}}}{dt} = \alpha e^{V_{\text{m}}^2/\text{V}_{\text{ep}}^2}\left(1 - \frac{N_{\text{ep}}}{N_o} e^{-qV_{\text{m}}^2/\text{V}_{\text{ep}}^2}\right), \tag{17}$$

where V_{ep} is the threshold membrane voltage above which electroporation occurs, N_o is the pore density at rest, when V_{m} equals 0, and α and $q > 1$ are *ad hoc* parameters. It is worth noting that the values of these non–measurable parameters are unclearly chosen.

2.2.a. *The KDN–model for electroporation current.* From the total pore density, Debruin and Krassowska [32] deduced the nonlinear electroporation current I_{ep}:

$$I_{\text{ep}}(t, V_{\text{m}}) = N_{\text{ep}}(t, V_{\text{m}}) i_{\text{ep}}(V_{\text{m}} RT/F),$$

where i_{ep} is the current through a single pore. This single pore current is described by a sigmoidal function with 4 non–measurable parameters, given by formula (7) [32] as

$$i_{\text{ep}}(\nu_{\text{m}}) = \frac{\sigma\pi r_{\text{m}}^2 F}{RT\delta} \frac{\nu_{\text{m}}\left(e^{\nu_{\text{m}}} - 1\right)}{e^{\nu_{\text{m}}}\dfrac{w_o e^{w_0 - n\nu_{\text{m}}} - n\nu_{\text{m}}}{w_o - n\nu_{\text{m}}} - \dfrac{w_o e^{w_0 + n\nu_{\text{m}}} + n\nu_{\text{m}}}{w_o + n\nu_{\text{m}}}}. \tag{18}$$

Here again, the definition of the 4 parameters is quite unclear: Krassowska and Debruin define them as the mean pore radius r_{m}, the pore conductivity σ, the membrane barrier energy "inside a pore" w_o and the "relative entrance length of the pore" n. The Kirchhoff equation (13c) is then changed into

$$\text{C}_{\text{m}}\partial_t V_{\text{m}} + \text{S}_{\text{m}}^0 V_{\text{m}} + I_{\text{ep}}(t, V_{\text{m}}) = \sigma_{\text{c}} \partial_{\boldsymbol{n}} U|_{\Gamma^-}. \tag{19}$$

[1] $r_\star$ denotes the mean distance between two phospholipids when the membrane is at rest.

This model with at least 8 parameters, which is called KDN–model in this manuscript, has been extensively used in the past decade. It provides qualitative results that are more or less in accordance with the experiments. However, even though the physical basis of the model is clearly stated, the choice of the parameters is quite obscure. In addition, and due to the number of parameters, the fit of the model to obtain quantitative results in accordance with the experiments are hardly obtainable.

2.2.b. *Drawbacks of the KDN–model.* We point out some drawbacks of the KDN–model, that justify the derivation of new models:

- The dynamics of $N_{\rm ep}$ is not intrinsic to the membrane. Actually, the increase of $N_{\rm ep}$ is driven by $\alpha e^{V_{\rm m}^2/{\rm V}_{\rm ep}^2}$ while the global pore shrinkage is driven by $\alpha e^{(1-q)V_{\rm m}^2/{\rm V}_{\rm ep}^2}/N_o$.
- The pore density $N_{\rm ep}$ is not bounded: it is possible to create more pores than the membrane area.
- The current through one single pore $i_{\rm ep}$ is very sensitive to the parameters w_o, n, σ and $r_{\rm m}$, which makes the identification of the parameters with the experiments hardly obtainable.
- The modeling is based on the existence of pores, while such pores have never been observed in experiments.
- The model identifies the high conducting state of the membrane and the electropermeabilization, while it has been reported by Benz *et al.* [9] that the conducting state lasts a few microseconds after the pulse for planar bilayer, while the permeable state of the membrane lasts several minutes according to Mir *et al* [71].

For all these reasons, we choose to develop new models of electropermeabilization, which avoid these drawbacks. Instead of dealing with complex biophysics models involving a lot of parameters, we prefer to deal with phenomenological models, that describe all the main features observed in the experiments with the fewest parameters. The fact that a few parameters are involved in our models will facilitate the parameter identification to obtain results that are quantitatively in accordance with the experiments. We emphasize that the main topic of this thesis does not deal with the inverse problem that consists in the fitting of the model parameters. The aim of this chapter is to provide relevant models for cell electroporation, however it is important to keep in mind that the fitting is crucial for the applications, in order our models to involve the least possible parameters.

3. Phenomenological approach for membrane conductivity

Since cell electroporation is initiated by eletric pulse delivery, and since it has been shown by Benz *et al.* that the membrane conductivity increases dramatically during the pulse, we first develop a nonlinear electrical cell model. This model, presented in [56], has been derived similarly to the sliding–door model of voltage–gated ion channels in electrophysiology.

3.1. The sliding–door model for membrane conductivity. Our sliding–door model describes the position X of a fictitious gate between 0 and 1, which describes the degree of poration of the membrane. The position of X depends on two variables: the time t and a scalar variable which corresponds to the membrane voltage, and which is denoted by λ. The membrane surface conductivity $S_{\rm m}$ is then given by

$$S_{\rm m}(t,\lambda) = {\rm S}_0 + {\rm S}_1 X(t,\lambda), \tag{20a}$$

where $\rm S_0$ is the membrane conductivity at rest, and S_1 is the surface conductivity of the fully porated membrane. The non–dimension variable X is governed by the following ordinary differential equation:

$$\frac{\partial X(t,\lambda)}{\partial t} = \max\left(\frac{\beta(\lambda)-X(t,\lambda)}{\tau_{\rm ep}}; \frac{\beta(\lambda)-X(t,\lambda)}{\tau_{\rm res}}\right), \quad t>0, \tag{20b}$$

$$X(0,\lambda) = X_0, \tag{20c}$$

where $\tau_{\rm ep}$ and $\tau_{\rm res}$ are the characteristic times of "pore" creation and "pore" closure respectively, and β is a sigmoidal function, which is a regularization of the Heaviside function. One can choose the two parameters function:

$$\beta(\lambda) = \frac{1+\tanh\left(k\left(|\lambda|-{\rm V}_{\rm ep}\right)\right)}{2}, \tag{21}$$

or if one wants to introduce the electrostatic energy:

$$\beta(\lambda) = e^{-(\mathrm{V_{ep}}/\lambda)^{2k}}. \tag{22}$$

Generically speaking, it is enough that β be a function satisfying

$$\begin{cases} \beta \in W^{1,\infty}(\mathbb{R}),\ \lambda \mapsto \beta(\lambda) \text{ is even on } \mathbb{R}, \\ \lambda \mapsto \lambda\beta'(\lambda) \quad \text{belongs to } L^\infty(\mathbb{R}), \\ 0 \le \beta(\lambda) \le 1, \quad \beta \text{ is non decreasing on } (0,+\infty), \\ \lim\limits_{\lambda\to+\infty} \beta(\lambda) = 1. \end{cases} \tag{23}$$

Note that the characteristic times of X are intrinsic to the membrane, unlike (17), and X takes its values in $(0,1)$. The Kirchhoff law is then given by

$$\mathrm{C_m}\partial_t V_\mathrm{m} + (\mathrm{S_0} + \mathrm{S_1} X\,(t, V_\mathrm{m}))\, V_\mathrm{m} = \sigma_\mathrm{c}\partial_n U|_{\Gamma^-}. \tag{24}$$

It is worth noting that our new model involves only 4 parameters: k, $\mathrm{V_{ep}}$, and the two characteristic times τ_ep, τ_res, compared to the 8 parameters of the KDN–model. In addition, the membrane conductivity is bounded between the conductivity at rest $\mathrm{S_0}$ and the the porated state $\mathrm{S_1}$, whereas the pore density N_ep of the KDN–model is *a priori* unbounded. We eventually point out that after the electric shock, the membrane resealing τ_res has been measured around tens of microseconds by Benz *et al.* [9] for planar bilayer, while the KDN–model predicted a membrane resealing given by $\alpha/N_o \sim 1\mathrm{s}$ as stated in [32].

3.2. Theoretical results. In [56], we prove the well–posedness of the electric potential U solution to the following problem:

$$U|_{t=0} = U_0, \quad \text{and for any } t > 0,$$

$$\Delta U = 0, \quad \text{in } (0,T)\times(\mathcal{O}_\mathrm{e}\cup\mathcal{O}_\mathrm{c}), \qquad U(t,\cdot) = g(t,\cdot) \quad \text{on } (0,+\infty)\times\partial\Omega, \tag{25a}$$

$$[\sigma\partial_\mathbf{n} U] = 0, \quad \text{on } (0,T)\times\Gamma, \tag{25b}$$

and with the Kirchhoff law, which reads

$$\mathrm{C_m}\partial_t V_\mathrm{m}(t,\cdot) + S_\mathrm{m}(t,V_\mathrm{m})V_\mathrm{m} = \sigma_\mathrm{c}\partial_\mathbf{n} U(t,\cdot)_{|_{\Gamma^-}}, \quad \text{on } (0,T)\times\Gamma, \tag{25c}$$

where $V_\mathrm{m} = [U]$ is the transmembrane voltage and where S_m is given by (20). In order to prove existence and uniqueness of the solution to our model, we use appropriate Dirichlet–to–Neumann operators to write our PDEs on the surface membrane.

Definition 3.1 (Steklov–Poincaré operators). *Denote by Λ_c and Λ_e the Dirichlet–to–Neumann operators on Γ (also called Steklov–Poincaré operators) for the Laplacian respectively in $\mathcal{O}_\mathrm{c}$ and in $\mathcal{O}_\mathrm{e}$. We define the operators Λ_c and Λ_e from $H^{1/2}(\Gamma)$ to $H^{-1/2}(\Gamma)$ as:*

$$\forall f \in H^{1/2}(\Gamma), \quad \Lambda_\mathrm{c}(f) := \mathbf{n}_\mathrm{c}\cdot\sigma_\mathrm{c}\nabla v_{\mathrm{c}_{|_{\Gamma^-}}},\ \text{where } \nabla\cdot(\sigma_\mathrm{c}\nabla v_\mathrm{c}) = 0 \text{ in } \mathcal{O}_\mathrm{c},\ \text{and } v_{\mathrm{c}_{|\Gamma}} = f, \tag{26a}$$

$$\Lambda_\mathrm{e}(f) := \mathbf{n}_\mathrm{e}\cdot\sigma_\mathrm{e}\nabla v_{\mathrm{e}_{|_{\Gamma^+}}},\ \text{where } \nabla\cdot(\sigma_\mathrm{e}\nabla v_\mathrm{e}) = 0 \text{ in } \mathcal{O}_\mathrm{e},\ v_{\mathrm{e}_{|\partial\Omega}} = 0 \text{ and } v_{\mathrm{e}_{|\Gamma}} = f. \tag{26b}$$

Moreover, for a function $g \in H^{1/2}(\partial\Omega)$, we define $\Lambda_0(g)$ by

$$\Lambda_0(g) := \mathbf{n}_\mathrm{e}\cdot\sigma_\mathrm{e}\nabla v_{|_{\Gamma^+}}, \quad \text{where } \nabla\cdot(\sigma_\mathrm{e}\nabla v) = 0 \text{ in } \mathcal{O}_\mathrm{e}, \quad v_{|\partial\Omega} = g \text{ and } v_{|\Gamma} = 0. \tag{26c}$$

Since Λ_e and Λ_c are non–negative self–adjoint operators from $H^{1/2}(\Gamma)$ into $H^{-1/2}(\Gamma)$, and since Λ_e is invertible in addition, we denote by $\mathcal{B}$ the positive slef–adjoint and invertible operator defined from $H^{1/2}(\Gamma)$ into itself by

$$\mathcal{B} = \mathrm{Id} + \Lambda_\mathrm{e}^{-1}\Lambda_\mathrm{c}.$$

Thanks to these operators, one has the following lemma, which makes it possible to write the problem in Ω on the surface membrane Γ:

LEMMA 3.2 (Equivalent problems [56]). *Let U_0 and X_0 be two functions regular enough, that are defined respectively in Ω and on Γ, and let $S_{\rm m}$ be defined by* (20).

Finding the solution (U, X) to problem (25)–(20)*, if it exists, is equivalent to finding $(u_{\rm e}, u_{\rm c}, X)$, with $u_{\rm e} = U_{|\Gamma^+}$ and $u_{\rm c} = U_{|\Gamma^-}$ satisfying:*

$$u_{\rm e} = u_{\rm c} - V_{\rm m}, \tag{27}$$

$$u_{\rm c} = \mathcal{B}^{-1}\left(V_{\rm m} - \Lambda_{\rm e}^{-1}\Lambda_0 g\right), \tag{28}$$

where $V_{\rm m}$ is the solution to

$$\begin{aligned} &{\rm C_m}\partial_t V_{\rm m} + \Lambda_{\rm c}\mathcal{B}^{-1}V_{\rm m} + S_{\rm m}(t, V_{\rm m})V_{\rm m} = G, \\ &V_{\rm m}(0,\cdot) = \phi, \end{aligned} \tag{29}$$

with ϕ and G being defined as

$$\phi = U_{0_{|\Gamma^+}} - U_{0_{|\Gamma^-}}, \quad G := \Lambda_{\rm c}\mathcal{B}^{-1}\Lambda_{\rm e}^{-1}\Lambda_0 g.$$

Thanks to this lemma, using the m–accretivity of $\mathcal{B}$, and the Lipschitz property of X with respect to its second variable, we infer the well–posedness of our problem.

THEOREM 3.3 (Theorem 10 of [56]). *Assume that β satisfies* (23)*, $G \in L^p((0,T); L^2(\Gamma))$ for some $p > 1$, and that $\phi \in L^2(\Gamma)$ is given. Let $X_0 \in L^\infty(\Gamma)$ such that $0 \le X_0 \le 1$ on Γ.*

Then, there exists a unique function $V_{\rm m} \in C([0,T]; L^2(\Gamma))$, mild solution to

$$\begin{cases} {\rm C_m}\partial_t V_{\rm m} + \Lambda_{\rm c}\mathcal{B}^{-1}V_{\rm m} + S_{\rm m}(t, V_{\rm m})V_{\rm m} = G, & in\,(0,T)\times\Gamma, \\ \dfrac{\partial X(t, V_{\rm m})}{\partial t} = \max\left(\dfrac{\beta(V_{\rm m}) - X(t, V_{\rm m})}{\tau_{\rm ep}}; \dfrac{\beta(V_{\rm m}) - X(t, V_{\rm m})}{\tau_{\rm res}}\right), & t > 0, \\ V_{\rm m}|_{t=0} = \phi, \quad X|_{t=0} = X_0. \end{cases} \tag{30}$$

Moreover, if $\phi \in H^1(\Gamma)$ and $G \in W^{1,1}((0,T); L^2(\Gamma))$, the above mild solution is a classical solution to (30)*, in the sense that*

$$V_{\rm m} \in C([0,T]; H^1(\Gamma)) \cap C^1([0,T]; L^2(\Gamma)).$$

3.3. Numerical methods. We choose to use schemes on cartesian grids, such as the scheme of M. Cisternino and L. Weynans [22], for which the accuracy has been shown and the parallelization has be already performed. We emphasize that the choice of the numerical methods is driven by the will to benefit from the skills of the research team MC2.

The time–derivative $\partial_t[U]$ of (25) is discretized using the following scheme:

$${\rm C_m}\frac{V_{\rm m}^{n+1} - V_{\rm m}^n}{dt} - \sigma_{\rm c}\partial_{\mathbf{n}}U_{\rm c}^{n+1} + \widetilde{S}_{\rm m}(t^n, V_{\rm m}^n)V_{\rm m}^n = 0. \tag{31}$$

Note that it is important to implicit the term $\partial_{\mathbf{n}}U_{\rm c}$ to avoid a restrictive stability condition as in [46]. Therefore we derived a modification of the scheme of Cisternino and Weynans. Fourth order Runge–Kutta method is used to compute X, with the time step dt. We perform the discretization on a cartesian grid covering the domain $\Omega = \mathcal{O}_{\rm e} \cup \overline{\mathcal{O}_{\rm c}}$, which is a square domain of length L. The interface is described by a level–set function [77], which separates the extra- and intra–cellular domains by the use of a signed distance function φ. The normal to the interface $\mathbf{n}(x)$ outwardly directed from the inner to the outer of the cell is directly obtained by computing numerically $\nabla\varphi(x)$. The grid spacing is denoted by h, and N is the number of points such as

$$N = L/h.$$

For any $(i,j) \in N^2$ we denote by M_{ij} the grid points defined by

$$M_{ij} = (x_i, y_j), \quad \text{where} \quad x_i = ih_x,\ y_j = jh_y, \quad \forall (i,j) \in N^2.$$

The numerical approximation of the solution U at the point (x_i, y_j) is generically denoted by u_{ij}.

Standard approximation of the Laplacian is used in the discretized domains $\mathcal{O}_{\rm e}$ and $\mathcal{O}_{\rm c}$ far from the interface, which is the cell membrane Γ. However, due to the jump conditions, a special treatment of the

approximation of the Laplacian and of the computation of the fluxes is needed at the points nearing the cell membrane.

If the intersection of the interface and $[M_{ij}\, M_{i+1j}]$ exists, then we denote by $I_{i+1/2,\,j}$ the interface point at this intersection and we set $I_{i+1/2,\,j} = (\tilde{x}_{i+1/2\,,j}, y_j)$. We create two additional unknowns at this interface point, called interface unknowns, and denoted by $\tilde{u}^{\rm e}_{i+1/2\,,j}$ and $\tilde{u}^{\rm c}_{i+1/2\,,j}$. The interface point $I_{i,\,j+1/2} = (x_i, \tilde{y}_{i,\,j+1/2})$ is similarly defined as the intersection of Γ and the segment $[M_{ij}M_{ij+1}]$.

An example of the discretization method is given by Figure 4. On regular grid points, that are not neighboring the interface, the Laplacian is discretized with a standard centered second–order finite difference scheme. A specific five points stencil including the interface points is used for neighboring points, as shown in Figure 4(a).

Figure 4(b) provides an example of the discretization of ∇U on both sides of the interface. The x–derivative of U can be computed with second order accuracy using a one–sided formula involving three grid points. For example we approximate the flux on the left-hand side of the interface, for instance in the exterior medium, with the points M_{i-1j}, M_{ij} and $I_{i+1/2\,,j}$ by

$$\frac{\partial U}{\partial x}(\tilde{x}, y_j) \approx \frac{(u_{i-1j} - \tilde{u}^{\rm e}_{i+1/2\,,j})(x_i - \tilde{x})}{h_x(x_{i-1} - \tilde{x})} - \frac{(u_{ij} - \tilde{u}^{\rm e}_{i+1/2\,,j})(x_{i-1} - \tilde{x})}{h_x(x_i - \tilde{x})}, \tag{32}$$

where for the sake of brevity, we have replaced $\tilde{x}_{i+1/2\,,j}$ by $\tilde{x}$. The y–derivative cannot be obtained in the same way, since there are no grid points aligned with the interface point in the y–direction. We therefore use a linear combination of $(\partial_y u)_{ij}$ and $(\partial_y u)_{i-1j}$, defined respectively as second order approximations of the y–derivative on M_{ij} and M_{i-1j}:

$$\frac{\partial U^{\rm e}}{\partial y}(\tilde{x}, y_j) \quad \approx \quad \frac{\tilde{x} - x_{i-1}}{h_x}\,(\partial_y u)_{ij} - \frac{\tilde{x} - x_i}{h_x}\,(\partial_y u)_{i-1j}. \tag{33}$$

The formulas for $(\partial_y u)_{ij}$ and $(\partial_y u)_{i-1j}$ depend on the local configuration on the interface, but they are based on the same principle as for (32). The scheme is stabilized by using a shifted y–stencil if two interface points are involved in the same flux discretization, as illustrated by Figure 4(c).

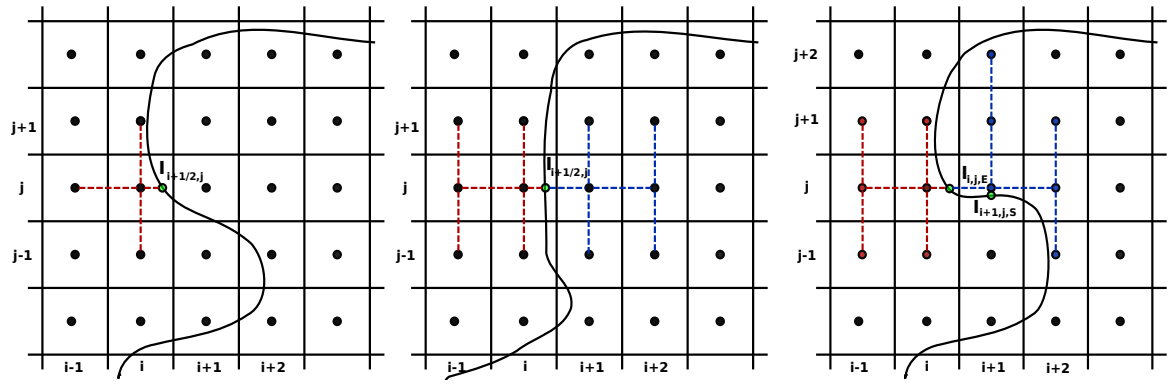

(a) Discretization of the Laplacian on the points at the interface.

(b) Discretization of ∇U at the interface: non–stabilized stencil.

(c) Discretization of ∇U at the interface: stabilized stencil.

FIGURE 4. Discretizations of the Laplacian and of the gradient of U at the interface. The first y–derivative stencil on the right side is shifted to avoid an ill conditioned discretization.

3.4. Numerical results. Figure 5(a) and 5(b) show the numerical results at $t = 100$ μs using the parameters of Table 1 of [56]. In order to visualize the membrane electropermeabilization, we depict it with boxes, which are colored and sized according to the values of $S_{\rm m}$ at each point of Γ and at $t = 100$ μs. We emphasize this is a visualization artefact: in our model, the cell membrane is a surface without any thickness.

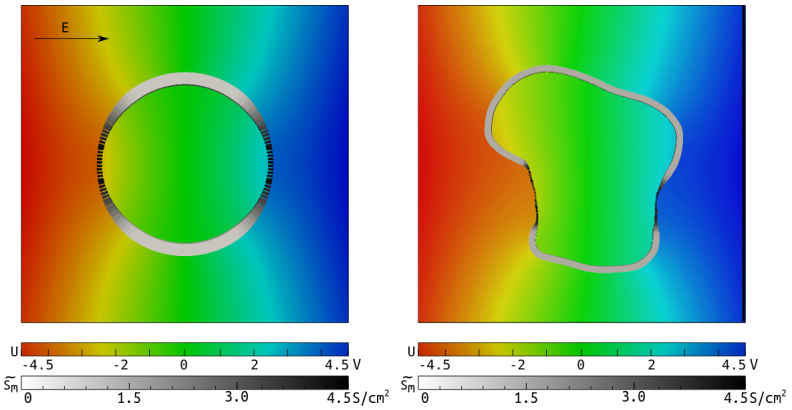

(a) Solution to the dynamical model for a circular cell.

(b) Solution to the dynamical model for a smooth non–convex cell shape.

FIGURE 5. Solution to the dynamical problem with two different cell shapes at $t = 100$ μs. Figure 5(b) shows that the electropermeabilized regions depend on the shape and orientation of Γ.

3.4.a. *Main parameters influence.* The parameters of the model define the electropermeabilization coefficient $S_{\rm m}$, that is k, $V_{\rm rev}$, S_1 and the characteristic times $\tau_{\rm ep}$ and $\tau_{\rm res}$. A numerical sensitivity analysis was led to determine how the behavior of the solution with respect to a variation of each specific parameter, as shown on Figure 6. All the parameters defining the function β have a very small influence on the average $\overline{X}$ of X over the cell membrane. Even for small values of k, the values of $\overline{X}$ are only modified by a factor 2 (Figure 6(a)). On the other hand, the "fully electroporated" membrane conductivity S_1, which was first taken as $(\sigma_{\rm c} + \sigma_{\rm e})/(2\delta)$, affects greatly the order of magnitude of $\overline{X}$, changing from 10^{-6} to 10^{-2} (Figure 6(d)). Therefore, it appears that the relevant quantity to observe the phenomenon is the membrane conductivity $S_{\rm m}$ and not only the function X.

3.4.b. *Comparison with the KDN–model for classical micropulses.* Even though the KDN–model presents some drawbacks that we pointed out previously, it has been extensively used and provides qualitative results in accordance with the experiments, at least for "classical" pulses. In particular, for micropulses, that last several hundreds of microseconds, or for millipulses, this model is considered as the most achieved model. Therefore, it is important to check whether our model can provide results that are similar to the KDN–model for such pulses.

The main difference between these two models resides in the description of the electroporation in Kirchhoff law. In KDN model, an electroporation current $I_{\rm ep} = N_{\rm ep} i_{\rm ep}$ is added to the linear Kirchhoff law (13c), while we prefer a direct description of the variations of the surface membrane conductivity $S_{\rm m}$, as given by (20).

The link between the two models can be obtained thanks to a Taylor expansion of $i_{\rm ep}$ given by (18) around $\nu \sim 0$, one has

$$i_{\rm ep}(\nu) \sim_{v\to 0} \mathrm{C}_{\rm ep} \nu \frac{F}{RT}, \quad \text{with} \quad \mathrm{C}_{\rm ep} = \frac{\sigma}{\delta} \frac{\pi r_{\rm m}^2 w_o e^{-w_o}}{w_o + 2\cosh(w_o)}, \tag{34}$$

and thus the Kirchhoff law with KDN–model (19) leads to

$$\mathrm{C}_{\rm m} \partial_t V_{\rm m} + (\mathrm{S}_0 + \mathrm{C}_{\rm ep} N_{\rm ep}(t, V_{\rm m}))\, V_{\rm m} = \sigma_{\rm c} \partial_n U|_{\Gamma^-}. \tag{35}$$

Hence the term $\mathrm{C}_{\rm ep} N_{\rm ep}(t, V_{\rm m})$, whose unit are homogeneous to a surface conductivity, corresponds to our term $\mathrm{S}_1 X(t, V_{\rm m})$. The values of the parameters of the KDN–model are given in Table 1 of [56].

For micropulses, our model reproduces qualitatively the behavior of transmembrane voltage as shown in Figure 7. The differences between the two models are not very significant since the KDN–model has been validated qualitatively and not quantitatively. In addition to the transmembrane voltage, it is important

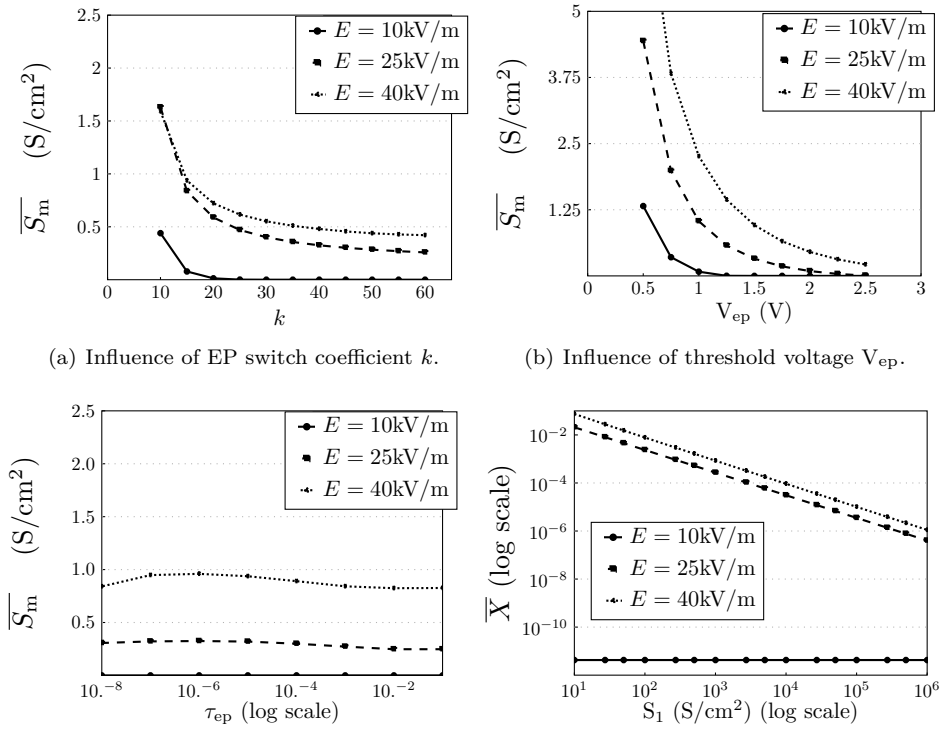

(a) Influence of EP switch coefficient k.

(b) Influence of threshold voltage V_{ep}.

(c) Influence of the characteristic time τ_{ep}.

(d) Influence of the EPd surface conductivity S_1.

FIGURE 6. Influence of each parameter on the mean value $\overline{S_{\rm m}}$ of $S_{\rm m}$ (Figure 6(a)–6(b)–6(c)), and on the mean value $\overline{X}$ of X (Figure 6(d)) at $t = 100$ μs. Three magnitudes of electric pulses are considered: 10, 25 and 40 kV/m.

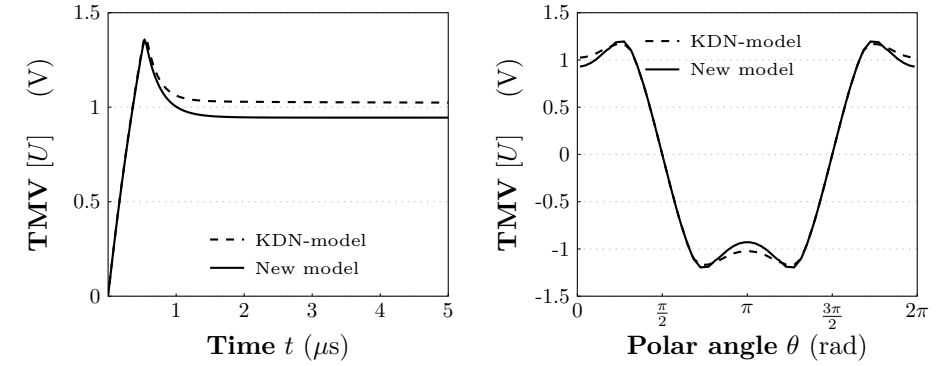

(a) Evolution of the ΔTMP at the cell's pole.

(b) Values of the ΔTMP after 100 μs along the perimeter of the circular cell.

FIGURE 7. Comparison of the ΔTMP obtained respectively with our model (solid lines) and with the model of Neu, Krassowska, *et al.* (dashed) (see [56] for more details).

to check whether the current density due to electroporation are similar for both models, since this is the physical quantification of membrane electroporation. Figure 8 shows that the variation of the membrane current density $S_{\rm m}[U]$ of the two models are similar.

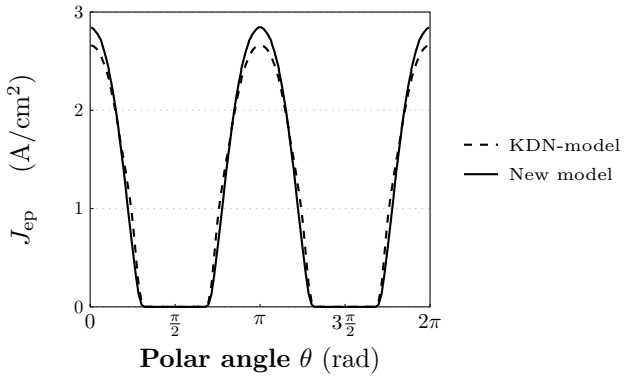

FIGURE 8. Current density through the membrane of the model of Neu, Krassowska, *et al.*, that is $J_{\rm ep} = N_{\rm ep} i_{\rm ep}$ (in dashed line), compared with the membrane current density of our model (in solid line), $J_{\rm ep} = \mathrm{S}_1 X\, V_{\rm m}$, along the the cell membrane at 100 μs.

Therefore we have shown that for "classical" pulses, meaning for pulses longer than 100μs, the two models provide similar results, which justifies the use of our new model, since it involves much less parameters. This first step in the validation of our model has to be completed by a comparison with the experiments.

3.5. Comparison with the experiments. In order to verify the consistency of our electrical modeling, we perform a few comparisons with experiments. The next results are very preliminary, and should be investigated in forthcoming research, but somehow, they provide a first step in fitting the model.

Two kinds of experiments have been used with two different collaborators. We first present the patch–clamp results done on BY2 cells by L. Wegner from KIT, and then, we present the experiments done by A. Silve at the cancer research Institute Gustave Roussy and then at KIT on the impact of the conductivity of the external solution on the DC3F cell permeabilization.

3.5.a. *Fitting with patch–clamp experiments.* The patch–clamp technique is a laboratory technique that has been developed in electrophysiology, originally in order to study single or multiple ion channels in excitable cells. The idea consists in micropipetting the cell membrane in order to have access to the cell cytoplasm. It is thus possible to impose a voltage potential across the cell membrane: the cell membrane is then uniformly charged and its physiological response is tracked thanks to the electric current measurements. This method has been extensively used for excitable cells such as axons but its application to electroporation has appeared very recently. Actually, the first papers dealing with patch–clamp and electroporation have been published in the last ten years, as mentioned by Wegner *et al.* in [120].

The principles of the method are presented in Figure 9. Roughly speaking, patch–clamp makes it possible to charge uniformly the membrane by imposing a transmembrane voltage as described in Figure 9(c). From the measurement of current, it is then possible to quantify the increase of membrane conductivity. We do not describe the drawbacks of the technique – in particular the influence of the seal effect, due the sticking of the membrane on the micropipette, which are presented in [120] – but we present preliminary comparisons of the numerical results with the experimental data.

In [120], Wegner *et al.* track the electroporation in BY2 cells that are a specific tobacco cell line with a non–zero transmembrane voltage, by imposing millipulses of 10 ms. Typically, rectangular pulses of different amplitudes are applied, and the current responses of the membrane are measured instantaneously. For instance Figure 10 shows a command voltage of 160mV during 10 ms and the corresponding electric intensity[2].

For "low" voltages, roughly speaking for voltage below 300mV, the membrane response is similar to a simple capacitor with specific capacitance and resistance. But for higher voltages, an electroporation current appears in the measures.

[2]It is worth noting that the voltage of Figure 10 is not the membrane potential but the command voltage.

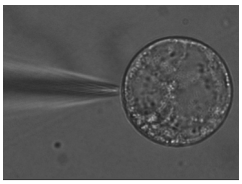

(a) BY2 cell patch–clamped

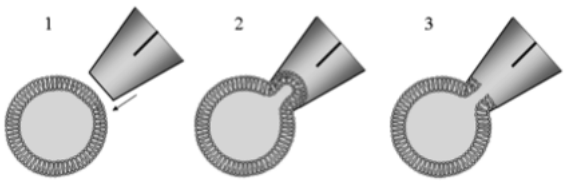

(b) The 3 steps of patch–clamp

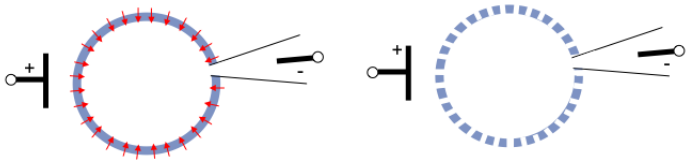

(c) Schematic representation of membrane during patch–clamp

FIGURE 9. Principle of the patch–clamp experiments (courtesy of L. Wegner).

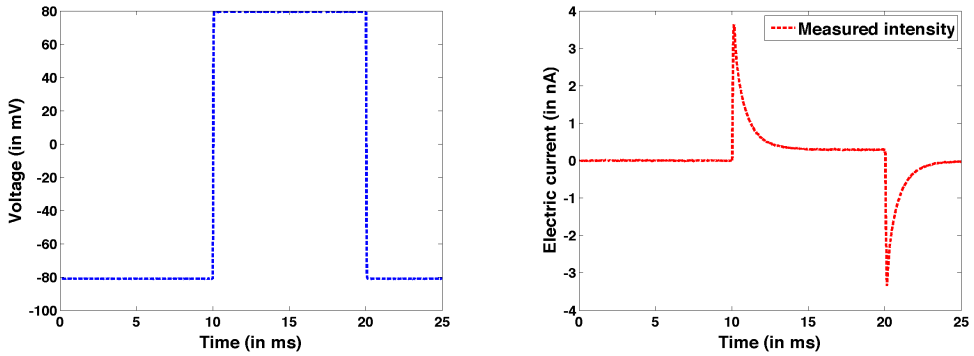

FIGURE 10. Command voltage of 160 mV during 10 ms, and the corresponding measured electric current. One can see the resting potential of the cell at -81mV, and the linear response of the membrane which behaves as a capacitor.

These data provide a nice tool to choose appropriately the parameters of our electroporation model, however, in order to link experiments and numerics, we have to adapt slighty our model. Actually, the radius of the micropipette and the cell geometry are not precisely know, so it is inconceivable to compute the model in 3D in order to have a rough estimation of the model parameters. Moreover, note that patch–clamp provides global current, while our model is local.

The simplest way to model patch–clamp configuration consists in assuming that the cells are spherical, which is acceptable since they are in suspension in the solution: this makes it possible to take advantage of the rotational invariance of the problem, since the membrane is uniformly charged. The cell is thus supposed to be a sphere of radius R_c centered at the origin and embedded in an infinite domain. The command voltage and the high resistance seal effect on the potential is mimicked by a spherical source g of radius R_s located at the origin. BY2–cells are plant cells with a non–zero transmembrane voltage v_0, which has to be taken into account in the Kirchhoff law, which is about -81mV, as given by the experiments (see Figure 10).

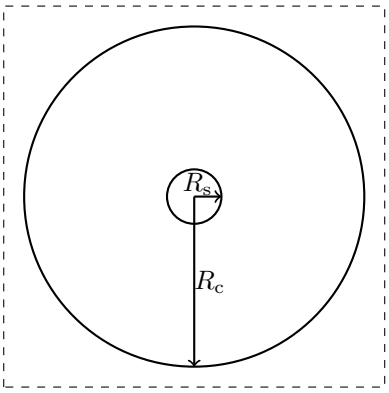

FIGURE 11. Geometry for patch–clamp.

The model reads as follows:

$$\begin{aligned}
&\Delta U = 0, \qquad \text{if } R_s \le r \le R_c \text{ or } R_c \le r,\\
&\sigma_e \partial_r U|_{r=R_c^+} = \sigma_c \partial_r U|_{r=R_c^-},\\
&C_m \partial_t V_m + S_m(t, V_m)(V_m + v_0) = \sigma_c \partial_r U|_{r=R_c^-},\\
&U|_{r=R_s} = g(t), \quad \lim_{r\to+\infty} U = 0, \quad V_m|_{t=0} = -v_0,\\
&\text{with the convention} \quad V_m = [U].
\end{aligned}$$

Since the command voltage g does not depend on the angle, the flux $\sigma_c \partial_r U|_{r=R_c}$ reads:

$$\sigma_c \partial_r U|_{r=R_c^-} = -(V_m + g) \Big/ \left(\frac{R_c}{\sigma_e} + \frac{R_c}{\sigma_c}\left(\frac{R_c}{R_s} - 1\right)\right),$$

and thus the membrane potential V_m satisfies[3]:

$$I(t) := C_m \partial_t V_m + S_m(t, V_m)(V_m + v_0) = -(V_m + g) \Big/ \left(\frac{R_c}{\sigma_e} + \frac{R_c}{\sigma_c}\left(\frac{R_c}{R_s} - 1\right)\right). \tag{36}$$

Since the patch–clamp technique consists in imposing a voltage and in order to measure the current, it is thus possible to compare the measure intensity with the theoretical current I. The configuration of the experimental setup possible to have an estimate of the inner and the outer conductivities σ_c and σ_e as well as the cell radius R_c:

$$\sigma_c = 2\,\mathrm{S/m}, \quad \sigma_e = 0.5\,\mathrm{S/m}, \quad R_c = 15\,\mu\mathrm{m}.$$

In addition to the electroporation model parameters, the radius corresponding to the gigaseal R_s is a crucial parameter. In the linear regime, the membrane capacitance C_m and the membrane conductivity at rest S_0 have been evaluated at

$$C_m = 0.006\,\mathrm{F/m^2}, \quad S_0 = 0.74\,\mathrm{S/m^2},$$

which made it possible to fix R_s to 40 nm. We then found the parameters of the non–linear part, for β given by (22):

$$\tau_{ep} = 0.01\,\mathrm{s}, \quad \tau_{res} = 0.002\,\mathrm{s}, \quad V_{ep} = 0.86\,\mathrm{V}, \quad S_1 = 8000\,\mathrm{S/m^2}, \quad k = 2.5,$$

for which the fit with the data is quite satisfactory as shown by Figure 12. Note that these parameters are physically significant, with a transmembrane voltage threshold of 0.86 V, which is close to the theoretical threshold of 1 V predicted by the molecular dynamics simulations [108, 104] as well as by the biophysical models [119, 118]. The porated membrane conductivity S_1 is ten thousands times higher than the membrane conductivity at rest, which is plausible.

We tried to obtain similar results with the KDN–model, however the sensitivity to the parameters was to high, in particular in the definition of i_{ep}, to obtain satisfactory results, moreover taking the parameters directly from [32] provides non–relevant results. The only successful way to obtain quantitative results with the KDN–model consists in using the linearization of i_{ep} given by (34), and to consider C_{ep} as a parameter to be fixed. However even with this simplification, the model does not provide satisfactory results, since it makes appear electroporation currents between 0 and 10ms while nothing is detected by the experiments, and after the pulse the theoretical intensity is overestimated as shown by Figure 13 for a pulse amplitude of 600mV. Therefore our phenomenological model seems to provide results in agreement with the experiments

[3]Note that in (36), the fix point of the O.D.E. is $-v_0$ instead of v_0. This is due to the convention: we chose to define the membrane voltage as the jump of U, meaning $V_m = [U] = U_{\Gamma+} - U_{\Gamma-}$ while in electrophysiology, it is defined as the opposite of the jump $U_{\Gamma-} - U_{\Gamma+}$.

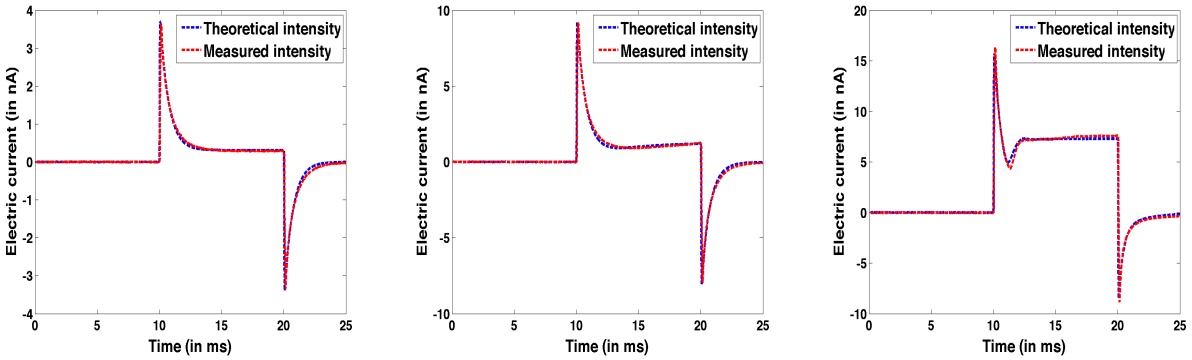

(a) 80mV is applied (b) 320mV is applied (c) 600mV is applied

FIGURE 12. Validation of the model by comparisons with patch–clamp data.

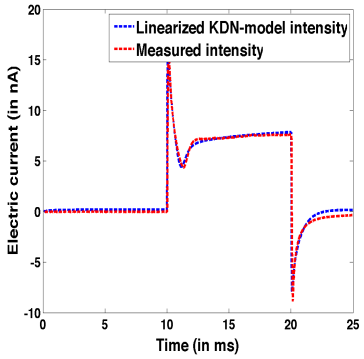

FIGURE 13. Linearized KDN model compared with the experiments for 600mV pulse amplitude (to be compared with Figure 12(c). Electrical intensity of overestimated before and after the electric shock: electroporation is predicted while nothing is detected.

at least for millipulses, with the advantage of involving a very few parameters compared with the classical KDN–model.

Note also that for millipulses, and for micropulses, as stated in [32], the two models provide quite similar behavior of the membrane, and even though the KDN–model seems to be hardly fittable, the predicted behaviours are relevant. In particular, from these patch–clamp experiments it is not possible to discriminate between an intrinsic behaviour of the membrane, with specific characteristic times as in our model and a membrane response only driven by the membrane potential, as in the KDN–model. The use of other experiments, using nanopulses made it possible to provide preliminary answer to this question.

3.5.b. *The nanopulse paradox.* A. Silve from KIT and L.M. Mir's group of IGR have studied the influence of the solution conductivity of DC3F cell, a chinese ovary cell line, on the cell permeabilization by nanopulses. Several groups have studied the influence of conductivity on the efficiency of cell permeabilization [73, 103, 88] for micropulses or millipulses. As stated by Ivorra *et al.* in [52], the general conclusion of those studies is that a decrease of the extracellular medium conductivity slightly decreases the efficiency of the permeabilization. Such an influence is however very weak and can only be observed only for very low values of conductivity, typically less than 0.01 S/m, which is far from the physiological conditions.

The aim of Silve and Mir's work is to investigate whether similar results hold for nanopulses. The experimental protocol is the following. Cells are put in suspension in two different aequous solutions: a conducting solution, with a conductivity of 1.5 S/m and a non–conducting solution whose conductivity is decreased to

0.1 S/m. Each solution contains a cytotoxic molecule: the bleomycin, which is non–permeant in non electroporated cells but which kills the cell as soon as it reaches the cytoplasm. The cell electropermeabilization is then detected by counting the number of survival cells.

They applied 3 types of nanopulses. Pulse A is 12 ns long with an amplitude of 3.2 MV/m, Pulse B is 12 ns long with an amplitude of 14.2 MV/m and Pulse C is 102 ns with an amplitude of 3.2 MV/m, as given by Figure 14. Unlike the observations for micro– or milli–pulses, their results highlight an influence of the conductivity in a strange way.

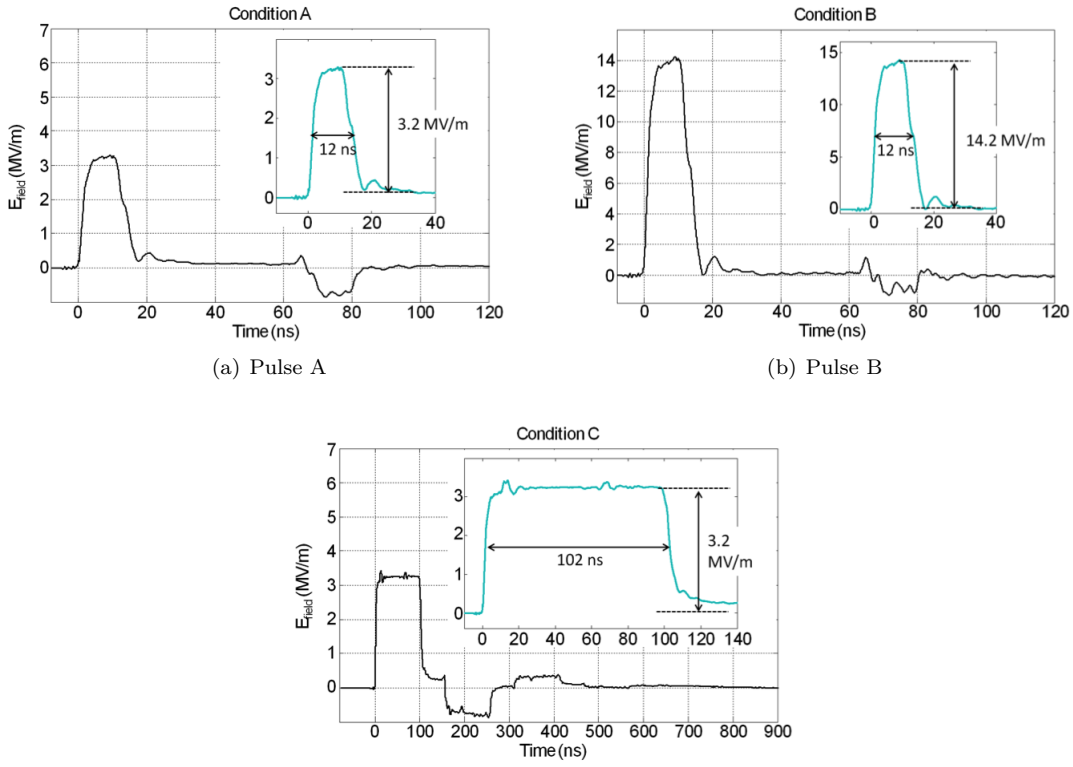

(a) Pulse A

(b) Pulse B

(c) Pulse C

FIGURE 14. Profiles of the three nanopulses used to study the influence of the conductivity on the cell electropermeabilization.

More precisely, for Pulse A, one hundred pulses are necessary to permeabilize the cells in the conducting solution, while even thousand pulses do not affect the cells in the resistive medium, as reported by Figure 15. It is also worth noting that electric shock with less than hundred pulses A do not affect the cells.

For the two other pulses, the results are drastically different. In particular, even only one pulse of type B or C permeabilized almost all the cells of the resistive solution, while the same single pulse does not affect the cells of the conducting solution, as reported in Figure 16. In order to verify whether or not the models predict at least quantitatively these quite striking results, we investigate the electroporation current of the KDN–model and our model of membrane conductivity for the three different pulses.

It appears that even though the KDN–model has been validated qualitatively for micro- and milli–pulses, it cannot be in agreement with the electropermeabilisation by nanopulses. The main reason lies in the fact that according to (17), the dynamics of the pore creation is linked to the instantaneous value of the membrane voltage by the term $\frac{\alpha}{N_o} e^{(1-q)(V/V_{ep})^2}$, providing higher values of N for conducting media, as described by Figure 17, whatever the pulse is. On the contrary, our model supposes that the cell membrane permeabilization has its instrinsic dynamics characterized by the parameter τ_{ep} for the permeabilization

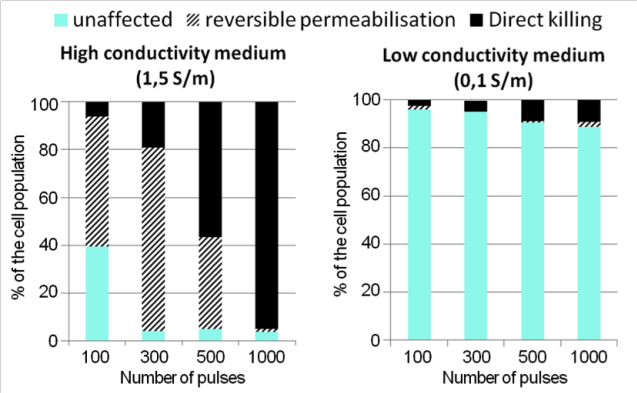

FIGURE 15. Percentage of affected and unaffected cells by the pulse A for the two solutions. With less than 100 pulses, no cell is affected in the two solutions.

characteristic time, and by τ_{res} for the resealing characteristic time. We emphasize that these characteristic times do not depend on the membrane voltage.

For micropulses, as reported by Figure 4 of [56], the membrane conductivity is weakly affected by the medium conductivity, which is in accordance with the experiments. However for nanopulses the results are drastically different. We impose exactly the same pulses as given by Figure 14. As we can see in Figure 18, the average of the membrane conductivity is not necessarily higher in the conducting solution. It can be explained as follows: the increase of membrane conductivity, due to its intrinsic behaviour, needs that the transmembrane voltage is above the threshold value during a minimum time. In the high conducting medium, the discharge of the membrane is as fast as the charging time: the membrane voltage reaches a much higher value than the threshold but during a too small time, while in the resistive solution, the membrane voltage reaches the threshold value and stays above it during a longer time thanks to a low discharge as illustrated in Figure 19.

Note that since the characteristic times are quite small, for pulses of several hundreds of microseconds, the two solutions lead to the same percentage of permeabilizaed cells. This could explain why the influence of the medium conductivity is weak for classical pulses.

We thus have presented two different experimental studies for which our model provides corroborating results. For path–clamp experiments the results are quantitatively in accordance with the experiments while for nanopulses, the results are qualitatively in agreement with the biological data.

However, we have to point out here a crucial fact: in the model permeabilized and conducting states are identified. This a shortcut is known to be false. Actually, even though the increase of membrane permeability is a consequence of the electric shock, the internalization of molecules into the cytoplasm cannot be described by the conducting state of the membrane. More precisely, it has been experimentally observed that the cell membrane may remain permeable several tens of minutes after the electric pulses delivery, while experiments by Benz, Zimmerman *et al.* [9] have reported that the membrane conductivity recovers almost entirely its initial value within several microseconds after the end of the pulse. From the modeling point of view, it is therefore important to distinguish the electric phenomenon, which leads to the increase of membrane conductivity, from the transport of molecules across the permeable membrane. In the next section, we add a model of membrane permeability to our electrical model, in order to make up for these shortcomings.

4. The membrane permeability

Since the experimental detection of cell electropermeabilization is mainly based on the internalization of non permeant molecules – such as propidium iodide (PI)[4] or DNA – into cells or vesicles, it is necessary to

[4]PI is a small molecule which is fluorescent inside the cytoplasm of the cell. It is thus a good fluorescent marker of membrane electropermeabilization.

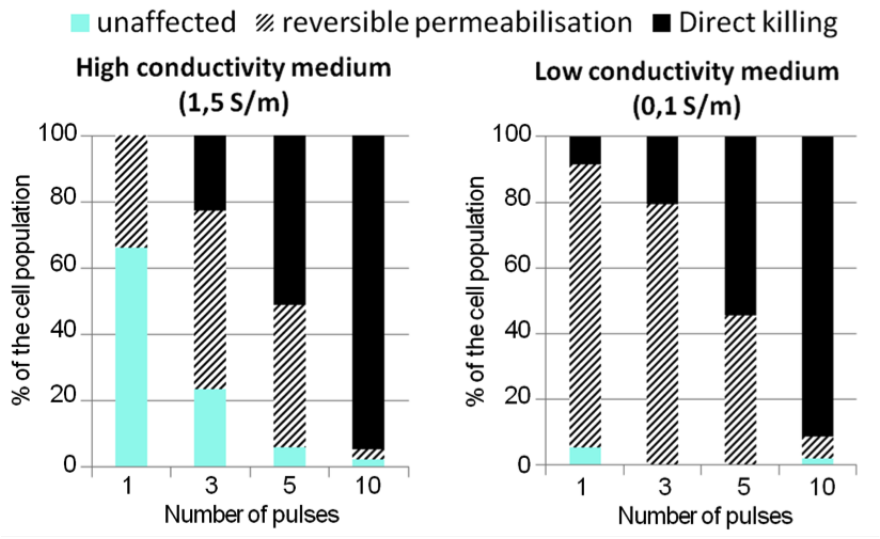

(a) Percentage of affected cells with the pulse B

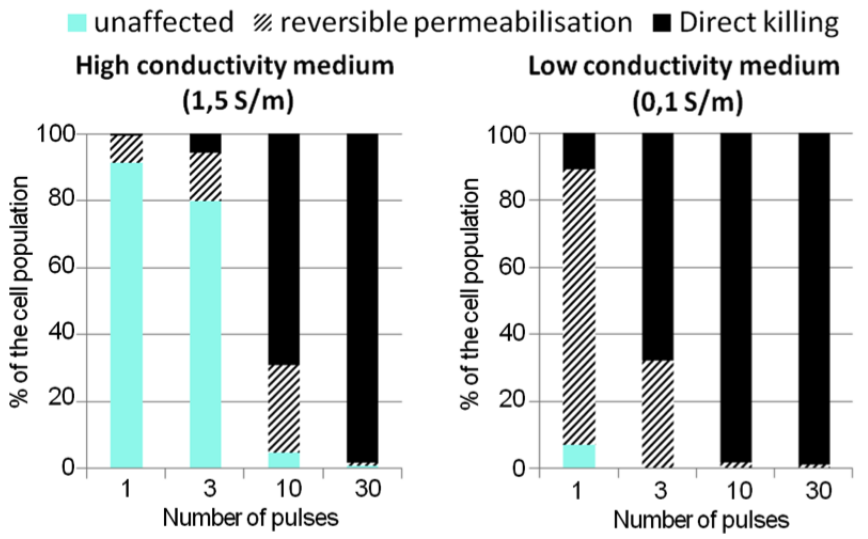

(b) Percentage of affected cells with the pulse C

FIGURE 16. Percentage of affected and unaffected cells by the pulses B and C. Only one single pulse permeabilizes almost all the cells of the resistive solution, and while it does not affect the cells of the conducting bath.

derive a model that describes the motion of these molecules around and inside the cell. The results of this section have been presented in [62].

4.1. Description of the model. Our transport model has to take the two main modes of molecule transport into account: the passive diffusion for small molecules such as PI and the electrophoresis for charged molecules such as DNA. We assume that the electrophoretic forces is given by $-\mu\nabla u$ where μ being the electrical motility of the molecule M in $\mathcal{O}_e \cup \mathcal{O}_c$. In order to ensure the continuity of $\mu\nabla u$ across the interface, we choose μ as follows

$$\mu(x) = \frac{1}{2}\sigma(x)\left(\alpha_e + \alpha_c - (\alpha_e - \alpha_c)\tanh(K\,\mathrm{dist}(x,\Gamma))\right),$$

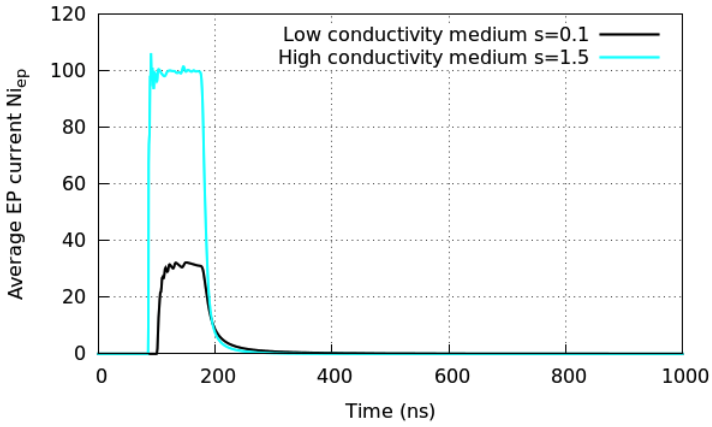

FIGURE 17. Electroporation current of the model of Krassowska and Neu for the two types of condutivity, when the pulse C is applied. The electroporation current for the conducting solution is higher than for the resistive solution, while experiments report a much higher percentage of permeabilized cells in the resistive solution.

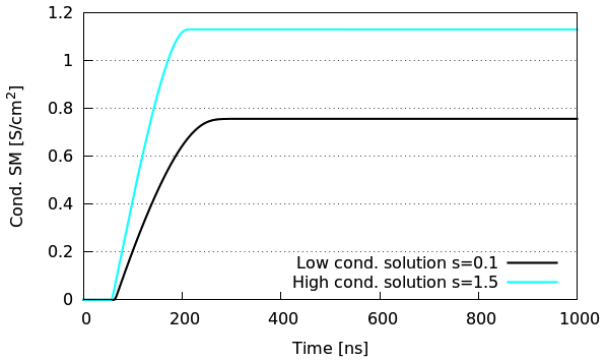

(a) Average membrane conductivity after 1 pulse A

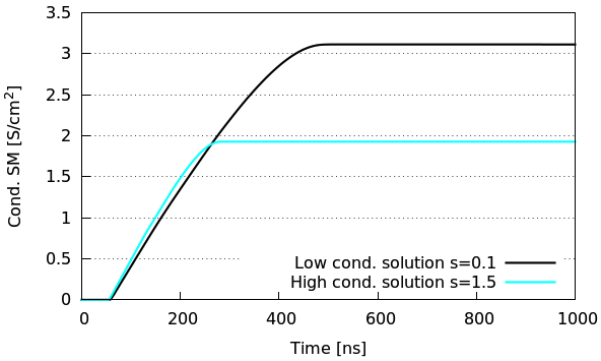

(b) Average membrane conductivity after 1 pulse B

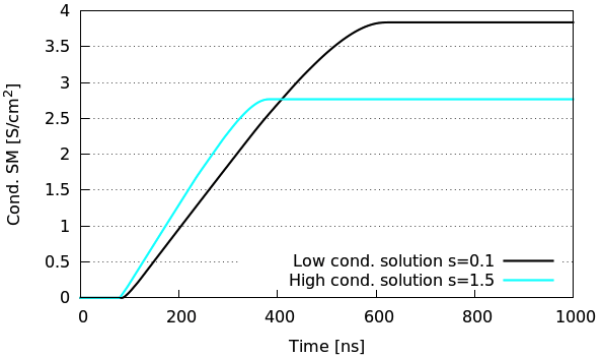

(c) Average membrane conductivity after 1 pulse C

FIGURE 18. Average membrane conductivity S_{m} for both low and high conducting media, for the 3 pulses. Only one pulse is used.

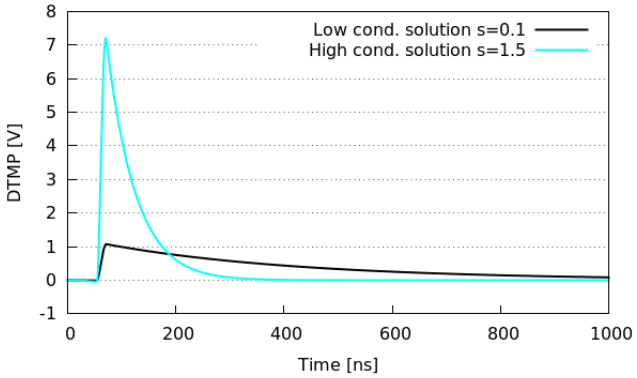

FIGURE 19. Transmembrane voltage in the conducting and the resistive solution for the pulse B.

such that

$$[\mu \partial_{\boldsymbol{n}} u]_\Gamma = 0,$$

where K is a constant which describes the slope of μ at the interface, and $\sigma_c \alpha_c$ and $\sigma_e \alpha_e$ are the electric motility of M in the outer medium and in the cytoplasm far from the interface.

Denoting by d_e and d_c the diffusion coefficients of M in $\mathcal{O}_e$ and $\mathcal{O}_c$ respectively, the concentration M is governed by the following drift–diffusion equation:

$$\begin{aligned} &\partial_t M - d_e \Delta M = \nabla \cdot (\mu M \nabla U), \quad \text{in } \mathcal{O}_e, \\ &\partial_t M - d_c \Delta M = \nabla \cdot (\mu M \nabla U), \quad \text{in } \mathcal{O}_c, \end{aligned} \tag{37a}$$

with the interface conditions on the membrane

$$d_e \partial_{\boldsymbol{n}} M|_{\Gamma^+} + [M]_\Gamma \, (\mu \partial_{\boldsymbol{n}} u)|_{\Gamma^+} = d_c \partial_{\boldsymbol{n}} M|_{\Gamma^+}, \tag{37b}$$

$$P_m(t, V_m) \, [M]_\Gamma = d_e \partial_{\boldsymbol{n}} M|_{\Gamma^+} - (\mu \partial_{\boldsymbol{n}} u M)|_{\Gamma^+}, \tag{37c}$$

$$M|_{t=0} = M_0 \mathbb{1}_{\mathcal{O}_e}, \quad M|_{\partial\Omega} = M_0, \tag{37d}$$

where P_m is the membrane permeability to M, M_0 is the concentration of the bath, and u is the electric potential coming from the electrical model. Equation (37c), that expresses the discontinuity of M across Γ, is a Kedem–Kachalsky type of transmission conditions [55], which describes the filtering effect of the membrane.

4.1.a. *Splitting scheme.* Note that there is no feedback from the transport part towards the electrical part. The discretization of the electric part has been presented in Section 3, and for the volume transport equation (37) we use a classical splitting scheme between the transport and the diffusive parts. Due to the interface, it is important to state carefully the transmission conditions for this splitting. Assuming that M^t is the numerical value of M at the time t, we use the following scheme:

$$\begin{aligned} &M^* = M^t + \delta t \, \nabla \cdot \left(\mu \nabla U^t M^t\right) \quad \text{in } \mathcal{O}_c \cup \mathcal{O}_e, \\ &M^{t+1} - \delta t \, d_e \Delta M^{t+1} = M^*, \quad \text{in } \mathcal{O}_e, \\ &M^{t+1} - \delta t \, d_c \Delta M^{t+1} = M^*, \quad \text{in } \mathcal{O}_c, \end{aligned}$$

with the transmission conditions

$$\begin{aligned} &d_e \partial_{\boldsymbol{n}} M^{t+1}|_{\Gamma^+} - d_c \partial_{\boldsymbol{n}} M^{t+1}|_{\Gamma^-} = (\mu \partial_{\boldsymbol{n}} u)|_{\Gamma^+} \, [M^t]_\Gamma, \\ &P_m(t, V_m^t) \left[M^{t+1}\right]_{\Gamma^+} - d_e \partial_{\boldsymbol{n}} M^{t+1}|_{\Gamma^+} = - (\mu \partial_{\boldsymbol{n}} u)|_{\Gamma^+} \, [M^t]_\Gamma. \end{aligned}$$

The transport equation is solved thanks to the classical upwind scheme, while the diffusion part is solved thanks to a discretization similar to the electric part. In the next subsection we present the model of membrane permeability.

4.2. Membrane permeabilization : a reaction–diffusion model for lipid alteration. The model of membrane permeability is based on the following assumptions, which come from experimental observations:

- We hypothetize that permeabilization results of a long–term effect of defects in the membrane related to an alteration phospholipids due to the presence of water inside the membrane. We thus use membrane voltage $V_{\rm m}$ as an initiating factor of permeabilization. Actually it has been reported by [48, 74] that electric field changes the phospholipid composition, by altering the lipid property.
- The dynamics of alteration and reconstruction of the membrane are dramatically not the same as it has been observed by the experiments [93, 106]. The alteration of the lipids is a physical phenomenon, which occurs as long as pores are present on the membrane and whose characteristic time is in the order of the microsecond. On the contrary, the membrane recovery is a biological phenomenon, called exocytosis, which takes time: it happens for minutes after the electric shock. Thus, we introduce two different time constants: $\widetilde{\tau}_{\rm perm}$ for permeabilization and $\widetilde{\tau}_{\rm res}$ for the membrane recovery due to exocytosis, $\widetilde{\tau}_{\rm res}$ being in the order of one hour as reported by Glogauer *et al.* [45].
- Lipids diffuse along the membrane at a speed $\mathrm{d_L}$ around 1 μm^2/s [20, 114, 109], which is non negligible compared to the lapse of time between two pulses (usually of the order of 1 second), and therefore this surface diffusion has to be accounted for.

We thus use a reaction–diffusion equation on the membrane in order to describe the degree of lipid alteration Y:

$$\partial_t Y - \mathrm{d_L}\Delta_\Gamma Y = F(V_{\rm m}, Y) \text{ on } \Gamma, \tag{38a}$$

with the initial condition

$$Y(t=0,s) = Y^0. \tag{38b}$$

Similarly to the model of membrane conductivity, we set

$$F(V_{\rm m}, Y) = \begin{cases} \dfrac{\widetilde{\beta}(V_{\rm m}) - Y}{\widetilde{\tau}_{\rm perm}}, & \text{if } \widetilde{\beta}(V_{\rm m}) - Y \geq 0, \\ \dfrac{\widetilde{\beta}(V_{\rm m}) - Y}{\widetilde{\tau}_{\rm res}}, & \text{if } \widetilde{\beta}(V_{\rm m}) - Y \leq 0, \end{cases} \tag{39}$$

where $\widetilde{\beta}$ is a regularized Heaviside function, for instance:

$$\widetilde{\beta}(\lambda) := \frac{1 + \tanh(\widetilde{k}(|\lambda| - \mathrm{V_{th}}))}{2}, \quad or \quad \widetilde{\beta}(\lambda) := e^{\left(-(\mathrm{V_{th}}/|\lambda|)^{2\widetilde{k}}\right)}, \tag{40}$$

and where $\mathrm{V_{th}}$ is the voltage threshold above which membrane permeability increases. The membrane permeability is then given by

$$\mathrm{P_m}(t, V_{\rm m}) = X(t, V_{\rm m})\mathrm{P_1} + Y(t, V_{\rm m})\mathrm{P_2}. \tag{41}$$

We also suppose that the permeabilization affects the membrane conductivity, which is then rewritten as

$$S_{\rm m}(t, V_{\rm m}) = \mathrm{S_0} + X(t, V_{\rm m})\mathrm{S_1} + Y(t, V_{\rm m})\mathrm{S_2}, \tag{42}$$

where $\mathrm{P_1}$, $\mathrm{P_2}$ and $\mathrm{S_1}$ and $\mathrm{S_2}$ are such that

$$\mathrm{P_2} \ll \mathrm{P_1}, \quad \mathrm{S_0} \leq \mathrm{S_2} \ll \mathrm{S_1}.$$

This makes it possible to discriminate the short–term porated state, with very high conductivity and permeability, from the long–term permeabilized state whose conductivity and permeability are higher than those of the membrane at rest, but much less than those of the porated state.

4.3. Discretization of the reaction–diffusion model on the interface and coupling with the volume grid. In order to solve equation (38) satisfied by Y onΓ, we use the following numerical scheme:

$$\frac{1}{\delta t} Y^{n+1} - \mathrm{d_L}(\Delta_\Gamma) Y^{n+1} = \frac{1}{\delta t} Y^n + F(Y^n, V_{\rm m}^n). \tag{43}$$

where $(\Delta_\Gamma)Y^{n+1}$ is the Laplace–Beltrami (LBO) Δ_Γ discretized on the interface.

4.3.a. *LBO discretization for parametrized surfaces.* For *in vitro* experiments, cell shapes are roughly speaking spherical, or at least kind of spheroidal. We thus decided to use the formula of the Laplace Beltrami operator Δ_Γ thanks to a parametrization of the surface: let $\Gamma = \Gamma(\theta, \varphi)$ be such a parametrization. The Euclidean metric at any point (θ, φ) is given by

$$\mathcal{G} := \begin{pmatrix} g_{\theta\theta} & g_{\theta\varphi} \\ g_{\theta\varphi} & g_{\varphi\varphi} \end{pmatrix}, \quad g := \det(\mathcal{G}) \quad \text{and } \mathcal{G}^{-1} := \begin{pmatrix} g^{\theta\theta} & g^{\theta\varphi} \\ g^{\theta\varphi} & g^{\varphi\varphi} \end{pmatrix},$$

where

$$g_{\theta\theta} := |\partial_\theta \Gamma(\theta, \varphi)|_2^2, \quad g_{\varphi\varphi} := |\partial_\varphi \Gamma(\theta, \varphi)|_2^2, \quad g_{\theta\varphi} := \langle \partial_\theta \Gamma(\theta, \varphi), \partial_\varphi \Gamma(\theta, \varphi) \rangle.$$

The LBO of any smooth function defined on Γ is then given by

$$\Delta_\Gamma f(\theta, \varphi) = \frac{1}{\sqrt{|g|}} \left[\partial_\theta \left(\sqrt{|g|} \left(g^{\theta\theta} \partial_\theta f + g^{\theta\varphi} \partial_\varphi f \right) \right) + \partial_\varphi \left(\sqrt{|g|} \left(g^{\theta\varphi} \partial_\theta f + g^{\varphi\varphi} \partial_\varphi f \right) \right) \right]. \tag{44}$$

The interface Γ is then discretized by a cartesian grid in (θ, φ) and a centered second order finite differences formula is used to approximate Δ_Γ.

4.3.b. *Coupling the discretizations.* In order to solve the whole model, it is necessary to couple the two discretizations, from the volume mesh to the surface grid and in *vice versa*. Define the **intersection points** as the points at the intersection between the 3D cartesian grid (representing $\mathcal{O}_c \cup \mathcal{O}_e$) and Γ. The points defined by the (θ, φ)–grid involved in the LBO discretization will be called **mesh points**.

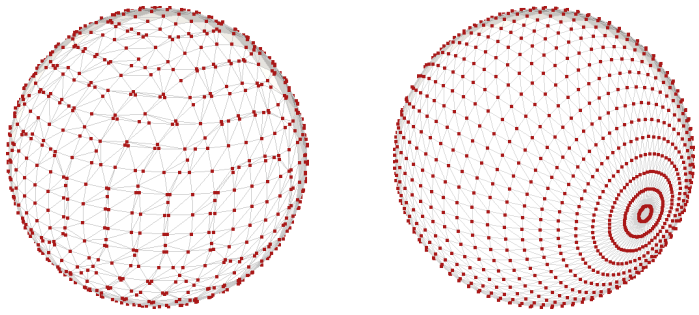

(a) (b)

FIGURE 20. 20(a): Mesh generated from the intersection points with the cartesian grid, used for the resolution of the potential and transport equations. 20(b): (θ, φ)–mesh on which the LBO is discretized.

4.3.c. *From the mesh points to the intersection points.* To obtain the values on the intersection points knowing the function on the mesh points, the coordinates of the intersection points are directly projected on the (θ, φ)–grid. This can be done straightforwardly if the expression of the reciprocal parametrization is known. A regular bilinear interpolation is then possible on this grid: if (θ_j, φ_j) are the coordinates of the point $P_j \in \widetilde{\Gamma}$ in $[\theta_k, \theta_{k+1}] \times [\varphi_l, \varphi_{l+1}]$:

$$\begin{aligned} f(\theta_j, \varphi_j) \quad \sim \quad & f_{kl} + (f_{k+1l} - f_{kl}) \frac{\theta_j - \theta_k}{d\theta} + (f_{kl+1} - f_{kl}) \frac{\varphi_j - \varphi_l}{d\varphi} \\ & + (f_{kl} - f_{k+1l} - f_{kl+1} + f_{k+1l+1}) \frac{(\theta_j - \theta_k)(\varphi_j - \varphi_l)}{d\theta d\varphi} \end{aligned}$$

4.3.d. *From the intersection points to the mesh points.* For the reverse interpolation, we consider the 3D–cartesian cell in which a mesh point is located. In this cell, the interface is described by a convex polygon whose vertices are intersection points where values are known (see Figure 21). We use barycentric coordinates

to perform the interpolation on the mesh point, as given by Meyer *et al.* in [68]. Let P_j, $j = 1, \cdots, j_{\max}$ be the list of these vertices, ordered along j around the mesh point P_{kl}. We define the weights

$$\alpha_j = \frac{\operatorname{cotan}(\overrightarrow{P_jP_{kl}}, \overrightarrow{P_jP_{j-1}}) + \operatorname{cotan}(\overrightarrow{P_jP_{kl}}, \overrightarrow{P_jP_{j+1}})}{\left|\overrightarrow{P_{kl}P_j}\right|_2^2}.$$

The value of a function f at P_{kl} is then given by $\sum_{i=1}^{j_{\max}} \alpha_j f_j$.

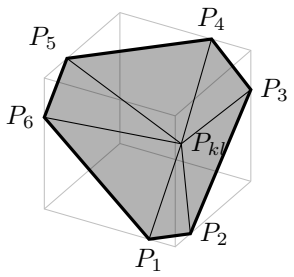

FIGURE 21. Interpolating values known on the intersection points P_j, $j = 1 : 6$ to evaluate a function at the mesh point P_{kl}.

5. Numerical simulations for the complete model in 3D

In this section, we present numerical results for the whole model, which involves both electrical and transport parts. *These results are presented in [62], and are part of the PhD thesis of M. Leguèbe.*

We performed 3D–simulations of a spherical cell submitted to 10 permeabilizing micropulses (10 μs, 40 kV/m), with various repetition rates from 1 to 1 000 Hz. In these simulations, we set the diffusion of the lipids on the membrane to

$$\mathrm{d_L} = 10^{-12}\ \mathrm{m^2 s^{-1}},$$

which is in the range of the measured lateral diffusion of the lipids in cell membranes [38].

It has been very recently reported by A. Silve *et al.* [100] that, strikingly, for the same number of pulses, a high frequency rate of repetition is less efficient than pulses repeated at low frequency. From the modeling point of view, the question of this kind of "desensitization" has never been addressed and we show in this section that our model can provide an explanation to these observations.

The average permeabilization $\mathrm{P_m}$ of the membrane, as well as the concentration of molecules that entered the cell are measured along time. Figure 22 shows the distribution of $\mathrm{P_m}$ on the surface of the cell at different instants of the 1 Hz and 1 000 Hz simulations. A comparative animation of these two simulations is also avalaible as supplementary material. We see that in the case of a fast repetition rate, the altered lipids do not have time to be evenly spread on the membrane. Since the next pulse altesr the same region as the previous one, and therefore the total quantity of altered lipids is lower than for the 1 Hz case.

Figure 23 presents the average of $\mathrm{P_m}$ after each pulse. As expected, the permeabilization is more efficient if enough time is left between pulses to let the lipids diffuse. In Figure 24, we plot the average concentration of molecules in the cytoplasm along time, growing as long as the value $\mathrm{P_m}$ is non–zero. We can see that the 1000 Hz case leads to a lower efficiency of the permeabilization leading to a lower amount of internalized molecules. We emphasize on the fact that the final quantity of molecules is highly dependent on the constants $\widetilde{\tau}_{\mathrm{res}}$ and $\mathrm{P_2}$. If $\mathrm{P_2}$ is large enough (for example for very small molecules), the concentration can reach its maximum value in a very short time whatever the pulse frequency. On the contrary, small values of $\mathrm{P_m}$ increase the difference between the final internalized quantity of molecules. In particular, these simulations corroborate results of High Voltage/Low Voltage experiments [97] that, within the first seconds after the pulses, show a better permeabilization when the lapse of time between two consecutive pulses is longer.

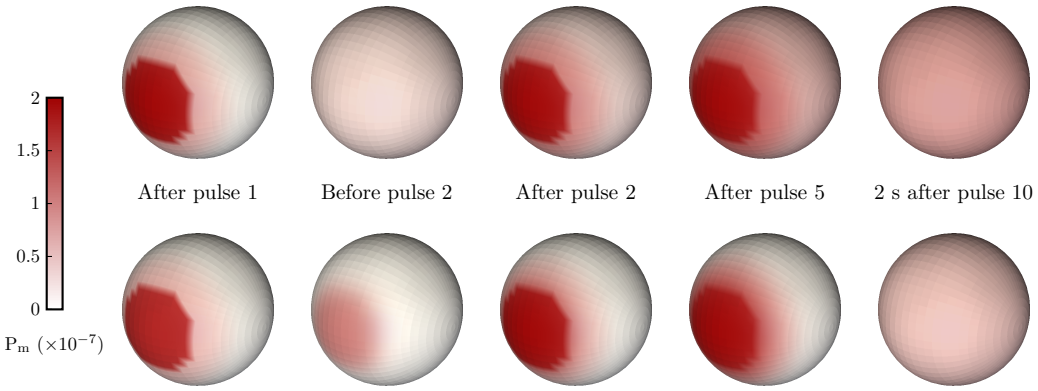

FIGURE 22. Influence of the pulse frequency on the membrane permeabilization P_m. The magnitude of each pulse is 40 kV/m during 10 μs. 10 pulses are applied on both cells, but the time between pulses is different : 1 second for the top line, 1 millisecond for the bottom line. After 10 pulses, the average of P_m is around 8×10^{-8} for the 1 Hz case, and half for the 1 000 Hz case. An animation of these simulation is available as supplementary content.

6. Concluding remarks and perspectives

In this chapter, we have presented some advances in the modeling of cell electropermeabilization. The main insight of our model is to distinguish both conducting and permeable states of membrane, unlike the previous existing models. The main results have been obtained during the PhD study of M. Leguèbe, and can be found in the following papers: [56, 61, 62].

Our model has been studied mathematically, which ensured the stability of the PDE and made it possible the use of efficient numerical schemes. From the modeling point of view, two kinds of validation have been obtained, which correspond to two types of experimental settings. The first validation, which is quantitative, dealt with direct current measurement thanks to patch–clamp technique. This technique made possible to determine plausible parameters of the electrical part of the model. The transport part of the model, which describes the permeable state of the membrane , has been validated qualitatively by the experiments of L.M. Mir's group on cell electropermeabilization and bleomycin.

It is worth noting that the novelty of the model, in particular the use of surface diffusion of altered lipids after the shock made it possible to explain the strange observation of desensitization, that has been reported

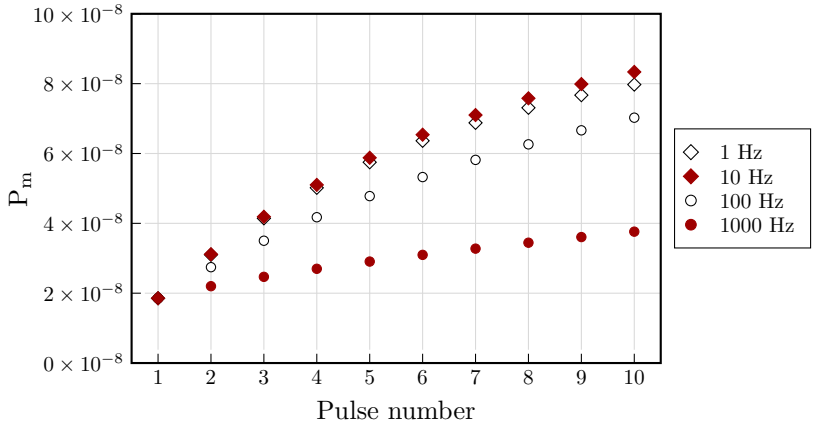

FIGURE 23. Average permeabilization P_m on the cell after each of the 10 pulses of Figure 22 for different pulse repetition rates.

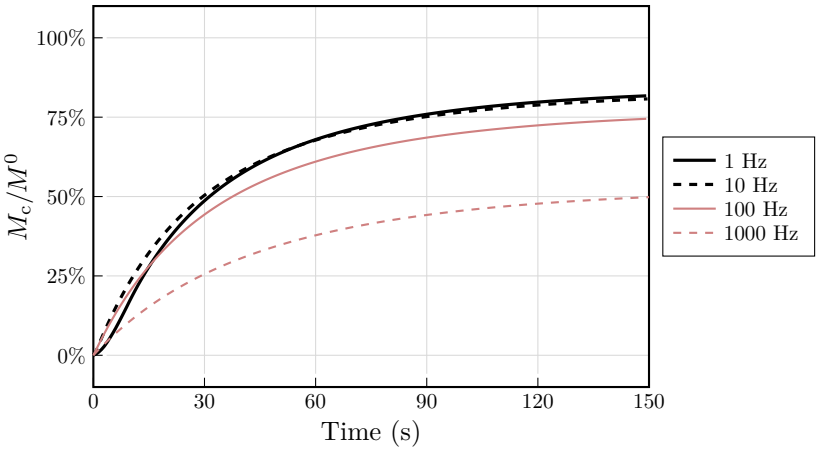

FIGURE 24. Average concentration M_c inside the cell for different pulses repetition rates, expressed as a percentage of external concentration M^0. As in Figure 22 and Figure 23, 10 micropulses (40kV/m during 10μs each) are applied at different frequencies.

very recently by A. Silve *et al.* [100]. This enlightens the crucial advantages to link numerical models and experiments in order to obtain a better description of biological phenomena.

We point out here after some perspectives in electroporation modeling that will be addressed in forthcoming works.

- At the cell scale, it is important to understand how DNA plasmids reaches the nucleus from the cell membrane boundary. Actually, the DNA vaccination is a very active research area in biomedicine, and it holds great promises in cancer treatments. The idea is to identify specific proteins that are produced by cancer cells, and then to generate an auto-immune response by DNA vaccination so that the immune system may detect cancer cells. The DNA uptake in muscle cells is the crucial point of these technique and electroporation seems to be one of the most efficient and save method for this uptake. However the transport of such a big molecule in the cytoplasm is still poorly understood and this problem should be addressed by the applied mathematicians. Note that preliminary works have been obtained by R. Natalini in this way, and the coupling of electroporation model and DNA transport inside the cell will be the heart of forthcoming collaboration with R. Natalini's group.
- Even if we have just presented electroporation at the cell scale, the tissue scale is the most relevant for the applications. It is thus important to investigate the electroporation at this scale. Note that the current models use the electroquasistatic formulation, and consider non-linear conductivity in a similar way as for cells. Roughly speaking, the electric potential is described by the non-linear PDE

$$\nabla \cdot (\sigma(\|\nabla U\|)\nabla U) = F, \quad \text{with } \sigma \text{ given by} \quad \sigma(\lambda) = \sigma_0 + \sigma_1 e^{\left(-(E_{\rm th}/\lambda)^{2k}\right)},$$

  with appropriate boundary conditions. This modeling is still very rough since time-dependence is omitted and the non-linear conductivity which involves the gradient of the potential raises technical questions in the numerical schemes. We also point out the fact that it is not sure that such equation is relevant to describe the time evolution of the electric potential in a tissue submitted to a high voltage pulse. Actually, we emphasize that at the cell scale, the equations of the electroquasistatic potential are very similar to the equations of cardiac cells, from which bidomain equations are derived thanks to two-scale homogenization procedure [29, 4]. It is thus possible that such bidomain equations could provide more relevant results on the study of tissue electroporation. This topic will be adressed in collaboration with Y. Coudière's research-team Carmen, which is devoted to cardiac electrophysiology and numerical computations.

All these points have the same goal: to provide model that can predict quantitatively the degree of tissue permeabilization, and the amount of molecules uptaken by electroporation. The fitting of the parameters

is thus a crucial point, which is common to these perspectives, and which also should be achieved for the models developed in this thesis.

6.1. Publications related to this chapter.

- **Poignard, C.** (2009), *About the transmembrane voltage potential of a biological cell in time-harmonic regime*, ESAIM: Proceedings, 26:16-179.
- Cindea, N., Fabrèges, B., De Gournay, F. & **Poignard, C.** (2010), *Optimal placement of electrodes in an electroporation process*, ESAIM: Proceedings, 30:34-43.
- Duruflé, M., Péron, V. & **Poignard, C.** (2011), *Time-harmonic Maxwell equations in biological cells. The differential form formalism to treat the thin layer*, Confluentes Mathematici, 3(2): 325-357.
- **Poignard, C.**, Silve, A., Campion, F., Mir, L., M., Saut, O. & Schwartz, L. (2011), *Ion flux, transmembrane potential, and osmotic stabilization: A new electrophysiological dynamic model for Eukaryotic cells*, European Biophysics Journal, 40(3): 235-246.
- Kavian, O., Leguèbe, M., **Poignard, C.** & Weynans, L. (on-line 2012), *"Classical" electropermeabilization modeling at the cell scale*, Journal of Mathematical Biology, 68(1-2): 235–265, 2014.
- Perrussel, R. & **Poignard, C.** (2013), *Asymptotic Expansion of Steady-State Potential in a High Contrast Medium with a Thin Resistive Layer*, Applied Mathematics and Computation, 221:48-65.
- **Poignard, C.** & Silve, A. (2014), *Différence de potentiel transmembranaire des cellules biologiques*, Revue 3EI, n^{o}75, Janvier.
- Duruflé, M., Péron, V. & **Poignard, C.** (2014), *Thin layers in electromagnetism*, To appear in CiCP. http://www.dx.doi.org/10.4208/cicp.120813.100114a.
- Leguèbe, M., **Poignard, C.** & Weynans, L., (2013), *"A second Order Cartesian Method for the simulation of electropermeabilization cell models*, Inria Research Report RR-8302, Submitted.
- Leguèbe, M., Silve, A., Mir, L.M, & **Poignard, C.**, (2014) *Conducting and Permeable States Membrane Submitted to High Voltage Pulses. Mathematical and Numerical Studies Validated by the Experiments*, Inria Research Report RR-8496, Accepted in Jnl. Th. Biol.

CHAPTER II

Cell migration modeling

This chapter is devoted to the modeling of cell migration on bioactive micropatterned polymers. This work has been obtained within the framework of a collaboration between the research-team MC2 with M.C. Durrieu from the biological institute IECB of Bordeaux, during the postdoctorate contract of J. Joie, which started in september 2011. The goal is to provide models based on the experimental data in order to describe the cell migration on micropatterned polymers. The long–term goal is to provide tools for the optimization of such a migration, which is crucial in tissue engineering. However we emphasize that the results of this chapter are very preliminary: they deal with the description of the cell migration. We develop two kinds of models: we first consider the cell densities and we use a Patlak-Keller-Segel type model to describe *qualitatively* the cell migration. This model is stated, and rigorously studied in [27] and presented in the next Section 2. We also show numerical results that are in accordance with the experiments. Then, in [54], we provide a simple agent-based model, in which the cells are identified to ellipses with fix minor and major axes. Each cell is characterized by the position of its center and the orientation of its major axis. Using a simple reasoning similar to classical mechanics, we sum up all the forces acting on each cell and the motion is described thanks to a second order differential equation. Even though such a modeling is very naive and simple, we interestingly obtain results that are *quantitatively* in accordance with the experiments, in terms of cell orientation and cell migration. This model is presented in Section 3. We then conclude by forthcoming research we aim at performing in cell migration modeling. Before stating precisely our models, we describe the experimental protocols in the next section.

1. Experimental protocols and observations

Adhesive areas are composed of cell adhesion peptides or growth factor peptides that make the cells adhere. These areas are surrounded by non-adhesive areas. We assume (and this is actually confirmed by experiments) that active principles (cell adhesion peptides or growth factors) do not diffuse. Therefore endothelial cells located outside the adhesive areas cannot straightforwardly "feel" the active principles. They find out the adhesive areas indirectly, probably thanks to chemoattractant produced by cells on the patch. Since cells are *in vitro*, their environment supply them enough nutrients to survive, thanks to grafted active principles onto material. Endothelial cells are seeded onto micropatterned bioactive materials for several hours, then the unadherent cells are removed by rinsing with culture medium. Only the adhered endothelial cells remain on the material. The initial cell density is around 40 000 cells per cm^2. At the beginning of the experiments, during the migration phase, it has been observed that cells have a random motility and stop on adhesive areas. Moreover the attraction of endothelial cells on adhesive areas seems to be higher than the attraction of cells located outside these areas. Experiments show that endothelial cells are grouping together along the micropatterns. On bioactive materials composed of thin strips of tens of micrometers width, that is the order of magnitude of cell size, endothelial cells line their cytoskeleton to adjust themselves with the bioactive micropattern.

To illustrate these experiments, we present in Figure 1 pictures of the micropatterned bioactive materials at the end of the migration phase. Two different micropatterns are considered: on Figure 1(a) thin adhesive areas (bioactive pattern size: 10 μm and distance between patterns: 100 μm) have beed used, whereas Figure 1(b) shows the end of the migration on large strips (bioactive pattern size: 300 μm and distance between patterns: 100 μm). We observed that for the large adhesive areas, the adhered cell density is smaller than for thin strips. Therefore the geometry of the micropatterns seems crucial for the endothelial cell migration.

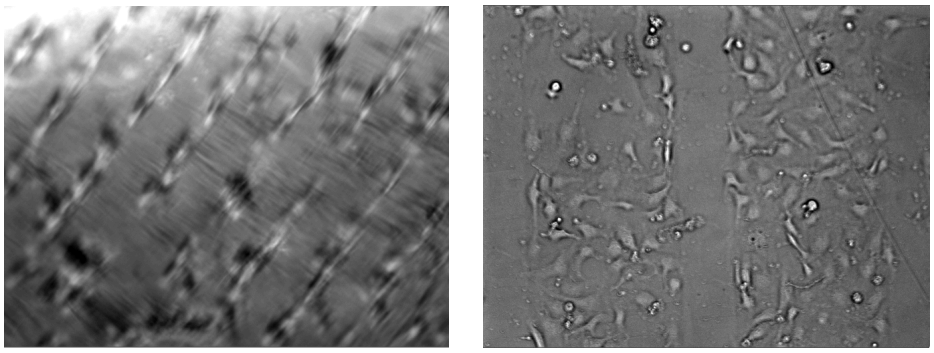

(a) thin areas (b) large areas

FIGURE 1. Endothelial cell alignment onto micropatterned polymer (PET) (10μm (A) and 300 μm (B) stripes of SVVYGLR peptides). The distance between bioactive patterns is 100 μm.

2. Continuous macroscopic model

According to the experiments, the behavior of the cells is drastically different on the adhesive areas and outside these areas. Actually, outside the adhesive strips, the cells seem to attract each other (probably thanks to the chemoattractant they produce) and also diffuse randomly in the domain, but as soon as they reach the adhesive strips the cells seem stuck on the strips and then they diffuse only on the bioactive material, ignoring the outer cells. Moreover, it seems that the cells located on the adhesive strips produce more chemoattractant than the outer cells.

Since there is no clear understanding of the way that endothelial cells communicate, we chose to consider the chemotaxis term as the attraction between endothelial cells (and we do not consider any gradient of concentration of the chemoattractant).

Based on these assumptions, we derive the following model in [27]. Let Ω be a domain bounded domain splitted between adhesive areas, denoted by $\widetilde{\Omega}$, and non-adhesive areas denoted by $\Omega \setminus \widetilde{\Omega}$. We assume that all the domains are bounded domains with smooth boundary.

Two different types of endothelial cells are considered. We denote by $u_1(t,x,y)$ the density of endothelial cells, at any point (x,y) and at time t, that can freely move (**i.e.** they have yet to move over adhesion proteins). Cells that are adhering on the substrate are tracked through their density u_2. The function v represents the density of the chemoattractant. The equations governing the endothelial cell migration are given for $t>0$ by

$$\partial_t u_1 = d_1\Delta u_1 - \lambda \mathbb{1}_{\widetilde{\Omega}} u_1(1-u_2) - \nabla.\left(\chi(u_1,v)u_1\nabla v\right), \qquad \text{in } \Omega, \tag{45a}$$

$$\partial_t u_2 = d_2\Delta u_2 + \lambda \mathbb{1}_{\widetilde{\Omega}} u_1(1-u_2), \qquad \text{in } \widetilde{\Omega}, \tag{45b}$$

$$\partial_t v = \Delta v - \eta v + \gamma_1 u_1 + \gamma_2 u_2, \qquad \text{in } \Omega, \tag{45c}$$

with the homogeneous boundary conditions on $\partial\Omega$ and $\partial\widetilde{\Omega}$:

$$\partial_{\mathbf{n}} u_1|_{\partial\Omega} = 0, \quad \partial_{\mathbf{n}} u_2|_{\partial\widetilde{\Omega}} = 0, \quad \partial_{\mathbf{n}} v|_{\partial\Omega} = 0, \tag{45d}$$

and with the initial conditions $(u_1^0, u_2^0, 0)$:

$$u_1|_{t=0} = u_1^0, \quad u_2|_{t=0} = u_2^0, \quad v|_{t=0} = 0. \tag{45e}$$

We then denote by u the total cell density:

$$u(t,x) = u_1(t,x) + u_2(t,x), \quad t \geq 0,\, x \in \Omega,$$

where u_2 is extended by 0 in $\Omega \setminus \widetilde{\Omega}$.

The parameters d_1, d_2, η, γ_1, γ_2 and λ are strictly positive. The coefficients d_1 and d_2 denote the diffusion coefficients of the cells u_1 and u_2 respectively. The coefficient $\eta > 0$ is the self-degradation rate of the chemoattractant produced by the cells, while the coefficients γ_1 and γ_2 are the coefficients of the production of the chemoattractant respectively for the cell u_1 and u_2. The parameter λ is the speed with which u_1 become u_2, when u_1 lies in the bioactive micropatterns $\widetilde{\Omega}$. The first two equations describe the cell migration in Ω. Outside the bioactive strips, the endothelial cells diffuse and attract the neighboring cells via the chemotaxis sensitivity function :

$$\chi(u_1, v) = \chi^0 \frac{v}{1+|v|}(1-u_1), \quad \text{with}\, \chi^0 > 0.$$

Here above, χ^0 is a chemotaxis parameter, and the term $(1-u_1)$ is settled to prevent the overcrowding of the cells u_1. Endothelial cells once they reach the adhesive area $\widetilde{\Omega}$ are captured and then diffuse only in the strip. This is handled by the penalty term $-\lambda \mathbb{1}_{\widetilde{\Omega}} u_1(1-u_2)$. Cells on the strips still have a random motility and their concentration grows up as the term $\lambda \mathbb{1}_{\widetilde{\Omega}} u_1(1-u_2)$, where $1-u_2$ prevents the blow-up of u_2 in equation (45b). The third equation (45c) describes the production of the chemoattractant by the cells. Since the cells on the strip seem to be more attractive, we suppose that the production coefficients satisfy $0 < \gamma_1 < \gamma_2$. We also add a degradation coefficient $\eta > 0$ describing the metabolization of the chemoattractant.

2.1. Theoretical result. Using the fact the kernels of the operators $\partial_t - \Delta + \eta$ and $\partial_t - d_1\Delta$ in Ω and of the kernel of $\partial_t - d_2\Delta$ in $\widetilde{\Omega}$, with homogeneous Neumann conditions imposed respectively on $\partial\Omega$ and $\partial\widetilde{\Omega}$, are bounded in L^1 and that their respective gradient blows-up as $t^{-3/4}$ in L^1 (see Proposition 1 of [27]), we proved existence and uniqueness for T small enough in $L^\infty(0,T;L^\infty)$ thanks to a fixed point method (Theorem 3.2 of [27]). We then use the mass conservation and uniform bounds to prove global existence. We refer to [27] for the proof of the following results.

THEOREM 2.1 (Theorem 2.1, Proposition 3, Proposition 4 of [27]). *Let d_1, d_2, η, γ_1, γ_2 and λ be strictly positive constants. Suppose that the initial data $(u_1^0, u_2^0) \in L^\infty(\Omega) \times L^\infty(\widetilde{\Omega})$ are such that*

$$\forall x \in \Omega, \quad 0 \le u_1^0(x) \le 1, \quad \forall x \in \widetilde{\Omega}, \quad 0 \le u_2^0(x) \le 1.$$

There exists a unique weak solution (u_1, u_2, v) to problem (45) such that

$$(u_1, u_2, v) \in L^\infty\Big([0,+\infty); L^\infty(\Omega)\Big) \times L^\infty\Big([0,\infty); L^\infty(\widetilde{\Omega})\Big) \times L^\infty\Big([0,\infty); L^\infty(\Omega)\Big),$$

and for almost any $t > 0$

$$0 \le u_1(t,\cdot) \le 1, \quad 0 \le u_2(t,\cdot) \le 1, \quad \textit{and} \quad 0 \le v(t,\cdot) \le \frac{1}{\eta}\left(\gamma_1 + \gamma_2\right).$$

Moreover the mass conservation of the cells is satisfied

$$\int_\Omega u(t,x)\,dx = \int_\Omega (u_1 + \mathbb{1}_{\widetilde{\Omega}} u_2)(t,x)\,dx = \int_\Omega u_1^0\,dx + \int_{\widetilde{\Omega}} u_2^0\,dx, \qquad \forall t > 0.$$

2.2. Numerical results. To solve our model we use a cartesian mesh (composed by quadrilaterals) and a splitting method for the advection–diffusion equation. For the time-discretization, we used Crank-Nicolson method to reach the order 2 in time, and WENO5 scheme is used for the advection part. The method is precisely described in [27], and we present here the conculsion on the cell migration.

2.2.a. *Main highligths of the model.* We investigate the influence of the patterns on cell migration. We fix the total surface of the adhesive domain, and let the number of strips, N_s, vary. The average of u_2 in term of the time for $N_s = 1$, 2, and 4 is presented in Figure 2 . We observe that when considering 4 strips, the migration is quicker. Moreover the mean density reached is higher, which is in accordance with the experimental data.

In spite of the lack of direct attraction of the bioactive patterns, the non-washed out endothelial cells end up on the patterns since the cells adhered on the micropatterns produce more chemoattractants than the cells outside the bioactive materials. We have observed two facts that have been reported by the experiments:

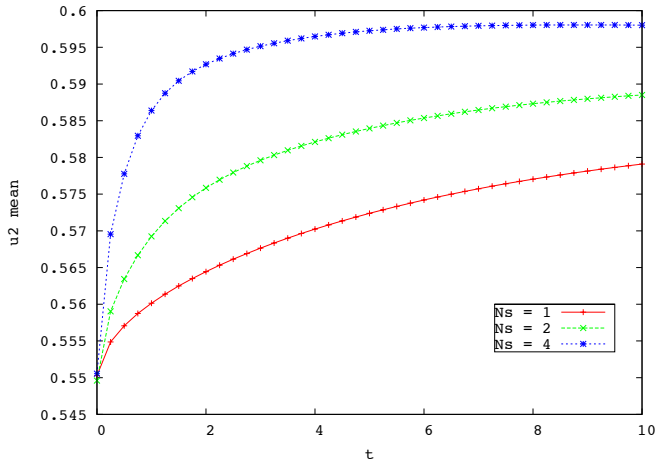

FIGURE 2. The average of the density of cells u_2 attached to patch with respect to the time for different number of strips. The total area of the polymers is fix

(1) For a given surface of bioactive material, the process of cell migration is more efficient with a large number of thin strips than with a small number of large strips.
(2) There exists a minimum value of the initial density of endothelial cells to be imposed in order to have an optimal cell migration towards bioactive patterns. Otherwise the chemoattractant produced by the attached cells is not sufficient to make the cells migrate.

3. Agent-based model for cell migration

The continuous model of the previous section does not take the cell orientation into account, which is an important experimental data since it describes the cell organization on the micropatterns. Cell orientation on the micropatterns plays a crucial role in the formation of tube-like structures, and the aim of this work is to propose a simple model that can account for it.

Since the experiments deal with a quite small number of cells (around 50 000 per cm^2), unlike [26], it is relevant to consider each cell separately and we describe cell-to-cell interactions for a large number of cells. We refer to [33, 110] for agent-based models that describe cell-cel interactions. It is worth noting that the idea is to propose a very simple model that can be fitted to produce quantitative results in accordance with the data, and not to deal with the complex problem of single cell migration: the cells are seen are shape stable body, which moves and rotates along a force vector–field. The following facts have been observed experimentally:

- Initially, cells have a random motility and stop on the adhesive areas.
- The attractive force between cells is important.
- Cells on adhesive areas more strongly pull their neighbors and still have a very low motility.
- Two cells cannot stack themselves.
- If part of a cell body is located on a strip, it tries to completely enter the strip.
- Cells tend to align themselves with their neighbors.

We denote by Ω the domain on which cells migrate. This domain is split into two parts: the micropatterned domain Ω_π, on which cells adhere, and the domain $\Omega \setminus \Omega_\pi$, on which cells move freely. In the experiments, Ω_π is mainly composed of disjoint thin strips of polymers, but some experiments have dealt with annulus micropatterns (see Figure 3(c)). We describe the motion and the orientation of N cells on the domain Ω.

For $0 \leq i \leq N$, the i^{th} cell at the time t is characterized by an ellipse centered at the point $\boldsymbol{M}_i(t)$ of the surface and whose (major axis) orientation is given by the unit vector $\boldsymbol{L}_i(t)$, as described in Figure 3(a).

The major and minor radii of the ellipse, respectively denoted by Λ and λ, do not depend on time: they are parameters of the model that will be fitted with the experimental data.

(a) Ideal cell (b) Micropatterns in strip (c) Micropatterns in circle

FIGURE 3. Schematic single cell, and examples of experimental micropatterned domain.

The heuristics of the modeling can be summarized as follows: using the principle of the second Newton's law, which states that the net force is proportional to the acceleration, we first obtain the motion of $\boldsymbol{M}_i$, the center of the ellipsoidal cell. We then obtain the equation on $\boldsymbol{L}_i$ by analogy with the orientation of a dipole subjected to a field in a bidimensional domain.

3.1. Net force acting on the cell. According to the experiments, and to the biological consideration, a single cell is subjected to the four following forces:

- A long range attractive force between the cells $\boldsymbol{F}_{\mathrm{c}}$, generated by the chemical signal released by the other cells, so that cells attract themselves.
- A short range repulsive force $\boldsymbol{F}_{\mathrm{r}}$, which prevents the overcrowding of the cells.
- A friction force $\boldsymbol{F}_{\mathrm{f}}$, which describes the adhesion to the domain.
- An attractive force on the strip $\boldsymbol{F}_{\mathrm{a}}$, which stacks the cell on the strip thanks to the nutrients.

The differential equation satisfied by the cell center $\boldsymbol{M}_i$ reads:

$$\ddot{\boldsymbol{M}}_i = \boldsymbol{F}_{\mathrm{c}} - \boldsymbol{F}_{\mathrm{r}} - \boldsymbol{F}_{\mathrm{f}} + \boldsymbol{F}_{\mathrm{a}}. \tag{46}$$

Note that we have normalized cell mass to 1 in Newton's law. This is hidden in the parameters describing each force. We chose to keep the inertial term $\ddot{M}_i$ because it is not clear if it can be neglected in the crowding process. The drawbacks of this choice is that small time steps have to be used, which increase the computational time. Of course one can recover the usual overdamped model by choosing carefully the coefficient of the forces which neglect the inertial term. Moreover, as our model involves the velocity of the cells in the description of the forces, it would be difficult to solve numerically the problem without taking the acceleration into account.

Let us write precisely the above forces.

3.1.a. *Cell-to-cell attraction force* $\boldsymbol{F}_{\mathrm{c}}$. The way that endothelial cells communicate is still not clearly understood, but according to biologists (see [63]), it seems that cells produce chemoattractant that diffuse around them in order to attract their neighbors.

We denote by φ the density of chemoattractant produced by the cells on the domain Ω. For each cell, the production of φ is generated by a Gaussian Ψ supported by the cell, whose maximum is at the cell center. We assume that the diffusion of φ occurs on a smaller timescale than the cell movement. Therefore φ satisfies the Poisson equation:

$$\Delta\varphi = f_{\mathrm{c}}(\mathbf{x}) \sum_{i=1}^{N} \Psi\left(\mathbf{x} - \boldsymbol{M}_i(t,\mathbf{x})\right), \quad \forall (t,\mathbf{x}) \in (0,\infty) \times \Omega. \tag{47}$$

with homogenous Dirichlet boundary conditions.

Here above the function f_c is related to the rate of production of the chemoattractant. We assume that cells produce more chemoattractant on the strip than outside, therefore f_c is the following piecewise constant function:

$$f_c(\mathbf{x}) = \begin{cases} 1 & \text{if } \mathbf{x} \in \Omega \setminus \Omega_\pi \\ \gamma_c & \text{if } \mathbf{x} \in \Omega_\pi \end{cases}, \quad \text{with } \gamma_c > 1. \tag{48}$$

This corresponds to the fact that cells that are in good condition of adhesion tends to attract the other cells more than the cell whose adhesion is weak.

The attraction force $\boldsymbol{F}_c$ is then derived from φ:

$$\boldsymbol{F}_c(t, \mathbf{x}) = \nabla\varphi(t, \mathbf{x}), \quad \forall (t, \mathbf{x}) \in (0, +\infty) \times \Omega.$$

From the numerical point of view, φ (and thus the attraction force $\boldsymbol{F}_c$) is computed on the cartesian grid, while the cells move freely in the domain. Therefore, the value of $\boldsymbol{F}_c$ is projected on each endothelial cell $(\boldsymbol{M}_j)_{j=1}^N$, using the projection method described by Min and Gibou [70].

3.1.b. *Repulsive force.* It has been experimentally observed that two cells do not overlap. This fact is taken into account by a repulsive term which prevents the cell overcrowding:

$$\boldsymbol{R}(\boldsymbol{M}_i) = \sum_{\substack{j=1 \\ j \neq i}}^{N} \frac{\boldsymbol{M}_i - \boldsymbol{M}_j}{\|\boldsymbol{M}_i - \boldsymbol{M}_j\|^3}. \tag{49}$$

The power 3 ensures that the repulsive force is an inverse-square law: it is inversely proportional to the square of the distance between 2 cells. We chose such an inverse square law so that repulsion force is bigger than the attraction force. Actually in 2 dimensions the Green function of the Laplacian is $\log(r)$ and therefore the attraction force is of order $1/r$: to prevent the overlapping, we have to impose a repulsion greater than the attraction for short distances.

Since the cells are ellipsoidal, it is necessary to add a multiplication factor in front of $\boldsymbol{R}$. Actually suppose that two cells are located at the points $\boldsymbol{M}_i$ and $\boldsymbol{M}_j$ (see Fig 4). When cells are aligned along $\overrightarrow{\boldsymbol{M}_i\boldsymbol{M}_j}^{\perp}$ (see Figure 4(a)), the repulsion force is the lowest since the distance between the cell boundaries is the greatest. On the contrary, in the configuration of Figure 4(b) the cell alignment is parallel to $\overrightarrow{\boldsymbol{M}_i\boldsymbol{M}_j}$, the repulsion force reach its maximum value. We therefore introduce the factor $\beta(\boldsymbol{L}_i)$, which depends on the orientation

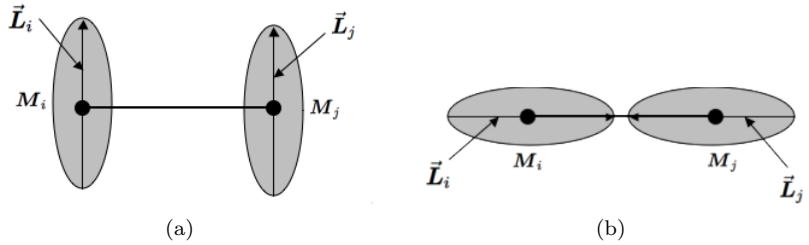

FIGURE 4. Influence of the cell orientation on the cell-cell distance.

of the i^{th} cell:

$$\beta(\boldsymbol{L}_i) = \frac{\Lambda - \lambda}{\lambda} \left(\sum_{\substack{j=1 \\ j \neq i}}^{N} \left(\left| \frac{\boldsymbol{M}_i - \boldsymbol{M}_j}{\|\boldsymbol{M}_i - \boldsymbol{M}_j\|} \cdot \boldsymbol{L}_i \right| + \left| \frac{\boldsymbol{M}_i - \boldsymbol{M}_j}{\|\boldsymbol{M}_i - \boldsymbol{M}_j\|} \cdot \boldsymbol{L}_j \right| \right) \right) + 1. \tag{50}$$

The coefficient $(\Lambda - \lambda)/\lambda$ is introduced in order to take the cell shape into account: for rounded cell it vanishes since there is no cell orientation, and the more elongated the cell, the greater it is. The repulsive force now writes

$$\boldsymbol{F}_r(\boldsymbol{L}_i, \boldsymbol{M}_i) = \gamma_r \beta(\boldsymbol{L}_i) \boldsymbol{R}(\boldsymbol{M}_i), \tag{51}$$

where γ_r is a parameter fitted with the experiments.

3.1.c. *Friction force.* The friction force is proportional to the cell velocity, it thus reads

$$\boldsymbol{F}_{\rm f}(\boldsymbol{M}_i) = \alpha_{\rm f} f_{\rm f}(\boldsymbol{M}_i)\dot{\boldsymbol{M}}_i,$$

where the friction coefficient $f_{\rm f}$ describes the adherence of the domain. Since cells move slowly on the strip, $f_{\rm f}(\boldsymbol{M}_i)$ is a piecewise constant function given by :

$$f_{\rm f}(\boldsymbol{M}_i) = \begin{cases} 1 & \text{if } \boldsymbol{M}_i, \in \Omega \setminus \Omega_\pi \\ \gamma_{\rm f} & \text{if } \boldsymbol{M}_i, \in \Omega_\pi \end{cases}, \quad \text{with } \gamma_{\rm f} > 1. \tag{52}$$

3.1.d. *Attractive force of the adhesive areas.* If a part of a cell is located on the micropatterned polymer region, it will find nutrients and oxygens on the active principle that will attract the whole cell on the strip. On the contrary, if the cell is completely on the polymer region, or outside this region, the attraction force $\boldsymbol{F}_{\rm a}$ due to the strip vanishes.

We use the above function $f_{\rm f}$, which describes the adherence of the domain, to determine whether the cell is straddling the polymer region and the outer domain. Actually, since the distance between two strips is larger than the cell size, the term

$$f_{\rm f}(\boldsymbol{M}_i + \Lambda \boldsymbol{L}_i) - f_{\rm f}(\boldsymbol{M}_i - \Lambda \boldsymbol{L}_i),$$

vanishes if the point $\boldsymbol{M}_i + \Lambda \boldsymbol{L}_i$ and $\boldsymbol{M}_i - \Lambda \boldsymbol{L}_i$ are on the same domain. It is positive and equal to $\gamma_{\rm f} - 1$ if $\boldsymbol{M}_i + \Lambda \boldsymbol{L}_i$ is on the strip and not $\boldsymbol{M}_i - \Lambda \boldsymbol{L}_i$, and thus the cell will tend to move in the direction of $\boldsymbol{L}_i$. On the other hand, if $\boldsymbol{M}_i - \Lambda \boldsymbol{L}_i$ is on the strip and not $\boldsymbol{M}_i + \Lambda \boldsymbol{L}_i$, then it equals $1 - \gamma_{\rm f}$, and the cell will tend to move in the direction of $-\boldsymbol{L}_i$. Similar considerations by replacing Λ by λ and $\boldsymbol{L}_i$ by $\boldsymbol{L}_i^\perp$ ensures that $\boldsymbol{F}_{\rm a}$ is thus given by

$$\begin{aligned} \boldsymbol{F}_{\rm a}(\boldsymbol{M}_i, \boldsymbol{L}_i) = {} & \gamma_{\rm a} \left(f_{\rm f}(\boldsymbol{M}_i + \Lambda \boldsymbol{L}_i) - f_{\rm f}(\boldsymbol{M}_i - \Lambda \boldsymbol{L}_i) \right) \boldsymbol{L}_i \\ & + \gamma_{\rm a} \left(f_{\rm f}(\boldsymbol{M}_i + \lambda \boldsymbol{L}_i^\perp) - f_{\rm f}(\boldsymbol{M}_i - \lambda \boldsymbol{L}_i^\perp) \right) \boldsymbol{L}_i^\perp, \end{aligned} \tag{53}$$

where $\gamma_{\rm a}$ is a numerical parameter.

3.2. Orientation of the cells. As mentioned before, the deformation of endothelial cells is a very complex process, which is not taken into account in our simple model. Nevertheless, the cell alignment plays an important role in the tube-like formation. We therefore have chosen to take this alignment behavior into account by modeling the orientation $\boldsymbol{L}_i$ of each cell.

3.2.a. *Heuristics of cell alignment.* Before stating the equation satisfied by $\boldsymbol{L}_i$, we introduce the "alignment" vector field $\boldsymbol{\Phi}$ defined from $\mathbb{R}^2 \times \mathbb{R}^2$ onto $\mathbb{R}^2$ by

$$\begin{aligned} \boldsymbol{\Phi} : \quad & \mathbb{R}^2 \times \mathbb{R}^2 \to \mathbb{R}^2 \\ & (\mathbf{U}, \mathbf{V}) \mapsto (\mathbf{U} \cdot \mathbf{V})(\mathbf{U} \cdot \mathbf{V}^\perp)\mathbf{U}^\perp \end{aligned} \tag{54}$$

In order to understand the above vector field $\boldsymbol{\Phi}$, suppose that $\mathbf{V}$ is a given vector of $\mathbb{R}^2$. Let $\mathbf{U}$ be a time-dependent vector of $\mathbb{R}^2$ and let θ be the angle between $\mathbf{U}$ and $\mathbf{V}$ in the left-handed orientation. The orientation of $\mathbf{U}$ along $\mathbf{V}$ is easily written by the following ordinary differential equation on θ:

$$\dot{\theta} = -\frac{1}{2}\sin(2\theta),$$

such that $\{0, \pi\}$ are stable equilibrium points while $\{-\pi/2, \pi/2\}$ are unstable. This differential equation can be written in terms of $\mathbf{U}$ thanks to $\boldsymbol{\Phi}$:

$$\dot{\mathbf{U}} = \boldsymbol{\Phi}(\mathbf{U}, \mathbf{V}).$$

3.2.b. *Differential equation for $\boldsymbol{L}_i$.* According to the experiments, the cell orientation is driven by three phenomena:

- Alignment along the cell velocity.
- Alignment along the orientation of their neighbors.
- Alignment along the local tangent vector $\mathbf{S}_i$ of the boundary of micropatterns at the closest point of $\boldsymbol{M}_i$.

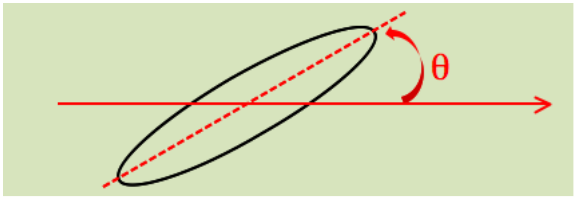

FIGURE 5. Definition of the angle θ for a cell.

We therefore infer the differential equation for $\boldsymbol{L}_i$:

$$\begin{aligned}\dot{\boldsymbol{L}}_i = \omega_{\mathrm{v}}\boldsymbol{\Phi}(\boldsymbol{L}_i, \frac{\dot{\boldsymbol{M}}_i}{\|\dot{\boldsymbol{M}}_i\|}) + \omega_{\mathrm{c}}\sum_{\substack{j=1\\ j\neq i}}^{N}\frac{\boldsymbol{\Phi}(\boldsymbol{L}_i,\boldsymbol{L}_j)}{\|\boldsymbol{M}_i-\boldsymbol{M}_j\|^2}\lambda^2 \\ + \omega_\pi\beta_\pi(\boldsymbol{M}_i)\boldsymbol{\Phi}(\boldsymbol{L}_i,\mathbf{S}_i).\end{aligned} \tag{55}$$

Here again it is natural to introduce an inverse-square law for the interaction between two cells. The above function β_π is given by

$$\begin{aligned}\beta_\pi(\boldsymbol{M}_i) = 4f_{\mathrm{f}}(\boldsymbol{M}_i) - f_{\mathrm{f}}(\boldsymbol{M}_i+\Lambda\boldsymbol{L}_i) - f_{\mathrm{f}}(\boldsymbol{M}_i-\Lambda\boldsymbol{L}_i) \\ - f_{\mathrm{f}}(\boldsymbol{M}_i+\lambda\boldsymbol{L}_i) - f_{\mathrm{f}}(\boldsymbol{M}_i-\lambda\boldsymbol{L}_i),\end{aligned} \tag{56}$$

it ensures that if the cell is entirely on (or out of) the micropatterns, the cell does not try to align but if the cell is partly on the strip then it tends to align along the direction of the strip. Here above, the parameters ω_{v}, ω_{c} and ω_π are homogeneous to the inverse of the characteristic time of each alignment. They will be fitted with the experiments.

3.3. Simulations and experiments. In order to study the consistency of our model, we compare the simulation with the experimental results. We focus on experimental results described in [64]. The domain Ω is a square of $1\mathrm{mm}^2$, on which 500 cells are randomly distributed, in accordance with the experiments. To compute the distribution of the chemoattractant φ given by (47), the domain Ω is meshed thanks to a cartesian grid of 100×100 elements. Three different widths of the adhesive areas are considered: 10, 50 and 100 μm, with the same spacing of 100 μm between the strips.

We emphasize that in order to validate the model we first optimized the parameters for one specific experiment: here we present the case of strips of 100μm width, and then, taking the values of the parameters for this specific experiment and changing the geometry, we compare the numerical results to the experimental data.

3.4. Quantitative results on cell alignment. We now focus on the orientation of the cells in the three previous configurations. In [64], at the end of the experiment, the authors measure the angle θ (in degree) between the major axis of a cell with the axis of the adhesive areas as shown in the Figure 5. For each configuration, six experiments are performed and histograms of the mean values are obtained. This is consistent with the number of experiments performed for each configurations ([63]). When θ is less than $10°$, we have considered that the cells are aligned with the strip.

We first consider the 100 μm width strips case. We have computed the angle θ of the adhered cells for different initial conditions. We present experimental and numerical results in Figure 6. The results are qualitatively and quantitatively in accordance with the experiments. Experimentally, 27% of the cells are considered to be aligned, numerically, this value is equal to 33.78%. Moreover, the mean value of the cell body alignment angle is equal to 25.9 in [64] and we obtain a closed value: 23.10. (see also Tables 1–2).

For the domain composed by 10μm width strips, the results are also in accordance with the experiments, as shown in Figure 7.

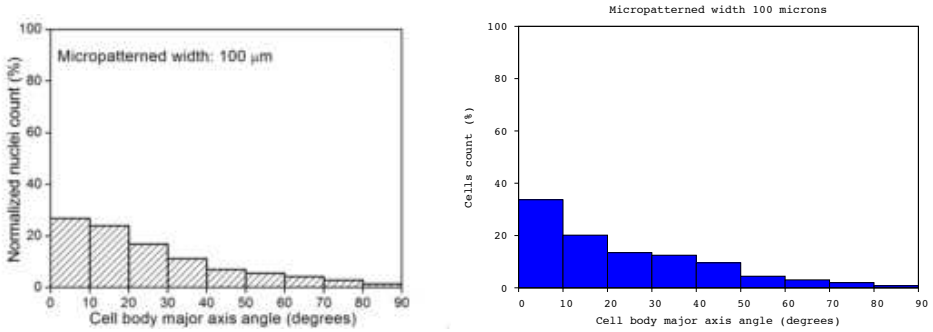

(a) 100 μm experiments, [64] (b) 100 μm simulations

FIGURE 6. Cell alignment on 100μm strips, comparison between experimental (a) and numerical (b) results.

Note that the number of aligned cells is more important on thin strips. Numerically, 70.54 % of the cells have an angle belonging between 0° and 10° whereas experimentally one obtains 73 % of the cells. The mean alignment angle value obtained numerically is equal to 8.8° and experimentally it is equal to 9.98°.

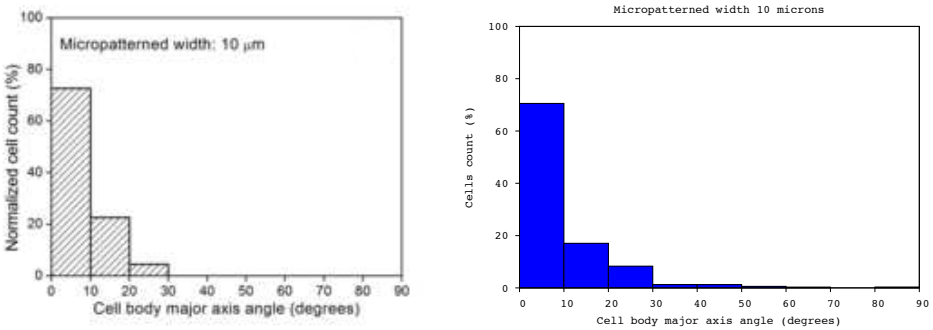

(a) 10 μm experiments, [64] (b) 10 μm simulations

FIGURE 7. Cell alignment on 10 μm strips in the experiments Figure 7(a) and in the simulation Figure 7(b).

Let us now take 50 μm width strips. As previously, we show, in Figure 8, the cell alignment at the end of the experiment.

The distribution of the angle have qualitatively the expected behavior, the cells are more aligned than in the case of 10 μm strips. One observes that 42% of the cells are aligned, when we have obtained 47.19%. We obtain an angle mean value of 14.62°, which is very closed to the experimental measurements: 15.2°. The comparison between the experimental measurement of the cell orientation to the simulation are summarized in tables 1–2. As mentioned above, the numerical results are qualitatively in good agreement with the experimental data.

According to both experimental and numerical results (Figure 7, Figure 8 and Figure 6) the cell alignment is more efficient on thin strips than on larger ones.

Moreover, the forces that we have used are enough to describe both adhesion and orientation of the cells. This may be seen, in some sense, as a basic framework for the description of cell motion on scaffold.

4. Conclusion and perspectives on cell migration modeling

In this chapter, we have presented two models to describe cell migration on bioactive micropatterned polymers. We first derived a continuous model of Patlak-Keller-Segel type in which we discriminate the

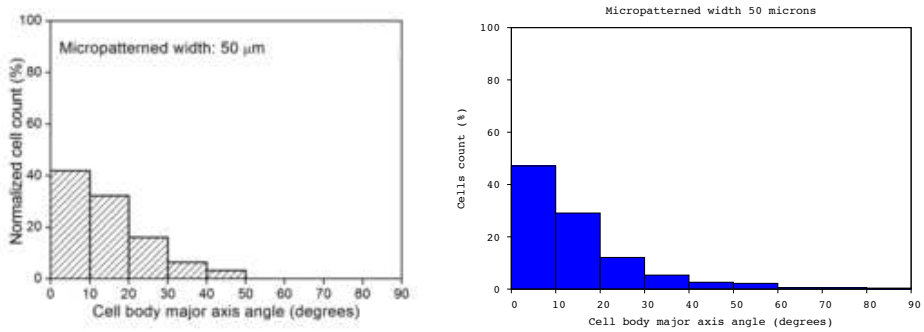

(a) 50 μm experiments, [64] (b) 50 μm simulations

FIGURE 8. Cell alignment on 50μm strips, comparison between experimental (a) and numerical (b) results.

	Percentage of aligned cells along the strips		
	10 μm	50 μm	100 μm
Exp. Data	73	42	27
Num. Res.	70.54	47.1	33.68

TABLE 1. Angle of the mean cell alignment along the patch

	Angle of the mean alignment along the strips		
	10 μm	50 μm	100 μm
Exp. Data	8.6± 6.1°	15.2±9.6°	25.9±15.8°
Num. Res.	9.98°	14.62°	23.10°

TABLE 2. Cell alignment of the experiments (Exp. Data.) given by [64] compared with the numerical simulations (Num. Res.)

non adhered cells from the adhered cells thanks to a penalization term, which makes the cell pass from the free moving state to the stuck state. We studied theoretically and numerically this model, which provides results that are qualitatively in accordance with the experimental data. We then develop a simple (and simplistic) agent-based model in which cells are shape stable bodies moving in a force vector–field, similarly to classical mechanics. Quite strikingly, we found parameters that made possible to obtain quantitative results in accordance with the data on the cell orientation.

4.1. Publications about cell migration.

- Colin, T.; Durrieu, M.-C.; Joie, J.; Lei, Y.; Mammeri, Y.; **Poignard, C.** & Saut, O. (2013), *Modelling of the migration of endothelial cells on bioactive micropatterned polymers*, Math. BioSci. Eng., 10(4):997-1015.
- Joie, J.; Y. Lei; Colin, T.; Durrieu, M.-C.; **Poignard, C.** & Saut, O. (2013), *Modeling of migration and orientation of endothelial cells on micropatterned polymers*, Inria-RR 8252, Submitted.

4.2. Perspectives. The next step of this research should be an accurate fitting of these models with the experiments, however due to scientific opportunity, I am switching to a quite different problem of cell migration: the modeling of the invadopodia, through a collaboration with Osaka University and Tokyo University of Science. I present briefly the topic as conclusion of this chapter.

Invadopodia describes the ability of the cancer cell to destroy the extra-cellular matrix (ECM) in order to migrate out of its environment. Cell produces MMP enzymes, which destroy the ECM: the ligands, as soon as they touch the cell membrane, generate a signal in the cell which lead to the formation of invasive feet, see Figure 1).

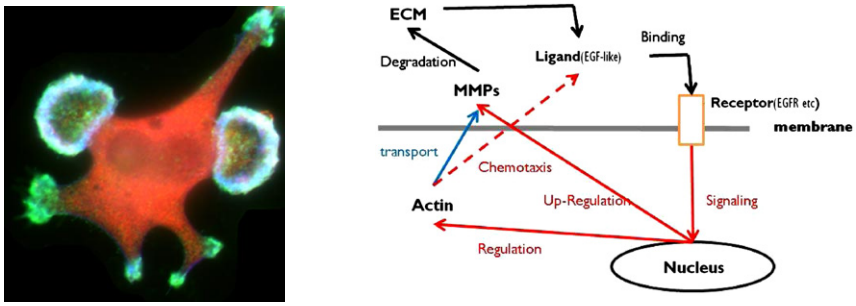

(a) Protusion formation in the invadopodia process

(b) Cascade of the chemical reactions

FIGURE 9. Principles of invadopodia

The research program about this subject can be split into two–fold:

- I am currently studying the mathematical analysis of the model will be developed by T. Colin, M. Ohta, and T. Suzuki. Existence and uniqueness results for this type of model are not trivial due to the moving boundary of the domain in which the PDEs are written.
- In parallel, it is necessary to develop appropriate schemes to compute numerically the model. Here again the motion of the boundary creates a non trivial difficulty. I am supervising the PhD thesis of O. Gallinato, co-advised by T. Colin and T. Suzuki, to provide accurate schemes that make possible the computation of the model.

I briefly present the simple model, we are considering and how we aim at tackling its well-posedness. Denote

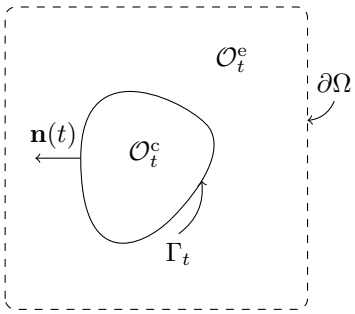

FIGURE 10. Geometry of the problem. The cell $\mathcal{O}_t^{\mathrm{c}}$ is imbedded in the bath $\mathcal{O}_t^{\mathrm{e}}$. The whole domain Ω does not depend on the time variable. It is defined by $\Omega = \mathcal{O}_t^{\mathrm{e}} \cup \overline{\mathcal{O}_t^{\mathrm{c}}}$.

by Γ_0 the unit circle. Let g be a function smooth enough, and defined on $\mathbb{R}^+ \times \mathbb{R}^2$. We aim at studying the well-posedness of the following free boundary problem:

$$\Delta c^\star = 0, \quad x \in \mathcal{O}_t^{\mathrm{e}}, \tag{57a}$$

$$c^\star(t,\cdot)|_{\partial\Omega} = 0, \quad -\partial_{\mathbf{n}} c^\star|_{\Gamma_t} = g(t,\cdot), \tag{57b}$$

$$\Delta\sigma(t,x) = 0, \quad t \in [0,T], \ \ x \in \mathcal{O}_t^{\mathrm{c}}, \tag{57c}$$

$$\sigma(t,x) = c^\star(t,x), \quad t \in [0,T], \ \ x \in \Gamma_t, \tag{57d}$$

$$(\partial_t + \nabla\sigma \cdot \nabla)\psi = 0, \quad t \in [0,T], \ \ x \in \Gamma_t, \tag{57e}$$

where

$$\mathcal{O}_t^{\mathrm{c}} = \{x \in \mathbb{R}^2 : \psi(t,x) > 0\},$$
$$\mathcal{O}_t^{\mathrm{e}} = \{x \in \mathbb{R}^2 : \psi(t,x) < 0\},$$
$$\Gamma_t = \{x \in \mathbb{R}^2 : \psi(t,x) = 0\}, \qquad \mathbf{n} = -\frac{\nabla\psi}{|\nabla\psi|}.$$

This model is the simplest model that describes the cell migration process. Actually, for a given distribution of MMP enzymes, ligands $c^\star$ are created on the boundary of the membrane. This ligand generates a signal σ, which diffuses inside the cell, and the membrane motion is driven by the velocity, which is given by the gradient of the signal. More precise models, that involve the production of MMP enzymes and other complex biological phenomena are not addressed in this preliminary work. We focus on the well-posedness of problem (57), in a bidimensional framework. We are confident that the well-posedness for a more accurate description of the cell migration will be a consequence of these results. We aim at presenting the main ideas to tackle such a free-boundary value problem for cell migration.

Following the paper of Iguchi [51], we assume that the free boundary Γ_t is in a neighborhood of the unit circle for $t \in [0,T]$, and we transform the problem (57) using the Lagrangian coordinates. More precisely, let X_1, X_2 be real-valued functions such as

$$\zeta(t,\theta) := (1 + X_2(t,\theta))e^{i(\theta + X_1(t,\theta))}, \quad \theta \in \mathbb{T} := \mathbb{R}/2\pi\mathbb{Z}, \tag{58}$$

be the parameter-representation of the free boundary Γ_t. The motion of $\Gamma(t)$ is then given by

$$\partial_t \zeta(t,\theta) = \nabla\sigma(t,\zeta(t,\theta)). \tag{59}$$

The well-posedness of Problem (57) is equivalent to prove existence and uniqueness of the above functions (X_1, X_2). Defining $\mathcal{T}$ as the vector-functions of 4 coordinates defined by

$$\begin{aligned}\mathcal{T}(\mathbf{U},\mathbf{V}) &= \begin{pmatrix}\mathcal{T}_1(\mathbf{U},\mathbf{V})\\ \mathcal{T}_2(\mathbf{U},\mathbf{V})\end{pmatrix}, \qquad \forall\,(\mathbf{U},\mathbf{V}) = (U_1,U_2,V_1,V_2),\\ &= \begin{pmatrix}V_2\cos(\theta+U_1) - (1+U_2)(1+V_1)\sin(\theta+U_1)\\ V_2\sin(\theta+U_1) + (1+U_2)(1+V_1)\cos(\theta+U_1)\end{pmatrix},\end{aligned} \tag{60}$$

then the vector function $\mathbf{X} = (X_1, X_2)$, which defines the parameterization of Γ_t, satisfies the following problem:

$$\partial_t X_2 \partial_\theta X_2 + (1+X_2)^2 \partial_t X_1 (1 + \partial_\theta X_1) = \mathcal{T}(\mathbf{X}, \partial_\theta \mathbf{X}) \cdot \nabla c^\star(t, \zeta(t,\theta)). \tag{61a}$$

$$\partial_t X_2 = \mathbb{K}\left[(1+X_2)\partial_t X_1\right], \tag{61b}$$

where $\mathbb{K}$ is the non-local operator of order 0 defined as in Iguchi [51]. Using a quasilinearization in the same vein as Iguchi [51], we are confident that one can prove well-posedness of Problem (61), under the following hypothesis.

Hypothesis 4.1 (Sign condition for the well-posedness). *We assume that $g_0 = g(0,\cdot)$ is such that there exists $\alpha > 0$, such that*

$$\mathbb{K}_0\left[\partial_\theta \Lambda_0 g_0\right] + g_0 \geq \alpha > 0,$$

where Λ_0 is the Neumann–to–Dirichlet operator defined for any $f \in H^{-1/2}(\Gamma_0)$ by $\Lambda(f) = u|_{\Gamma_0}$ where u is the solution in $\mathcal{O}_0^{\mathrm{e}}$ to

$$\Delta u = 0, \text{ in } \mathcal{O}_0^{\mathrm{e}} \qquad\qquad u|_{\partial\Omega} = 0, \qquad -\partial_{\mathbf{n}_0} u|_{\Gamma_0} = f.$$

Using a Ghost-Fluid method for the homogeneous Neumann condition, and a WENO5 scheme to capture the level–set, we obtain preliminary results that are quite encourageous, see Figure 11.

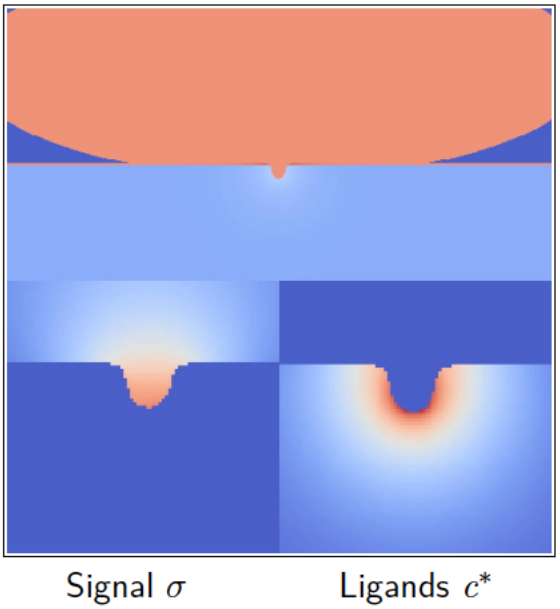

FIGURE 11. Preliminary numerical results on our simple model of invadopodia. In the upper part, we see formation of the protusion. The lower pictures present on the left the signal distribution in the cell and on the right, the the degraded ECM (the ligand) outside the cell.

CHAPTER III

Tumor Growth Models

This chapter is devoted to tumor growth models based on partial differential equations. I started this activity in september 2013 with the begining of the PhD thesis of O. Gallinato [1], and therefore this chapter is only based on one submitted preprint: [28]. Taking advantages of the knowledge of the research team MC2, which has started the modeling of tumor growth before my recruitment, together with T. Colin, O. Saut and O. Gallinato we derived in [28] a model for breast cancer (ductal carcinoma).

On-going works that yield the PhD research of T. Michel, whom I co-advise with T. Colin on the mathematical properties of a generic tumor growth model on one side, and those of F. Cornelis[2] and G. Lefèbvre on the modeling of GIST liver metastases resistance to drugs are presented in conclusion.

1. Tumor growth model for ductal carcinoma

Ductal carcinomas are among the most common breast cancers. Originally located to the milk duct, these cancers may become invasive and agressive after the degradation of the duct membrane. In this section, we present the tumor growth model we derived in [28], which is specific to two types of ductal carcinomas: the ductal carcinoma **in situ** (DCIS), which remains confined to the milk duct and the invasive ductal carcinoma (IDC), which produces specific enzymes called MMPs that degrade the duct membrane.

Our tumor growth model of ductal carcinoma describes different cell densities thanks to a system of PDEs similar to [92, 14, 15]. Roughly speaking, the tumor growth is driven by an advection equation which takes into account the fact that cancer cell proliferation generates a pressure that pushes the healthy tissue. We assume that the total cell density is constant in the whole tissue, equal to đ_0 and we distinguish between 4 types of cells: the healthy cells, whose proportion is denoted by S, the proliferating cells described by P, the necrotic cells tracked by N and the lumen cells, that remains confined to the duct membrane and whose percentage is given by L. The condition that there is no other cell type is given by

$$P + N + S + L = 1. \tag{62}$$

The main feature of our model, which is given in subsection 1.1, lies in the modeling of the duct membrane, which separates the lumen of the duct from the breast tissue and which is degraded by the MMPs. Actually we used a Kedem–Katchalsky type condition to handle the jump of pressure across the duct membrane, which is thin compared to the characteristic size of the breast. The new insights, compared to other existing tumor growth models, can be classified into two types:

- Specific aspects of the model as a model for breast cancer:
  - the mechanics related to the duct are taken into account,
  - the vascularization is located outside the duct, therefore the growth phase **in situ** is an avascular phase,
  - the nutrients diffusion is artificially forced within the duct, which avoids introducing a nonlinear diffusion to obtain realistic rates of nutrients.
- Non-specific aspects:
  - the pressure is taken into account in the proliferation rate, as some studies show that it tends to limit cancer cell proliferation [41, 121],
  - the very low thickness of the basement membrane led us to model it as an interface with jump conditions to link the outer and inner media thanks to Kedem-Katchalsky type conditions.

[1] O. Gallinato is a PhD student co-advised by T. Colin, T. Suzuki from Osaka University and myself.

[2] F. Cornelis is MD – radiologist – at CHU Bordeaux. He is doing a PhD with T. Colin and O. Saut on the modeling of tumor growth from medical imaging. G. Lefebvre is advised by T. Colin.

Since our deterministic PDE system provides too homogeneous solution compared to the biological data, we investigate different plausible hypotheses in the modeling that could explain such a heterogeneity:

- introduction of a mutation on certain cancer cells, which causes the MMP production, resulting in an anisotropic tumor invasion,
- modeling the role of cells of the microenvironment that produce MMPs or TNFs (tumor necrosis factors), with satisfactory results in terms of tumor heterogeneity.

In particular, the consideration of the microenvironment influence on the MMP production leads to one of the most significant result of the study, given by Figure 1: numerical results (Figure 1(a)) show the invasion of the breast tissue due to the membrane disruption, and are qualitatively similar to biopsies (Figure 1(b)).

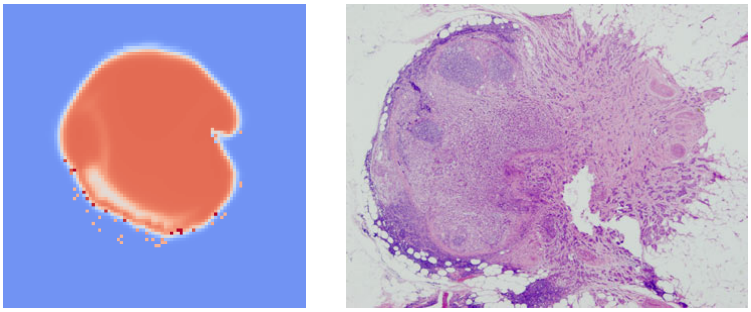

(a) IDC simulation (b) Biopsy image from [75]

FIGURE 1. Main result : qualitative comparison of our simulation with biopsy.

1.1. Construction of the ductal carcinoma growth model. The structure of the model is outlined in the schema of Figure 2. For the sake of clarity, we subdivide our model into three submodels given by Figure 3.

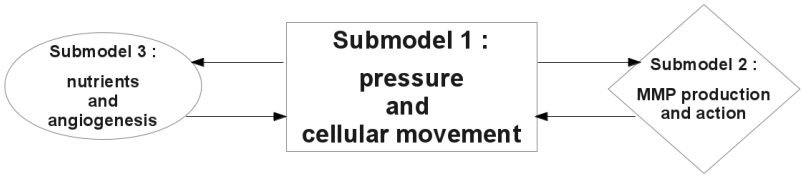

FIGURE 2. Schematic diagram of the model structure.

Submodel 1 is at the heart of the model: it describes the general movement of cell species caused by the pressure due to cell proliferation. The specificity lies in the modeling of the very thin membrane as an interface across which Kedem-Katchalsky type conditions are imposed to describe the jump of pressure. Submodel 2, given at Subsubsection 1.1.b, describes the action of MMP enzymes, leading to cell invasion, which is crucial in this study. Finally, submodel 3, dealing with nutrients, will be discussed in Subsubsection 1.1.c. It considers that the supply of nutrients comes from the membrane vasculature and from the neo-vasculature resulting from the angiogenesis.

1.1.a. *Submodel 1: Advection equations and generic structure of the model.* We denote by Ω the considered domain composed of the duct (Ω_0), the membrane (Γ) and the outer medium (Ω_1).

$$\partial_t P + \nabla \cdot (\mathbf{v}P) = (\alpha_P - \alpha_N)P, \tag{63a}$$

$$\partial_t N + \nabla \cdot (\mathbf{v}N) = \alpha_N P, \tag{63b}$$

$$\partial_t S + \nabla \cdot (\mathbf{v}S) = 0, \tag{63c}$$

$$\partial_t L + \nabla \cdot (\mathbf{v}L) = 0, \tag{63d}$$

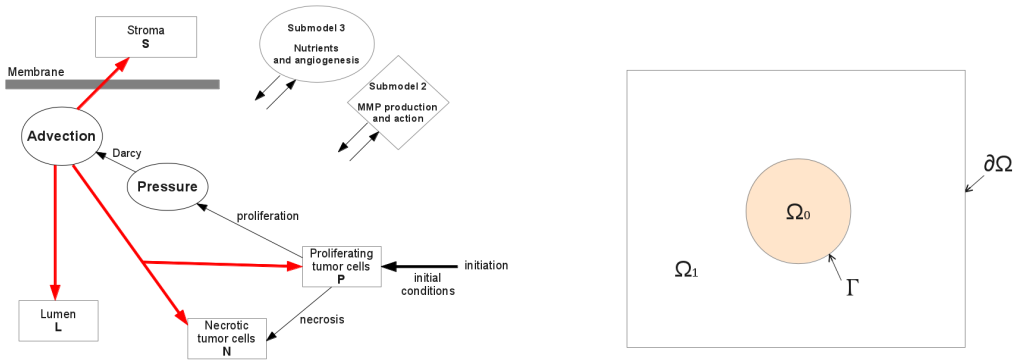

(a) Submodel 1 (b) Geometry

FIGURE 3. Schematic diagram of Submodel 1 and geometry.

where α_P and α_N denote the rates of proliferation and necrosis, respectively. The necrosis rate is a transition rate between proliferating and necrotic cells. Using the saturation condition (62), we obtain the divergence of the velocity in Ω:

$$\nabla \cdot \mathbf{v} = \alpha_P P. \tag{64}$$

The proliferation and necrosis rates are driven by genetic internal factors and by environmental factors: the nutrient concentration Θ and the pressure Π:

$$\alpha_P = \alpha\, f_P, \qquad \alpha_N = \alpha\, f_N,$$

where α is a generic rate which is weighted by the functions f_P and f_N:

$$f_P(\Theta, \Pi) = \alpha_G \frac{1 + \tanh\left[\Lambda_P(\Theta - \Theta_H)\right]}{2} \frac{\Pi^{max} - \Pi}{\Pi^{max}}, \tag{65a}$$

$$f_N(\Theta) = \frac{1 - \tanh\left[\Lambda_N(\Theta - \Theta_N)\right]}{2}. \tag{65b}$$

In the above equalities,

- Π^{max} denotes the maximal pressure that cancer cells can withstand before stopping their mitoses. Θ_H and Θ_N are the hypoxia and necrosis thresholds for nutrient concentration Θ. We impose

  $$0 < \Theta_N < \Theta_H,$$

  such that for Θ smaller than Θ_N cancer cells P turn into necrotic cells N, between Θ_N and Θ_H the cells P do not proliferate, but are not necrotic: they are in a quiescent phase. Above Θ_H the proliferating cells P proliferate and the tumor grows.
- Λ_P and Λ_N are strictly positive constants, homogeneous to the inverse of a concentration. They give the slopes of the curves representing f_P and f_N in the neighborhood of the thresholds Θ_H and Θ_N,
- α_G is a weight function whose value is between 0 and 1. It represents the quantitative influence of oncogenic factors, such as the overexpression of estrogen receptors or other growth factor receptors like HER-2 [76, 107]. In this study, for the sake of simplicity, α_G is supposed to be homogeneous and constant.

Darcy law is imposed to link the velocity to the pressure [5]. Since the membrane is a thin-layer of very low permeability, we link the outer and inner media thanks to Kedem-Katchalsky conditions[3] [57, 80]:

$$-\nabla\cdot(k\nabla\Pi)=\alpha_P P \qquad \text{in} \quad \Omega_0\cup\Omega_1, \tag{66a}$$

$$[\![k\partial_n\Pi]\!]=0, \tag{66b}$$

$$\kappa_m[\![\Pi]\!]=k\partial_n\Pi|_{\Gamma^+}\,, \tag{66c}$$

$$\Pi|_{\partial\Omega}=0, \tag{66d}$$

where

- The medium permeability is denoted by k and depends on cellular species:
$$k=k_L L+k_S S+k_N N+k_P P,$$
- κ_m represents the surface membrane permeability.

1.1.b. *Submodel 2: the Role of MMPs.* In our model, P cells are supposed to produce MMPs which are locally diffused. Then, they degrade the ECM of the biological tissues: membrane, stroma, tumor (Figure 4).

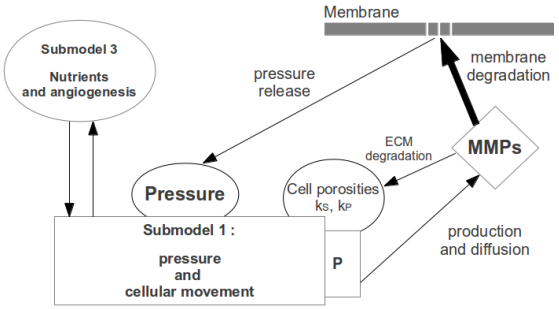

FIGURE 4. Schematic diagram of submodel 2.

The pressure accumulated in the tumor that was previously confined to the duct, tends to limit and block the proliferation. But as soon as the membrane is damaged by the action of MMPs, the pressure is released, the cell divisions restart and tumor cells can cross the membrane to invade healthy tissue. MMPs make the basement membrane porous and can break it, by degrading the extracellular matrix, that is to say by breaking cellular adhesions. While the membrane is intact, the membrane permeability is denoted by κ^0 which is very small: cells cannot cross the membrane. Conversely, a high permeability means that the junctions are fewer and the tissue is more permeable: relation (66c) then expresses the fact that the pressure flux is non-zero across the membrane, as well as the velocity (according to Darcy law). Thus, the action of MMPs, whose concentration is denoted by M is described by

$$\kappa_m(t,x)=\kappa^0+(\kappa^{max}-\kappa^0)\sup_{s\in[0,t]}\left(\frac{1+\tanh\left[\Lambda_M(M(s,x)-M_{th})\right]}{2}\right), \tag{67}$$

where

- κ^0 denotes the very low membrane permeability when it is intact,
- κ^{max} denotes the membrane permeability when it is completely degraded,
- Λ_M is strictly positive, homogeneous to the inverse of a concentration, and gives the slope of the curve,
- M_{th} is the enzymatic threshold from which the MMPs start to degrade the membrane.

[3] Brackets $[\![\cdot]\!]$denote the jump from Ω_0 to Ω_1 across the membrane Γ,

We neglect the regeneration of the basement membrane. In the expression (67), the supremum in time therefore reflects the irreversibility of the degradation phenomenon.

The production of MMPs has been extensively studied in biological literature but remains still unclear because of its complexity [35, 78, 58]. We thus provide a simple reaction–diffusion model :

$$\partial_t M - \nabla \cdot (D_M \nabla M) = \alpha_M P \, đ_0 - \mu M, \tag{68a}$$

$$M|_{t=0} = 0, \tag{68b}$$

$$M|_{\partial\Omega} = 0, \tag{68c}$$

where the diffusion coefficient D_M has a higher value in the region where cancer cells are located:

$$D_M = D_M^{prod} P + D_M^{diff}(1-P),$$
$$0 < D_M^{diff} < D_M^{prod} < \infty.$$

1.1.c. *Submodel 3: Nutrients and Angiogenesis.* Cells need nutrients, in particular for mitosis. As a result, cancer cells require more nutrients than normal cells. Nutrients, whose concentration is denoted by Θ, are provided by the membrane vascularization and by the angiogenetic process, assumed to occur during the invasive stage (Figure 5).

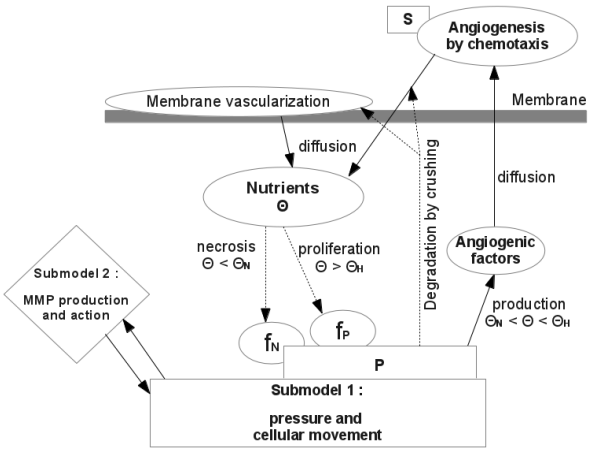

FIGURE 5. Schematic diagram of submodel 3.

Avascular stage. The vascularization of the membrane is the only source of nutrients at the **avascular** stage of tumor growth. We assume that this is an average vascularization on Γ, providing at each point of Γ a constant nutrient concentration equal to Θ^{max} at the constant rate α_θ. It is further assumed that the capillaries are damaged at a constant rate β, when tumor cells P invade and crush them. We thus define this source of nutrients by

$$S_{memb} = (\alpha_\theta - \beta\, P)\, \Theta^{max} \mathbb{1}_\Gamma. \tag{69}$$

where $\mathbb{1}$ denotes the indicator function.

Angiogenesis. The second source of nutrients is angiogenesis, at the stage of **vascular** growth. We use a model of angiogenesis similar to the one of F. Billy [12]. When the tumor infiltrates outside the duct, it needs more and more nutrients as the number of proliferating cells grows. Then, the hypoxic cells react by producing angiogenic factors, of concentration denoted by ξ, which are diffused:

$$-\nabla \cdot (D_\xi \nabla \xi) = \alpha_\xi f_\xi P \, đ_0, \qquad \text{on} \quad \Omega, \tag{70a}$$

$$\xi|_{\partial\Omega} = 0. \tag{70b}$$

The production rate of angiogenic factors, denoted by α_ξ, is weighted by the function f_ξ that contains the hypoxic condition:

$$f_\xi(\Theta) = \frac{1 - \tanh\left[\Lambda_\xi(\Theta - \Theta_H)(\Theta - \Theta_N)\right]}{2} \tag{71}$$

where the parameter Λ_ξ is homogeneous to the square of a concentration. The signal ξ implies the formation of new blood vessels, composed of endothelial cells, according to the well-known biological process of chemotaxis. Endothelial cells are a part of S cells. Their proportion relative to the cells S is denoted by ν. They are provided at the rate α_ν by the initial blood network $\mathcal{R}_0$, which is assumed to be composed only of endothelial cells. They are then transported in the direction of the gradient of the angiogenic factors, leading to the formation of a new vasculature $\mathcal{R}$. ν is thus driven by the following equations:

$$\partial_t \nu + \nabla \cdot (\chi\, \nu\, \nabla \xi) = \alpha_\nu \mathbb{1}_{\mathcal{R}_0} + (\alpha_\nu - \beta\, P)\, \nu\, (1 - \nu)\, \mathbb{1}_{\mathcal{R}}, \qquad \text{on} \quad \Omega, \tag{72a}$$

$$\nu|_{\partial\Omega} = 0 \tag{72b}$$

$$\nu|_{\mathcal{R}_0} = 1 \tag{72c}$$

$$\nu|_{t=0} = 0, \qquad \text{on} \quad \Omega \setminus \mathcal{R}_0. \tag{72d}$$

where

$$\mathcal{R}|_{t=0} = \emptyset, \quad \mathcal{R} = \{(t,x) : \nu(t,x) \geq \nu_{min}\}.$$

The new vasculature $\mathcal{R}$ also provides endothelial cells at the rate α_ν, and is subject to degradation by P cells at the rate β. The term $(1-\nu)$ is a term of saturation to prevent overcrowding. The chemotaxis coefficient χ is built so that the endothelial cells are easily transported in lumen and healthy tissue and do not progress in the tumor tissue and through the basement membrane:

$$\chi = \chi_L L + \chi_S S.$$

Finally, considering that the new vascularization diffuses a concentration of nutrients denoted by Θ_ν^{max} at the constant rate α_{θ_ν}, the second source of nutrients is given by

$$S_{angio} = \alpha_{\theta_\nu} \Theta_\nu^{max} \mathbb{1}_{\mathcal{R}_0 \cup \mathcal{R}}. \tag{73}$$

Diffusion of nutrient. The diffusion of nutrients from the two sources S_{memb} and S_{angio}, is assumed to be instantaneous and is described by a static diffusion equation in the domain Ω_1:

$$-\nabla \cdot (D_\theta \nabla \Theta) = S_{angio} + S_{memb} - \lambda \alpha_P P \Theta, \qquad \text{on} \quad \Omega, \tag{74a}$$

$$\Theta|_{\partial\Omega} = 0, \quad \partial_n \Theta|_{\partial\Omega} = 0, \tag{74b}$$

where P cells are supposed to consume nutrients at rate $\lambda\alpha_P$ and D_θ denotes the diffusion coefficient. Inside the duct, the diffusion is radial and of the order of magnitude of $\delta_0 = 1$ millimeter from Γ:

$$\Theta(x) = \begin{cases} \Theta|_\Gamma \, \exp\left(-\frac{\text{dist}(x,\Gamma)}{\delta_0 - \text{dist}(x,\Gamma)}\right), & \text{if } \text{dist}(x,\Gamma) < \delta_0, \\ 0, & \text{otherwise.} \end{cases} \tag{75}$$

The above model is capable of reproducing the behavior of a carcinoma that infiltrates through the membrane, but it remains relatively unsatisfactory when compared with biomedical results, since it cannot provide hetergeneous growth. We refer to Section 3 of [28] for an exhaustive presentation of the numerical results. For the sake of conciseness, we do not present the numerical simulations of the fully deterministic model. In the next paragraph we provide several hypotheses that may explain tumor growth heterogeneity. This part is prospective and should be investigated in forthcoming research.

1.2. Different hypotheses for tumor heterogeneity. It is worth noting that even with random initial data, the above fully deterministic model provide tumor growth which is still too uniform as illustrated by Figure 6(a), compared with biopsy image Figure 6(b). We proposed to overcome this lack of heterogeneity by first considering the effect of a genetic mutation within the tumor, and then the influence of the microenvironment on the production of MMPs and TNFs.

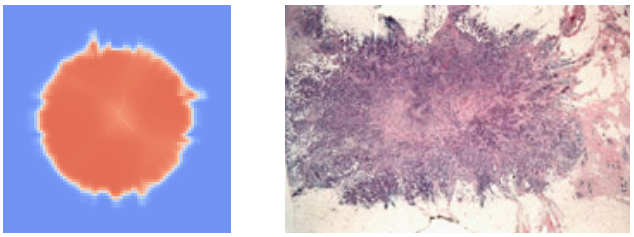

FIGURE 6. Invasive tumors (biopsy from [113]). The simulation gives a too symmetrical tumor.

1.2.a. *Different cell species to mimic the influence of genetic mutations of tumor cells.* It is well known that genetic factors are critical in tumor initiation and progression. As cancer is the result of genetic mutations that can be seen as random in space, a tumor is usually inhomogeneous in terms of growth and substances which it produces. We assumed in previous section that each cell produced MMPs from the initial time. We now consider that a random mutation is occuring in a few selected cells that makes them produce MMPs (Figure 7). A genetic mutation means that a cell acquires a specific property which is cloned

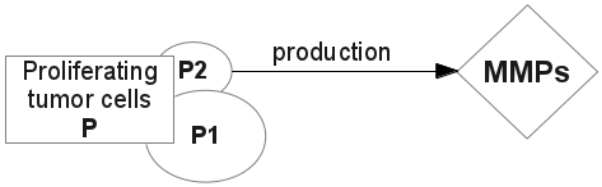

FIGURE 7. Genetic influence on MMP production.

during cell division. It requires the definition of new species for each mutation. We then introduce two species of proliferative cells, P_1 and P_2. MMPs are only produced by P_2. They satisfy the same advection equation (63a) than P:

$$\partial_t P_1 + \nabla \cdot (\mathbf{v} P_1) = (\alpha_P - \alpha_N) P_1, \tag{76a}$$

$$\partial_t P_2 + \nabla \cdot (\mathbf{v} P_2) = (\alpha_P - \alpha_N) P_2, \tag{76b}$$

$$P = P_1 + P_2, \tag{76c}$$

and relation (68a) becomes

$$\partial_t M - \nabla \cdot (D_M \nabla M) = \alpha_M P_2 \, đ_0 - \mu M. \tag{76d}$$

Starting with initial conditions P_1^0 and P_2^0 that are randomly distributed, makes it possible to provide heterogeneous tumor growth, as given by Figure 8. We could consider that genetic mutations occur later

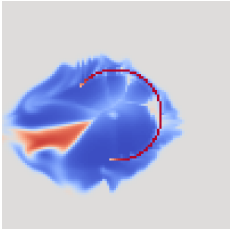

FIGURE 8. Invasive carcinoma with two populations of proliferating cells. $P1$ cells are in blue. $P2$ cells, in red, produce MMPs ($\alpha = 5$).

and obtain the same kind of results. Obviously, it is possible to introduce some other genetic mutations. For example, some onco-genetic mutations imply overexpression of cell receptors like HER-2 that, when activated, increase the mitosis rate. This phenomenon has already been modeled [107] and leads to a rate α_G becoming variable in space and time, in relation (65a). Then, the proliferation rate would be inhomogeneous and could also lead to various shapes of tumor. What can be retained is that different genetic mutations can be simulated and give more realistic results, with inhomogeneities in the growth and shape of the tumor.

1.2.b. *Influence of the microenvironment on production of MMPs.* Another source of heterogeneity can be the influence of microenvironment, since many recent studies underline that it has a deep impact on cancer growth. We focus on the impact of the microenvironment on the production of MMPs, which leads us to improve and complexify the model (Figure 9). Some studies mention the role played by cells of epithelial

FIGURE 9. Schematic diagram of model improvements.

tissue (myoepithelial cells) and stromal cells (fibroblasts, macrophages of the immune system, etc.) in MMP production [16, 21, 49, 91]. In response to a signal from the tumor, stromal cells migrate towards the duct and produce MMPs as inactive proenzymes. These are then activated by forming complexes with MMPs produced by tumor cells (Figure 10(a)).

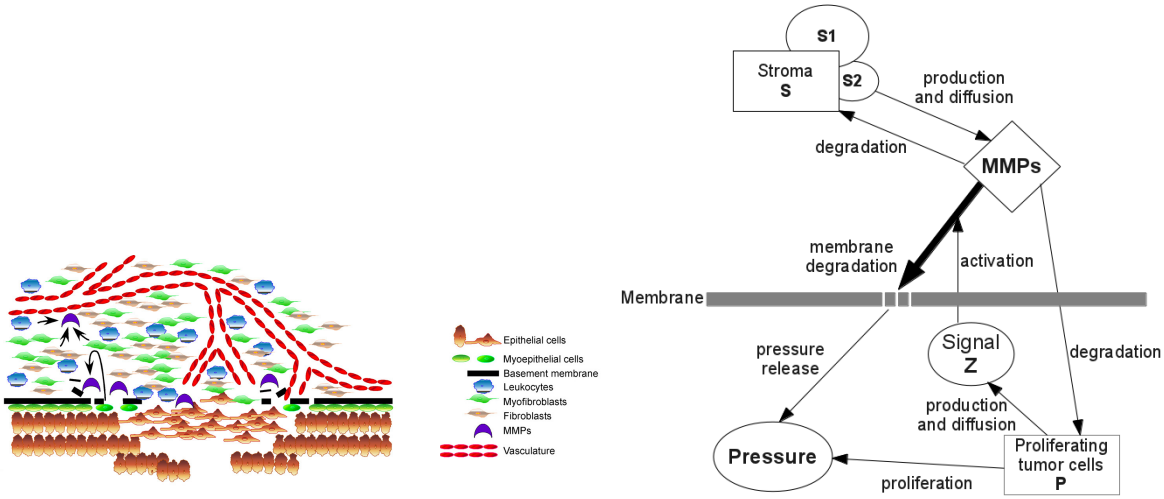

(a) Role of stroma in membrane degradation

(b) Schematic diagram of MMP production

FIGURE 10. Role of stroma in MMP production, and its implication in our modeling [49].

To model these processes simply, some stromal cells S are randomly labeled as **fibroblasts** denoted by S_2, which avoids introducing a new population that would migrate to the tumor: the important point is that these cells can produce MMPs. Other stroma cells are denoted by S_1. Then, proliferative cells diffuse a chemical signal, of concentration Z, to activate the proenzymes (Figure 10(b)). The local action of the signal is simulated with the same diffusion coefficient than for MMPs. Actually, we assume that the MMP

production starts only if the signal concentration reach a certain threshold Z_s. We therefore set:

$$\partial_t S_1 + \nabla \cdot (\mathbf{v} S_1) = 0, \tag{77a}$$

$$\partial_t S_2 + \nabla \cdot (\mathbf{v} S_2) = 0, \tag{77b}$$

$$S = S_1 + S_2. \tag{77c}$$

Equation (68a) is replaced by

$$\partial_t M - \nabla \cdot (D_M \nabla M) = \gamma(Z) S_2 \, đ_0 - \mu M, \tag{77d}$$

$$\partial_t Z - \nabla \cdot (D_M \nabla Z) = \alpha_z P \, đ_0 - \mu Z, \tag{77e}$$

$$Z|_{t=0} = 0, \quad M|_{t=0} = 0, \quad Z|_{\partial\Omega} = 0, \quad M|_{\partial\Omega} = 0 \tag{77f}$$

where

$$\gamma(Z) = \alpha_M \left(\frac{1 + \tanh\left[\Lambda_z (Z - Z_{th})\right]}{2} \right),$$

and Λ_z is homogeneous to the inverse of a concentration. As initial conditions, S_2^0 cells are randomly distributed around the duct membrane. The results in Figure 11(a) show a localized breaking point in the membrane. This more localized gap is due to the random distribution of stromal cells that produce MMPs. Before the membrane is completely destroyed, the tumor starts to come out and invade healthy

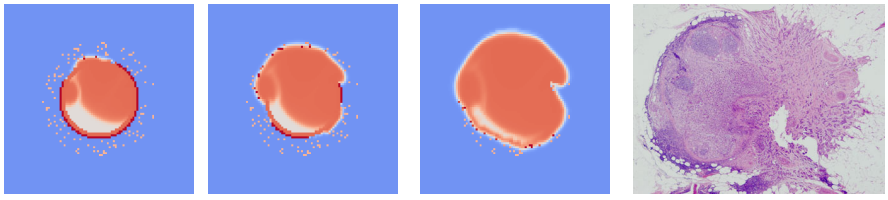

(a) $t = 11$ (b) $t = 12$ (c) $t = 13$ (d) Biopsy [75]

FIGURE 11. Improved model simulating the evolution of an invasive carcinoma ($\alpha = 5$).

tissue, brimming over the duct. The resulting tumor is asymmetrical and an analogy is observed between tumor shapes in Figure 11(c) and Figure 11(d).

1.2.c. *TNF action on the tumor necrotic core.* In the same vein, we can take another microenvironmental influence into acount: the TNF action on necrosis core (Figure 12). The lack of nutrient is not the only responsible for the development of a necrotic core: the tumor necrosis factors (TNFs) seem to be involved with conflicting effects [117, 47]. It is a chemical secreted by immune cells that infiltrated the tumor and that cause cell death. TNFs could also play a role in promoting cancer: initiation, proliferation of malignant cells, angiogenesis and metastases production. Motivated by the idea of modeling more realistic necroses, larger and with an irregular shape (Figure 13(c)), we decide to take the TNF actions into account. TNFs are supposed to be produced and diffused by infiltrating macrophages, denoted P', which are chosen among P cells, randomly in space and time,

$$-\nabla \cdot (D_\tau \nabla \tau) = \alpha_\tau P' \, đ_0, \tag{78}$$

where τ denotes the TNF concentration with $\tau^0 = 0$.

The action of TNF on the rate of necrosis α_N is introduced in the weight function f_N and is assumed to be described by equation (79) instead of equation (65b):

$$f_N = 1 - \frac{1}{4} \left[1 + \tanh\left(\Lambda_N(\Theta - \Theta_N)\right)\right] \cdot \left[1 - \tanh\left(\Lambda_\tau(\tau - \tau_{th})\right)\right], \tag{79}$$

where Λ_τ is homogeneous to the inverse of a concentration. For a given concentration of nutrients, the rate of necrosis increases if the TNF concentration exceeds a certain threshold τ_{th}. The simulations reveal a more extensive and irregular necrosis (Figure 13(b)) than if only hypoxia is involved (Figure 13(a)). The wider necrosis is due to the increase in necrosis rate, and its irregularity to the random distribution of

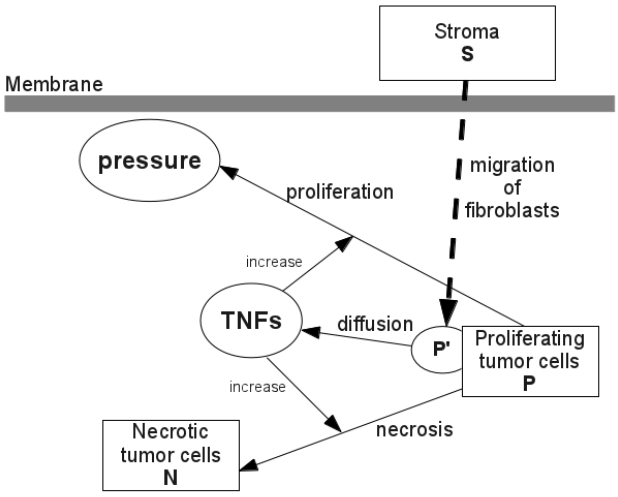

FIGURE 12. Schematic diagram of TNF production and action on necrosis and proliferation rates.

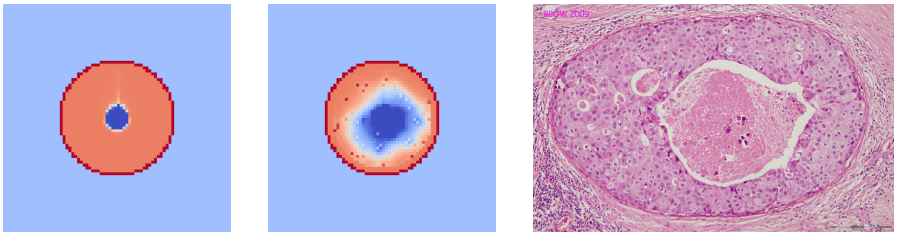

(a) $\alpha_\tau = 0$ (b) $\alpha_\tau = 1000$ (c) Comedo-carcinoma from [75]

FIGURE 13. Simulation of the TNF effect on tumor necrosis ($t = 11$, $\Lambda_\tau = 8$, $D_\tau = 2$, $\tau_{th} = 0.5$).

macrophages. Introducing the action of TNFs in the calculation of the weight function f_P of the proliferation rate (equation (65a)), in the same way as in equation (79), we could also simulate a faster growth under the influence of TNFs, as they are supposed to promote tumor cells proliferation. Once again, despite a very partial modeling of biological processes involved, the results seem more realistic (Figure 13(b) and Figure 13(c)) when the microenvironment is taken into account.

1.3. Pros and cons of the modeling. We conclude this section by summing up the advantages and the drawbacks of our model.

Considering that the permeability of the medium simulates correctly the degree of cell adhesion within tissues, the process of membrane degradation was described by the permeability, which is a function of enzyme concentration. The simulations highlighted the degradation of the membrane, the spread of malignant cells outside the duct and the tumor invasion. To avoid to homogeneous growth, we first introduce some genetic factors, and secondly some influences of the microenvironment. It is worth noting that quite satisfactory results have been obtained at least qualitatively. In particular, our results seem to support the idea that microenvironmental factors play a crucial role in tumor progression, in agreement with many recent studies in oncology [13, 21, 50].

However, in spite of these satisfactory behaviors, we can highlight some points for further study. The use of Darcy law, at the heart of the model, raises issues that indicate some limits of the model. First, when the tumor grows and fills the duct, it may tend to deform the duct membrane, implying a feedback on the rate of tumor growth due to the membrane elasticity. To take the membrane elasticity into account,

we could use a Stokes law [15, 43] rather than Darcy law, which would significantly complexify the model. Secondly, carcinoma **in situ** may have very different architectures from one cancer to another. The model provides only two of the main types of breast carcinomas: solid and comedo carcinomas. Other types of breast intraductal carcinoma mentioned in the medical literature are:

- the micropapillary carcinoma develops along the epithelium, with tumor cells projections towards the center of the duct, without filling (Figure 14(a))
- the papillary carcinoma develops inside the duct with irregular shapes (Figure 14(b))
- the cribriform carcinoma is caracterized by distinctive holes between the cancer cells (Figure 14(c)).

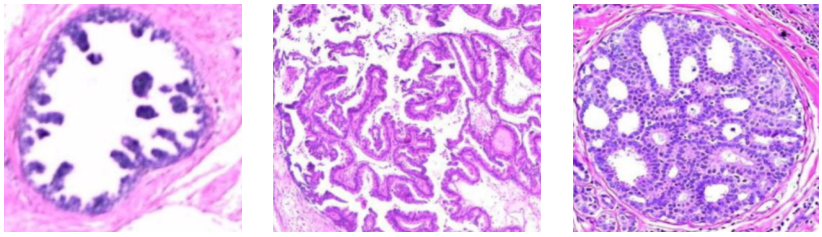

(a) micropapillary (b) papillary (c) cribriform

FIGURE 14. Other types of intraductal carcinoma. Taken from [95].

The modeling of these types of carcinomas are more difficult to address: in each case (Figure 14), projections and spans of tumor cells appear to indicate that some of adhesion and polarity properties have been kept by the cells. In our model, the permeability coefficient, introduced with Darcy law, does not distinguish between the different types of adherent junctions. Above all, it simulates neither the polarization of proliferating cells nor the orientation of cell divisions. Thus, the continuous model finds its limits when it comes to simulate phenomena that are played at the cellular level. A discrete model, where each cell is modeled by an agent, like in [34, 66, 67], seems more appropriate. Note that there still remains numerous unanswered questions regarding the biological phenomena that are involved: the impact of the pressure, or mechanical stress, on tumor growth seems to be ambiguous [121, 111]. It could even have an impact on genetic mutations and production of MMPs. The production of MMPs seems even more complex than what we simulated, involving different kinds of MMPs. The structure and activity of the membrane, here reduced to an interface, could also be a determining factor in the invasive process [50]. Finally, the migration of specific cells of the microenvironment (such as immune cells, macrophages, fibroblasts), randomly simulated in our study, should be further studied in the hope of bringing predictability to the model.

It is worth noting that according to our model, either oncogenic or microenvironmental factors make possible to obtain heterogeneous tumors, in accordance with biopsies. Our result can be seen as a first step in the study of the influence of these factors, and in their modeling in order to provide realistic tumor shapes.

2. On-going research on tumor growth models

I conclude this chapter by presenting the on-going research on tumor growth modeling. These works are the part of the PhD theses of T. Michel on one side and F. Cornelis and G. Lefebvre on the other side, that are PhD candidates of the team.

2.1. Mathematical properties of a generic tumor growth model. In the thesis of T. Michel, we are interested in the well-posedness of a simplified version of tumor growth model, where the action of therapy has been introduced. More precisely, we consider the following model where two species of proliferative tumor cells are involved. The first type of cancer cells is assumed to be sensitive to the treatment, we track them by P_1, while the second type, P_2 is assumed to be resistant to the treatment. The proliferative rate of these two kinds of cells is a smooth function denoted by $\gamma(M)$, where M is related to nutriens supply and vascularization. The efficiency of the treatment is proportional to MP_1, and the cancer cell densities satisfy

$$\partial_t P_1 + \nabla \cdot (vP_1) = \gamma(M)P_1 - \delta M P_1, \tag{80a}$$

$$\partial_t P_2 + \nabla \cdot (vP_2) = \gamma(M)P_2 \tag{80b}$$

We also introduce necrotic cells that are cancer cells killed by the treatment or by hypoxia, whose density denoted by N satisfies

$$\partial_t N + \nabla \cdot (vN) = \delta M P_1 + [\gamma(M)]^-(P_1 + P_2) - \frac{1}{\tau}N, \tag{80c}$$

Similarly to the ductal carcinoma model, healthy cells satisfy equation (63c). The assumption

$$P_1 + P_2 + N + S = 1, \tag{80d}$$

leads to

$$\nabla \cdot v = [\gamma(M)]^+(P_1 + P_2) - \frac{1}{\tau}N, \tag{80e}$$

and the system is close by a Darcy law:

$$v = -k\nabla \Pi, \tag{80f}$$

$$\Pi|_{\partial\Omega} = 0. \tag{80g}$$

Note that since no membrane are accounted for, the pressure is H^1 in the whole domain, unlike the solution to (66). Simple model for angiogenesis is used. Tumor cells are supposed to produce a signal, ξ defined by

$$\partial_t \xi = \alpha \int_\Omega \frac{[\gamma(M)]^-}{\gamma_1} P dx - \lambda \xi, \tag{80h}$$

and the vascularization M is assume to come from the health tissue and satisfies

$$\partial_t M + \nabla \cdot (M\xi \nabla P) = -\eta M P + C_0 S(1 - M) + \Delta M. \tag{80i}$$

We are interested in the existence and uniqueness of the solution to problem (80) in appropriate Sobolev spaces. In particular, we have shown thanks to a classical (but tricky) fixed-point method, existence and uniqueness hold independently of τ. We also investigated the limit $\tau \to 0$ and we show that for well-prepared initial conditions, the solution to problem (80) converges to the solution to the problem without necrotic phase:

$$\left\{ \begin{array}{rcl} \partial_t P_1 + \nabla \cdot (vP_1) &=& \gamma(M)P_1 - \delta M P_1, \\ \partial_t P_2 + \nabla \cdot (vP_2) &=& \gamma(M)P_2, \\ \partial_t S + \nabla \cdot (vS) &=& 0, \\ P_1 + P_2 + S &=& 1, \\ \nabla \cdot v &=& \gamma(M)(P_1 + P_2) - \delta M P_1, \\ v &=& -k\nabla \Pi, \\ \Pi|_{\partial\Omega} &=& 0, \\ \partial_t M - \Delta M + \nabla \cdot (M\xi \nabla P) &=& -\eta M P + C_0 S(1 - M), \\ \partial_t \xi &=& \alpha \displaystyle\int_\Omega \frac{[\gamma(M)]^-}{\gamma_1} P dx - \lambda \xi. \end{array} \right. \tag{81}$$

2.2. Drug Resistance of GIST Liver Metastases. Gastrointestinal stromal tumors (GIST) are the most common mesenchymal tumors of the gastrointestinal tract, whose pathogenesis is characterized by an important variability in molecular alterations. This makes metastatic GIST a clinical model for personalized targeted therapies in cancer treatment. The aim of this on-going work with T. Colin, O. Saut and the PhD students F. Cornelis and G. Lefebvre, is to provide a spatial model of GIST liver metastasis growth based on medical images. The ultimate goal is possibly to highlight more crucial data such as tumor heterogeneities and geometrical properties of the tumor growth, which may provide more precise indicators than the RECIST criteria.

Actually, as shown by scans of Figure 15, the metastasis growth is far from homogeneous. More precisely

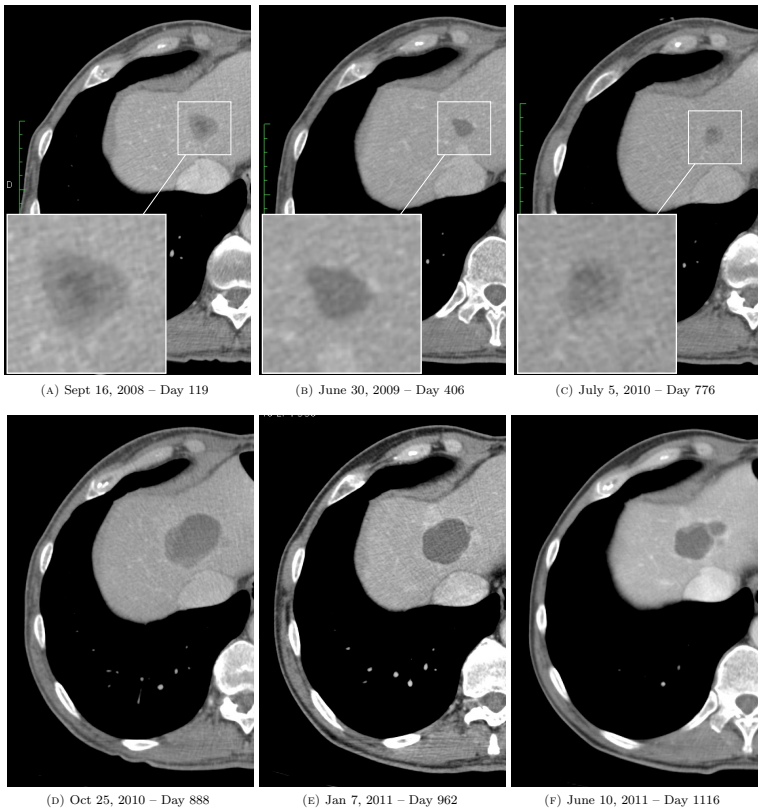

(A) Sept 16, 2008 – Day 119 (B) June 30, 2009 – Day 406 (C) July 5, 2010 – Day 776

(D) Oct 25, 2010 – Day 888 (E) Jan 7, 2011 – Day 962 (F) June 10, 2011 – Day 1116

FIGURE 15. Evolution GIST metastasis a specific patient

we aim at modeling the following observations from the scans of Figure 15:

(A) During the initial growth – before the treatment – the tumor is very heterogeneous.
(B) During the first phase of the evolution with the imatinib (cytotoxic drug), the lesion becomes smaller and very homogeneous. This may correspond to a low cellular activity.
(C) Before the relapse, some heterogeneity appears: a rim of proliferative cells is visible while the center is composed of necrotic cells (darker). Let us note that even if the cellular division has started again, the tumor area has not yet increase.
(D) When the imatinib failure is obvious (increase of area), clinicians change the treatment. Usually, a multi-targeted recepetor tyrosine kinase inhibitor, sunitinib, which has an antiangiogenic treatment is used: the.
(E) The tumor area has decreased again. The tumor becomes darker: this may correspond to an increase of necrotic cells rate in a tumor. The heterogeneity is also reduced. However, the phenomenon is less important than under imatinib.
(F) Before the new therapeutic failure, the tumor becomes heterogeneous again: the tumor growth restarts from the boundary of the necrosis part.

The modeling is based on the description of 3 cancer cells types, in the same vein as the models previously presented: one is resistant to both imatinib and sunitinib, and a second type resistant to imatinib only and the third one is killed by both drugs. The other parts of the model are quite similar to the generic model of subsection 2.1 and thus we do not present them here. Preliminary numerical results provide very realistic tumor growth and we found parameters that makes it possible to reproduce the images of Figure 15, as shown by Figure 16. With the same parameters, in Figure 17 we compared the numerical tumor area with the measured area from the scans, and we see that the model fits quite well the data.

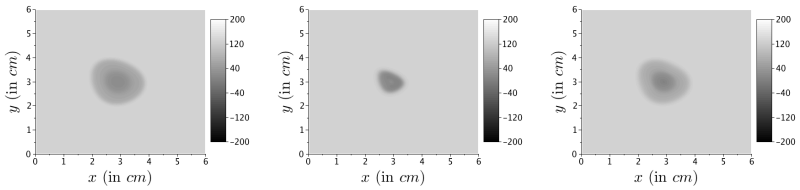

(A) Day 119 (B) Day 409 (C) Day 778

(D) Day 870 (E) Day 961 (F) Day 1120

FIGURE 16. Numerical simulations of the GIST liver model fitted with scans of Figure 15

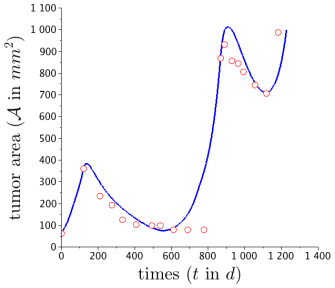

FIGURE 17. Comparison between numerical tumor areas with the data of Figure 15

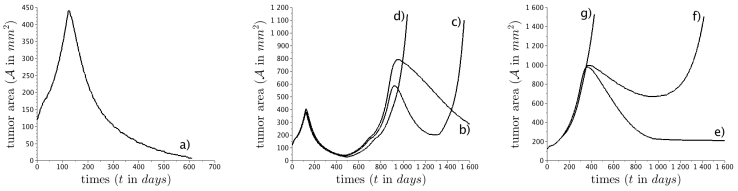

(A) Imatinib from 119^{th} day

(B-C-D) Imatinib from 119^{th} day until 867^{th} day and sunitinib just after

(E-F-G) Imatinib from 119^{th} day until 300^{th} day and sunitinib just after

FIGURE 18. Different behaviors that have been obtained by fitting the initial part

Therefore we have obtained a model that makes it possible to fit with the GIST liver metastasis evolution. Unfortunately, this model is not predictive in the sense with a few scans (let say 2 or 3), it is not possible to predict the relapse time. Actually we can find initial conditions and parameters that fits well the initial evolution but provides very different results for long-term (see Figure 18. This means that we need more information. The forthcoming works will consist in using more clinical data, such as biopsys or functional medical imaging to discriminate between possible behaviors.

2.3. Publication related to this chapter.

- Colin, T., Gallinato, O., **Poignard, C.**, Saut, O. (2014), *Tumor growth model for ductal carcinoma: from* **in situ** *phase to stroma invasion.* Inria Research Report RR–8502, Submitted.

CHAPTER IV

Some Results in Asymptotic Analysis for Electromagnetism

This chapter is devoted to asymptotic analysis of static problems in electromagnetism. This research is motivated by collaborations in the electrical engineering research area, and more precisely by a tigh collaboration with researchers of the Ampère laboratory of Lyon. The following results are in the continuity of my PhD research. They can be split into two parts: first we present approximate transmission conditions through a periodically rough thin layer, and we characterize the influence of such a layer on the polarization tensor. Then we focus on the eddy current problem in domain with a corner singularity. Note that all the PDEs of this chapter are time-independent and linear, and we focus on the bidimensional case.

1. Transmission conditions through a rough thin layer for the conductivity problem

The aim of this section consists in deriving *transmission* conditions for the electrostatic potential that are equivalent to a rough thin layer in the case of periodic roughness[1]. We consider a smooth and bounded

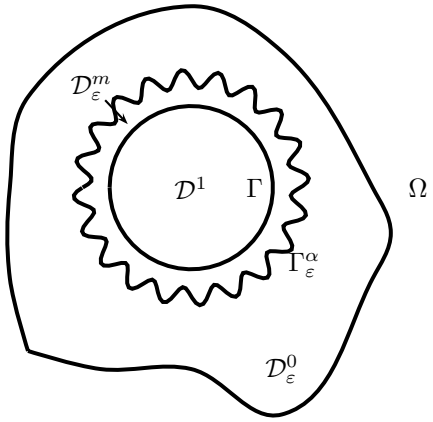

FIGURE 1. Geometry of the domain with rough thin layer.

domain $\mathcal{D}$ in $\mathbb{R}^2$ with connected boundary $\partial\mathcal{D}$. Let $\varepsilon > 0$ and $\alpha > 0$ be small positive parameters. We split $\mathcal{D}$ into three subdomains: $\mathcal{D}^1$, $\mathcal{D}_\varepsilon^m$ and $\mathcal{D}_\varepsilon^0$. The domain $\mathcal{D}^1$ is a smooth domain strictly embedded in $\mathcal{D}$ (see Figure 1), and we denote by Γ its boundary, which is a connected smooth curve of length 1 by convention. Denoting by Ψ the parameterization of Γ, the curve Γ^α is described thanks to a periodic function f:

$$\Gamma_\varepsilon^\alpha = \partial\mathcal{D}_\varepsilon^m \setminus \Gamma = \{\Psi(\theta) + \varepsilon f(\theta/\varepsilon^\alpha) n(\theta), \quad \theta \in \mathbb{T}\},$$

ε is the membrane average thickness, and the parameter α measures the degree of roughness. The domain $\mathcal{D}_\varepsilon^m$ is the connected component of the domain located between Γ and $\Gamma_\varepsilon^\alpha$, and $\mathcal{D}_\varepsilon^0$ is defined by

$$\mathcal{D}_\varepsilon^0 = \mathcal{D} \setminus \overline{\mathcal{D}_\varepsilon^m \cup \mathcal{D}^1}. \quad \text{We also set} \quad \mathcal{D}^0 = \mathcal{D} \setminus \overline{\mathcal{D}^1}.$$

[1]Note that one can extend the following results to a quasi-periodic roughness, but for the sake of clarity we do not present this case in this manuscript.

The conductivity charts, denoted respectively by σ^ε in the pertubed domain and by σ in the unperturbed domain are given by

$$\sigma^\varepsilon(z) = \begin{cases} \sigma_1, \text{ if } z \in \mathcal{D}^1, \\ \sigma_m, \text{ if } z \in \mathcal{D}_\varepsilon^m, \\ \sigma_0, \text{ if } z \in \mathcal{D}_\varepsilon^0, \end{cases} \qquad \sigma(z) = \begin{cases} \sigma_1, \text{ if } z \in \mathcal{D}^1, \\ \sigma_0, \text{ if } z \in \mathcal{D}^0, \end{cases}$$

where σ_1, σ_m et σ_0 are strictly positive constants. For g regular enough on $\partial\mathcal{D}$, the steady state potential u_ε in the perturbed domain and the "background" potential u_0 in the unperturbed domain are the respective solutions to

$$\nabla \cdot (\sigma^\varepsilon \nabla u_\varepsilon) = 0, \text{ in } \mathcal{D}, \tag{82a}$$

$$u_\varepsilon|_{\partial\mathcal{D}} = g, \tag{82b}$$

$$\nabla \cdot (\sigma \nabla u_0) = 0, \text{ in } \mathcal{D}, \tag{83a}$$

$$u_0|_{\partial\mathcal{D}} = g. \tag{83b}$$

According to Capdeboscq and Vogelius [19], the polarization tensor makes it possible to characterize the influence of the inhomogeneity $\mathcal{D}_\varepsilon^m$ on the "background" solution. More precisely, there exists a symmetric definite positive matrix $\mathcal{M}_\alpha$ such that for any $y \in \mathcal{D}$ far from $\mathcal{D}_\varepsilon^m$,

$$u^\varepsilon(y) - u^0(y) = \varepsilon(\sigma_m - \sigma_0) \int_\Gamma \mathcal{M}_\alpha \begin{pmatrix} \partial_n u^0 \\ \nabla_\Gamma u^0 \end{pmatrix} \cdot \begin{pmatrix} \partial_n G \\ \nabla_\Gamma G \end{pmatrix} (\cdot, y)\, \mathrm{d}s + o(\varepsilon),$$

where G is the Dirichlet function:

$$\begin{cases} \nabla_x \cdot \Big(\sigma \nabla_x G(x,y) \Big) = -\delta_y, \text{in } \mathcal{D}, \\ G(x,y) = 0, \quad \forall x \in \partial\mathcal{D}. \end{cases}$$

The aim of this section is to provide explicit formulae for this polarization tensor for our specific problem.

Since almost two decades, several papers have been devoted to rough boundaries through the derivations of equivalent boundary conditions [1, 2, 3, 53] in electromagnetism and fluid mechanics in the case $\alpha = 1$. In 2008, Basson and Gérard-Varet [8] derived approximate boundary condition for a boundary with random roughness. The analysis of these previous papers is essentially based on the construction of the so-called "wall law", which is a boundary condition imposed on an artificial boundary inside the domain. The wall law reflects the large-scale effect on the roughness on the background solution.

Compared to equivalent boundary conditions, the derivation of equivalent transmission conditions leads to several difficulties in the definition of the boundary layer correctors, as shown in [23]. In particular, a naive approach coming from wall law derivation techniques can lead to ill-posed problems satisfied by the boundary layer correctors. However, it is worth noting that the derivation of the boundary layer correctors is very efficient since it provides simultaneously an explicit characterization of the so–called polarization tensor defined in [6, 7, 19] and an accurate description of the electric potential in the vicinity of the inhomogeneity, while the variational techniques as used by Capdeboscq, Vogelius, Beretta *et al.* [19, 10, 11] provide estimates only far from the roughness.

For $\alpha < 1$ in [83], for $\alpha = 1$ in [23, 84], and for $\alpha > 1$ in [25] we derived equivalent transmission conditions for the conductivity problem, and we characterized the polarization tensor. Note that the tools to derive the expansion in the three cases are different: in [83] we performed a rescaling in $1/\varepsilon$ in the normal direction and we write the Euclidean metric and the Laplace operator in the new coordinates. Taking advantage of the weak roughness, we are able to order the terms in power of ε, and then by identification we derive the equivalent transmission conditions. This method fails for the high roughness case $\alpha \geq 1$, since the derivatives in the tangential direction makes appear terms in $\varepsilon^{-\alpha}$, which are not compensated by the terms in ε, and thus it is impossible to order the terms of the Laplace operator. In [23], for the case $\alpha = 1$ we made appear boundary layer correctors defined in the infinite strip with 1 oscillation. However for $\alpha > 1$ the infinite strip is highly oscillating in $\varepsilon^{\alpha-1}$: the boundary layer correctors are defined in a domain which is highly rough, as shown by Figure 2(b). In [25], we used a two-scale analysis to derive the first order transmission conditions. Note that for $\alpha > 1$ only weak results have been obtained in [25] by using two-scale convergence techniques, in the sense that no error estimate has been provided.

Interestingly, in our review [85] we revisit all these results using the general framework based on the derivation of boundary layer correctors in the 3 cases, that makes it possible to treat similarly the three

cases $\alpha < 1$, $\alpha = 1$ and $\alpha > 1$, and we are able to prove error estimates for these three cases. In this section, we present the heuristics of the derivation of these asymptotics and we summarize the results we obtained in [83, 23, 25, 85].

1.1. Heuristics of the derivation of the boundary layer correctors. Since the derivation of the asymptotic analysis is technical, we present in this thesis the heuristics of the analysis on a model problem to clarify the purpose. We refer the reader to [85] and references therein for more details.

Suppose that $\mathcal{D}$ be the cylindrical domain $(-1,1)\times\mathbb{T}$ with null curvature, and let $\mathcal{D}_1$ be $(-1,0)\times\mathbb{T}$. Denoting by $n_0 = (1,0)^T$ the normal to the curve $\{\eta = 0\}$ outwardly directed from $\mathcal{O}_1$ to its outside, the

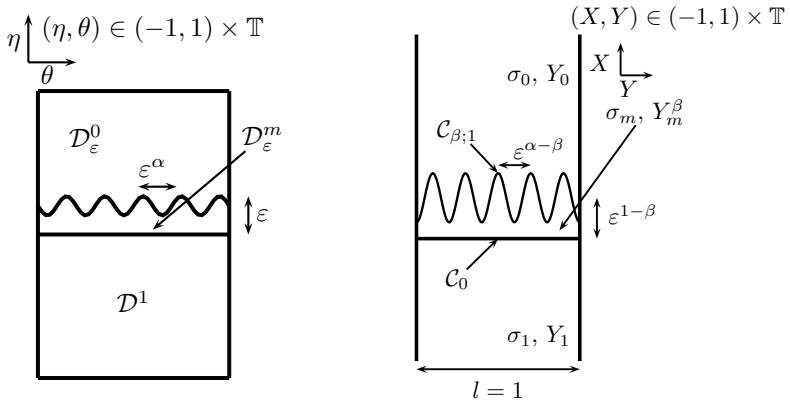

(a) Geometry of the model problem

(b) The infinite strip for the derivation of the correctors

FIGURE 2. Geometry of the model problem and definition of the infinite periodic strip.

normal n_ε to the rough curve $\{(\varepsilon f(\theta/\varepsilon^\alpha,\theta),\theta\in\mathbb{T}\}$ writes

$$n_\varepsilon(\theta/\varepsilon^\alpha) = \frac{1}{\sqrt{1+\varepsilon^{1-\alpha}f'(\theta/\varepsilon^\alpha)}}\begin{pmatrix}1\\ -\varepsilon^{1-\alpha}f'(\theta/\varepsilon^\alpha)\end{pmatrix}.$$

Therefore, the solution to problem (82) is nothing but the continuous θ–periodic function u_ε that satisfies

$$\begin{aligned}
&\partial^2_\eta u_\varepsilon + \partial^2_\theta u_\varepsilon = 0, \quad \text{in the three domains,}\\
&\sigma_0\left(\partial_\eta u_\varepsilon - \varepsilon^{1-\alpha}f'(\theta/\varepsilon^\alpha)\partial_\theta u_\varepsilon\right)\big|_{\eta^+=\varepsilon f(\theta/\varepsilon^\alpha)} = \sigma_m\left(\partial_\eta u_\varepsilon - \varepsilon^{1-\alpha}f'(\theta/\varepsilon^\alpha)\partial_\theta u_\varepsilon\right)\big|_{\eta^-=\varepsilon f(\theta/\varepsilon^\alpha)},\\
&\sigma_m\partial_\eta u_\varepsilon|_{\eta=0^+} = \sigma_0\partial_\eta u_\varepsilon|_{\eta=0^-},
\end{aligned}$$

and the difference $w_\varepsilon = u_\varepsilon - u_0$ is the continuous function that satisfies

$$\partial^2_\eta w_\varepsilon + \partial^2_\theta w_\varepsilon = 0, \quad \text{in the three domains,} \tag{84}$$

$$[\sigma\partial_n w_\varepsilon]_{\eta=\varepsilon f(\theta/\varepsilon^\alpha)} = (\sigma_m-\sigma_0)\,n_\varepsilon(\theta/\varepsilon^\alpha)\cdot\begin{pmatrix}\partial_x u_0\\ \partial_y u_0\end{pmatrix}\Big|_{\eta=\varepsilon f(\theta/\varepsilon^\alpha)}, \tag{85}$$

$$[\sigma\partial_n w_\varepsilon]_{\eta=0} = (\sigma_0-\sigma_m)\,n_0\cdot\begin{pmatrix}\partial_x u_0\\ \partial_y u_0\end{pmatrix}\Big|_{\eta=0^+}. \tag{86}$$

Since $\nabla u_0|_{\varepsilon f(./\varepsilon)} \sim \nabla u_0|_{0^+}$, equation (85) shows that at the order $O(\varepsilon)$ the fast and slow variables are uncoupled. The idea of the asymptotics is to introduce a corrector that takes advantage of this uncoupling.

Instead of differentiating between the cases $\alpha < 1$, $\alpha = 1$ and $\alpha > 1$, and instead of performing *ad hoc* rescaling for each case, as we did in [83, 23, 25], we introduce in [85] the parameter $\beta = \min(1,\alpha)$, and we perform the rescaling $1/\varepsilon^\beta$ in the normal direction.

We then introduce the pair $({}^{\alpha}\mathrm{A}, {}^{\alpha}\mathrm{a})$, where ${}^{\alpha}\mathrm{A}$ is a vector field of $\mathbb{R}\times\mathbb{T}$ and ${}^{\alpha}\mathrm{a}$ is a constant vector, defined in the infinite strip $\mathbb{R}\times\mathbb{T}$ by

$$\Delta_{X,Y}\,{}^{\alpha}\mathrm{A} = 0, \text{ in } \mathbb{R}\times\mathbb{T}\setminus(\mathcal{C}_0\cup\mathcal{C}_{\beta;1}), \tag{87a}$$

$$\sigma_0\nabla_{X,Y}\,{}^{\alpha}\mathrm{A}|_{\mathcal{C}^+_{\beta;1}}\cdot n_{\mathcal{C}_{\beta;1}} - \sigma_m\nabla_{X,Y}\,{}^{\alpha}\mathrm{A}|_{\mathcal{C}^-_{\beta;1}}\cdot n_{\mathcal{C}_{\beta;1}} = \frac{1}{\sqrt{1+\varepsilon^{1-\alpha}f'(\theta/\varepsilon^{\alpha-\beta})}}\begin{pmatrix}1\\ -\varepsilon^{1-\alpha}f'(\theta/\varepsilon^{\alpha-\beta})\end{pmatrix}, \tag{87b}$$

$$\sigma_m\nabla_{X,Y}\,{}^{\alpha}\mathrm{A}|_{\mathcal{C}^+_0}\cdot n_{\mathcal{C}_0} - \sigma_1\nabla_{X,Y}\,{}^{\alpha}\mathrm{A}|_{\mathcal{C}^-_0}\cdot n_{\mathcal{C}_0} = -\begin{pmatrix}1\\0\end{pmatrix}, \tag{87c}$$

$${}^{\alpha}\mathrm{A}\to_{X\to-\infty}0,\ {}^{\alpha}\mathrm{A}\to_{X\to+\infty}{}^{\alpha}\mathrm{a}. \tag{87d}$$

It is worth noting that the above convergence are exponentially fast as we show in [23], and the boundary layer corrector u_0^{BL} defined as

$$u_0^{BL}(\eta,\theta) = (\sigma_m-\sigma_0)\,\varepsilon^{\beta}\nabla u_0|_{0^+}\cdot\begin{cases}\left({}^{\alpha}\mathrm{A}(\eta/\varepsilon^{\beta},\theta/\varepsilon^{\beta})-{}^{\alpha}\mathrm{a}\right), \text{ if } \eta>0,\\ {}^{\alpha}\mathrm{A}(\eta/\varepsilon^{\beta},\theta/\varepsilon^{\beta}), \text{ if } \eta<0,\end{cases}$$

adjusts the jumps (85)–(86) at the order ε, but it generates an error on the boundaries $|\eta|=1$ and on the jump of the Dirichlet traces, that are *a priori* of order ε^{β}. Thanks to this corrector, the polarization tensor $\mathcal{M}_{\alpha}$ writes[2]

$$\mathcal{M}_{\alpha} = \varepsilon^{\beta-1}\begin{pmatrix}\sigma_0\,{}^{\alpha}\mathrm{a}_X & \sigma_0\,{}^{\alpha}\mathrm{a}_Y\\ D_X & D_Y\end{pmatrix},$$

with

$$D = (\sigma_m-\sigma_0)\int_{\mathcal{C}_{\beta;1}}\frac{\varepsilon^{1-\alpha}f'(Y/\varepsilon^{\alpha-\beta})}{\sqrt{1+\left(\varepsilon^{1-\alpha}f'(Y^{\alpha-\beta})\right)^2}}{}^{\alpha}\mathrm{A}\,\mathrm{d}Y - \varepsilon^{1-\beta}\int_0^1 f(Y/\varepsilon^{\alpha-\beta})\mathrm{d}Y\,n^{\perp}_{\mathcal{C}_0}. \tag{88}$$

1.2. Main results for rough thin layer (Theorem 3.1 of [85]). Depending on the parameter $\beta=\min(1;\alpha)$, the above corrector still depends on ε. For the three cases $\alpha<1$, $\alpha=1$ and $\alpha>1$, we exhibit the leading part of $({}^{\alpha}\mathrm{A}, {}^{\alpha}\mathrm{a})$, and we provide the corresponding polarization tensor.

1.2.a. *The case* $\alpha<1$. For $\alpha<1$, then $\beta=\alpha$ and the infinite strip has only 1 oscillation of the curve. The boundary layer corrector thus is defined in a domain with thin layer, with thickness $\varepsilon^{1-\alpha}\ll 1$. Using exactly the same analysis as in [83], we prove that ${}^{\alpha}\mathrm{A}\sim\varepsilon^{1-\beta}A_1$, where A_1 is defined by

$$A_1(X,Y) = \begin{cases}0, & \text{if } X<0,\\ \dfrac{1}{\sigma_m}\begin{pmatrix}f\\0\end{pmatrix}, & \text{if } X>0.\end{cases}$$

from which we infer that

$${}^{\alpha}\mathrm{a} = \varepsilon^{1-\beta}\frac{1}{\sigma_m}\begin{pmatrix}\int_{\mathbb{T}}f(Y)\mathrm{d}Y\\0\end{pmatrix}+O(\varepsilon^{1-\beta}),\quad\text{and}\quad D=\varepsilon^{1-\beta}\begin{pmatrix}0\\\int_{\mathbb{T}}f(Y)\mathrm{d}Y\end{pmatrix}+O(\varepsilon^{1-\beta}).$$

Denote by $\overline{f}=\int_{\mathbb{T}}f(Y)\mathrm{d}Y$ and let u^1 be the solution to

$$\Delta u^1 = 0, \text{ in } \mathcal{D}^1\cup\mathcal{D}^0,$$
$$u^1|_{\partial\mathcal{D}} = 0,$$

with the following transmission conditions:

$$\sigma_0\partial_{\boldsymbol{n}}u^1|_{\Gamma^+}-\sigma_1\partial_{\boldsymbol{n}}u^1|_{\Gamma^-} = (\sigma_m-\sigma_0)\overline{f}\Delta_{\Gamma}u^0_{\Gamma},$$
$$u^1|_{\Gamma^+}-u^1|_{\Gamma^-} = \frac{\sigma_m-\sigma_0}{\sigma_m}\overline{f}\partial_{\boldsymbol{n}}u^0|_{\Gamma^+}.$$

According to [85], far from the layer we have

$$u^{\varepsilon}-u^0 = \varepsilon u^1+o(\varepsilon),$$

[2]Note that $D_X=\sigma_0\,{}^{\alpha}\mathrm{a}_Y$.

which means that the mean thickness of the layer provides a first order approximation of u^ε, as previously described in [83]. In addition, the polarization tensor writes:

$$\mathcal{M}_\alpha = \overline{f}\begin{pmatrix} \dfrac{\sigma_0}{\sigma_m} & 0 \\ 0 & 1 \end{pmatrix}, \tag{89}$$

as obtained by Beretta *et al.* [10, 11] in the case of constant thickness ($\alpha = 0$).

The fact that the rough thin layer can be identified, as first approximation, as a flat thin layer whose thickness equals the mean thickness of the rough layer is a specific property of weakly rough thin layer. As we see in the two next paragraphs, for $\alpha \geq 1$ this approximation is no more accurate.

1.2.b. *The case* $\alpha = 1$. For $\alpha = 1$, the boundary layer corrector does not depend on ε, since the thickness and the period of the oscillations are of the same order. The couple $({}^\alpha\mathrm{A}, {}^\alpha\mathrm{a})$ defined by (87) is thus ε–independent. We prove in [23, 84] that $u_\varepsilon = u_0 + \varepsilon u_1 + o(\varepsilon)$ where u^1 is defined by

$$\begin{aligned}
&\Delta u^1 = 0, \ \text{ in } \mathcal{D}^0 \cup \mathcal{D}^1, \quad u^1|_{\partial\Omega} = 0, \ \text{ on } \partial\mathcal{D} \\
&\sigma_0 \partial_n u^1|_{\Gamma^+} = \sigma_1 \partial_n u^1|_{\Gamma^-} + D \cdot \partial_t \begin{pmatrix} \partial_{\boldsymbol{n}} u^0|_{\Gamma+} \\ \partial_t u^0|_{\Gamma^+} \end{pmatrix}, \\
&u^1|_{\Gamma^+} = u^1|_{\Gamma^-} + {}^\alpha\mathrm{a} \cdot \begin{pmatrix} \partial_n u^0|_{\Gamma+} \\ \partial_t u^0|_{\Gamma^+} \end{pmatrix},
\end{aligned}$$

and the polarization tensor is the plain matrix given by

$$\mathcal{M}_\alpha = \begin{pmatrix} \sigma_0 {}^\alpha\mathrm{a}_X & \sigma_0 {}^\alpha\mathrm{a}_Y \\ D_X & D_Y \end{pmatrix}. \tag{90}$$

1.2.c. *The case* $\alpha > 1$. For $\alpha > 1$, then $\beta = 1$ and the corrector $({}^\alpha\mathrm{A}, {}^\alpha\mathrm{a})$ depends on ε since the curve $\mathcal{C}_{\beta;1}$ is oscillating, with a period of the order $\varepsilon^{\alpha-1}$. In [85] we use a two-scale analysis to exhibit the limit of $({}^\alpha\mathrm{A}, {}^\alpha\mathrm{a})$ for ε going to zero.

Let $\sigma^\sharp$ be the function defined by

$$\forall (X,\tau) \in \mathbb{R}\times\mathbb{T}, \quad \sigma^\sharp(X,\tau) = \begin{cases} \sigma_0, & \text{in } \{(X,\tau), \quad \tau \in \mathbb{T},\, X > f(\tau)\}, \\ \sigma_m, & \text{in } \{(X,\tau), \quad \tau \in \mathbb{T},\, 0 < x < f(\tau)\}, \\ \sigma_1, & \text{in } \{(X,\tau), \quad \tau \in \mathbb{T},\, X < 0\}, \end{cases}$$

and define for any $X \in \mathbb{R}$

$$\overline{\sigma}^\sharp(X) = \int_{\mathbb{T}} \sigma^\sharp(X,\tau)\,\mathrm{d}\tau, \quad \text{and } q \text{ the cumulative distribution function:} \quad q(X) = \int_{\mathbb{T}} \mathbb{1}_{\{0<X<f(\tau)\}}\mathrm{d}\tau.$$

We prove that $({}^\alpha\mathrm{A}, {}^\alpha\mathrm{a})$ two-scale converges towards $(\mathfrak{A}^0, \mathfrak{a}^0)$ defined by

$$\begin{aligned}
&\nabla\cdot\left(\begin{pmatrix} \overline{\sigma}^\sharp & 0 \\ 0 & 1/(\int_{\mathbb{T}} 1/\sigma^\sharp \mathrm{d}\tau) \end{pmatrix} \nabla\mathfrak{A}^0\right) = \nabla q, \\
&\mathfrak{A}^0 \to_{X\to-\infty} 0, \quad \mathfrak{A}^0 \to_{X\to+\infty} \mathfrak{a}^0.
\end{aligned}$$

This corrector has to be related with the well-known homogenization formula for laminate structures: in the laminate alignment (here the X-direction), the mean of the conductivities appears, while in the transverse direction (the Y-direction in our case) the harmonic mean holds.

We prove that D_X converges to zero and that D_Y converges to D^∞ defined as

$$D^\infty = \int_0^{+\infty} (\sigma_m - \sigma_0)\frac{q(X)(1-q(X))}{\sigma_0 q(X) + \sigma_m(1-q(X))}\mathrm{d}X - \int_{\mathbb{T}} f(Y)\mathrm{d}Y. \tag{91}$$

such that the polarization tensor equals

$$\mathcal{M}_\alpha = \begin{pmatrix} -\int_0^{+\infty} q(s)(\sigma_0/\overline{\sigma}^\sharp(s))\mathrm{d}s & 0 \\ 0 & D^\infty \end{pmatrix}. \tag{92}$$

1.3. Numerical simulations for $\alpha > 1$. We provide in [24, 25] numerical simulations that corroborate the theoretical results of convergence for $\alpha \geq 1$. In particular we illustrate that the approximation of the rough layer by a thin layer of thickness equal to the mean thickness of the roughness is no accurate for $\alpha geq 1$. Numerical results for weakly rough thin layer are presented in [83], and for the sake of conciseness we choose to omit them in this manuscrpit. The numerics have been obtained using the mesh generator *Gmsh* [44] and the finite element library *Getfem++* [90].

The computational domain $\mathcal{D}$ is delimited by the circles of radius 2 and of radius 0.2 centered in 0, while $\mathcal{D}^1$ is the intersection of $\mathcal{D}$ with the concentric disk of radius 1. The rough layer is then described thanks to the function $f(y) = 1 + \frac{1}{2}\sin(y)$ and we choose $\alpha = 3/2$. One period of the domain is shown Figure 3(a). The Dirichlet boundary data is identically 1 on the outer circle and 0 on the inner circle. The conductivities σ_0, σ_1 and σ_m are respectively equal to 1, 1 and 0.1. The computed coefficients for quantifying the roughness are $r_1 = 5.87$ and $r_2 = 0.413$ (three significant digits are kept).

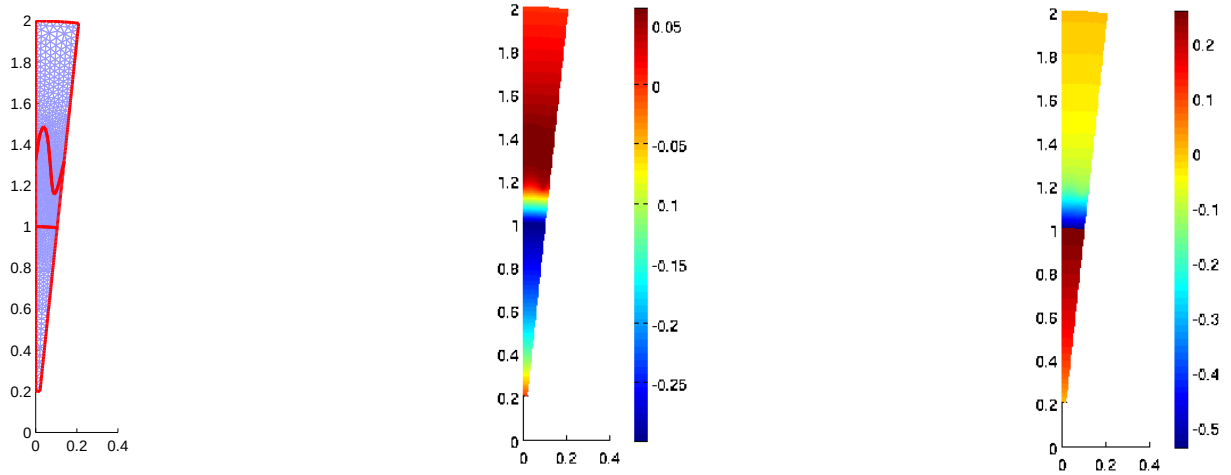

(a) Mesh (b) Error order 0. (c) Error order 1.

FIGURE 3. Representation of one period of the domain and the errors $u_\varepsilon - u_0$ in Figure 3(b) and $u_0 + \varepsilon u_1$ in Figure 3(c), with $\varepsilon = 2\pi/60$.

We denote by $\tilde{u}_1$ the correction, which only takes the mean effect of the layer into account. The numerical convergence rates for the H^1– and the L^2–norms in $\mathcal{D}^1$ of the three following errors $u_\varepsilon - u_0$, $u_\varepsilon - u_0 - \varepsilon u_1$ and $u_\varepsilon - u_0 - \varepsilon\tilde{u_1}$ as ε goes to zero are given Figure 4 for $\alpha = 3/2$. The numerical convergence rates are close to 1 for $u_\varepsilon - u$ and for $u_\varepsilon - (u + \varepsilon^\beta \tilde{u}_1)$, whereas the convergence rate is close to 2 for $u_\varepsilon - (u + \varepsilon u_1)$. Figure 4(b) demonstrates that the convergence rate decreases dramatically for $\alpha = 1$. This is in accordance with the theory, since the polarization tensor for $\alpha = 1$ is a plain matrix, while for $\alpha > 1$ it is diagonal.

Therefore the results of this section provide explicit characterizations of the polarization tensor of the steady-state potential for any rough thin layer, in the perdiodic case.

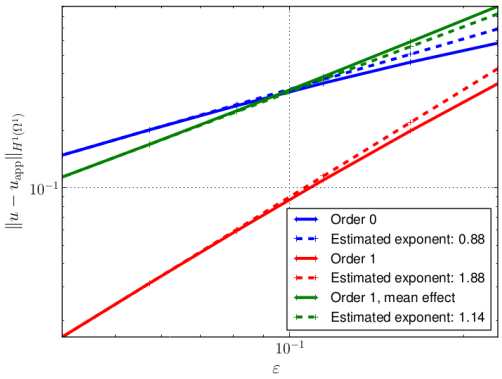

(a) H^1–norm of the error for $\alpha = 3/2$.

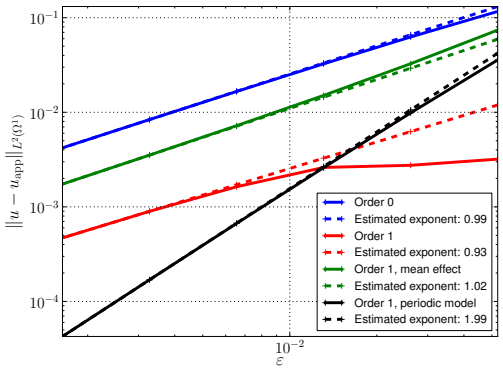

(b) L^2–norm of the error for $\alpha = 1$.

FIGURE 4. Norm of the error in the cytoplasm vs ε for approximate solutions. We choose $\alpha = 3/2$ in Figure 4(a). For $\beta = 1$, the perodic model of Subsection 1.2.b has to be used instead of equation (92).

2. Eddy current model in domain with corner singularity

This section is devoted to the eddy current problem in a bidimensional setting where the conducting medium is non-magnetic and has a corner singularity.

For smooth conducting domain, it is well known that impedance boundary condition such as Leontovitch condition imposed on the interface between the dielectric and the conducting materials provides an accurate description of the magnetic potential [65]. However in the presence of corner singularity, this approximation fails. The aim of this section is to propose a rigorous asymptotic method to tackle this difficulty in the case of the scalar PDE satisfied by the magnetic potential.

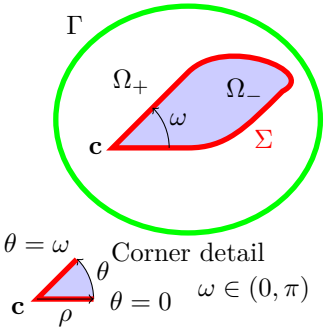

For $\delta > 0$, let $\mathcal{A}_\delta$ be the magnetic potential, solution to

$$\text{(93)}\qquad \begin{cases} -\Delta \mathcal{A}_\delta^+ = \mu_0 J \text{ in } \Omega_+, & \\ -\Delta \mathcal{A}_\delta^- + \dfrac{2\mathrm{i}}{\delta^2}\mathcal{A}_\delta^- = 0 \text{ in } \Omega_-, & [\mathcal{A}_\delta]_\Sigma = 0, \text{ on } \Sigma, \\ \mathcal{A}_\delta^+ = 0 \text{ on } \Gamma, & [\partial_n \mathcal{A}_\delta]_\Sigma = 0, \text{ on } \Sigma. \end{cases}$$

Subsection 2.1 is devoted to provide the corner asymptotics for $\mathcal{A}_\delta$ obtained in [31] for δ fix, as the distance to the corner r goes to zero [59]. We show the heuristics for the construction of the singularities and we present the quasi-dual method to extract the singular coefficients. We then provide in Subsection 2.2 the heuristics of the expansion of $\mathcal{A}_\delta$ as δ goes to zero.

2.1. Corner asymptotics for the eddy current model. In this subsection, we assume that δ is a fix parameter, which does not tend to zero, and for the sake of clarity we avoid the index δ on the magnetic potential. To simplify the calulations, we set in [31]:

$$\zeta = \sqrt{2}/(2\delta)$$

such that for J compactly supported in Ω_+, the magnetic potential $\mathcal{A} \in H_0^1(\Omega)$ satisfies:

$$\Delta \mathcal{A}^- + 4\mathrm{i}\zeta^2 \mathcal{A}^- \mathbb{1}_{\Omega_-} = \mu_0 J \text{ in } \Omega.$$

For J is smooth enough, standard elliptic regularity of the Laplace operator implies that $\mathcal{A}$ belongs to $H^2(\Omega)$, and even to $H^{\frac{5}{2}-\varepsilon}(\Omega)$ for any $\varepsilon > 0$. In particular, $\mathcal{A}$ belongs to $\mathcal{C}^1(\overline{\Omega})$ thanks to Sobolev imbeddings in two dimensions. However, due to the corner the magnetic potential $\mathcal{A}$ does not belong to $\mathcal{C}^2(\overline{\Omega})$, but it possesses a corner asymptotic expansion as the distance r to the corner $\mathbf{c}$ goes to zero.

In contrast with problems involving only *homogeneous* operators, problem (93) involves the lower order term $2\mathrm{i}/\delta^2$ in Ω_-. As a consequence, according to the seminal paper of Kondratiev [59], the singularities are not homogeneous functions, but infinite sums of quasi-homogeneous terms of the general form

$$r^{\lambda+\ell} \log^n r \, \Phi(\theta), \quad \lambda \in \mathbb{C},\ \ell \in \mathrm{N},\ n \in \mathrm{N},$$

in polar coordinates (r, θ) centered at $\mathbf{c}$. In the present situation, the *leading exponents* λ can be made precise: they are determined by the principal part of the operator at $\mathbf{c}$, which is nothing but the Laplacian $-\Delta$ at the interior point $\mathbf{c}$. Thus, the leading exponents are *integers* $k \in \mathrm{N}$ corresponding to leading singularities in the form of *harmonic polynomials*, written in polar coordinates as

$$\text{(94)}\qquad r^k \cos(k\theta - p\pi/2), \quad k \in \mathrm{N},\ p \in \{0, 1\},$$

— only $p = 0$ is involved when $k = 0$. Therefore $\mathcal{A}$ can be expanded close to the corner as

$$\text{(95)}\qquad \mathcal{A}(r,\theta) \underset{r\to 0}{\sim} \Lambda^{0,0}\mathfrak{S}^{0,0}(r,\theta) + \sum_{k\geq 1}\sum_{p\in\{0,1\}} \Lambda^{k,p}\mathfrak{S}^{k,p}(r,\theta),$$

where the terms $\mathfrak{S}^{k,p}$ are the so-called *primal singular functions*, which belong to the formal kernel of the considered operator in $\mathbb{R}^2$, and the numbers $\Lambda^{k,p}$ are the *singular coefficients*.

The derivation of the corner asymptotics consist then in making precise the primal singularities $\mathfrak{S}^{k,p}$ and the singular coefficients $\Lambda^{k,p}$. Since the calculations of the singular coefficients involve the dual singularity, *i.e* the singular functions which do not belong to H^1 in any neighborhood of the corner, it is necessary to derive these singular functions too.

2.1.a. *Heuristics of the construction of the singularities.* The positive parameter ζ being chosen, we denote by $\mathscr{L}_\zeta$ the operator defined on $\mathbb{R}^2$ by

$$\mathscr{L}_\zeta(u) = \begin{cases} -\Delta u, & \text{in } \mathcal{S}_+, \\ -\Delta u + 4\mathrm{i}\zeta^2 u, & \text{in } \mathcal{S}_-. \end{cases} \tag{96}$$

acting on functions u such that $\partial_\theta^q u_-|_{\mathcal{G}} = \partial_\theta^q u_+|_{\mathcal{G}}$ for $q = 0, 1$. As described above, the asymptotics of $\mathcal{A}$ near the corner involve the *singularities* of the operator $\mathscr{L}_\zeta$, which, by convention, are formal solutions $\mathfrak{U}$ to the equation $\mathscr{L}_\zeta(\mathfrak{U}) = 0$. It is therefore crucial to make explicit these singularities.

Note that the operator $\mathscr{L}_\zeta$ is the sum of its leading part $\mathscr{L}_0$ which is the Laplacian $-\Delta$ in $\mathbb{R}^2$, and of the zeroth order operator $4\mathrm{i}\delta^2\mathscr{L}_1$ where $\mathscr{L}_1$ is the restriction to $\mathcal{S}_-$. According to the general principles of Kondratiev's paper [59], the singularities $\mathfrak{U}$ of $\mathscr{L}_\zeta = \mathscr{L}_0 + 4\mathrm{i}\zeta^2\mathscr{L}_1$ can be described as formal sums

$$\mathfrak{U} = \sum_j (\mathrm{i}\zeta^2)^j \mathfrak{u}_j, \tag{97}$$

where each term $\mathfrak{u}_j$ is derived through an inductive process by solving recursively

$$\mathscr{L}_0\mathfrak{u}_0 = 0, \quad \mathscr{L}_0\mathfrak{u}_1 = -4\mathscr{L}_1\mathfrak{u}_0, \quad \dots, \quad \mathscr{L}_0\mathfrak{u}_j = -4\mathscr{L}_1\mathfrak{u}_{j-1}, \tag{98}$$

in spaces of quasi-homogeneous functions S^λ defined for $\lambda \in \mathbb{C}$ by

$$\mathsf{S}^\lambda = \mathsf{Span}\left\{ r^\lambda \log^q r\, \Phi(\theta), \quad q \in \mathrm{N}, \quad \Phi \in \mathcal{C}^1(\mathbb{T}),\ \Phi^\pm \in \mathcal{C}^\infty(\overline{\mathbb{T}}_\pm) \right\}. \tag{99}$$

2.1.b. *Principles of the construction of the primal singularities.* For $R > 0$, let $\mathcal{B}$ be the ball of radius R centered at the corner. The primal singular functions start with (quasi-homogeneous) terms $\mathfrak{u}_0 \in H^1(\mathcal{B})$ satisfying $\Delta\mathfrak{u}_0 = 0$. Therefore, $\mathfrak{u}_0$ is a homogeneous harmonic polynomial. We are looking for a basis for primal singular functions, so we choose $\mathfrak{u}_0 = \mathfrak{s}^{k,p}$ (for $(k,p) = (0,0)$ and for any $(k,p) \in \mathrm{N}^* \times \{0,1\}$) where

$$\mathfrak{s}^{k,p}(r,\theta) = \begin{cases} 1, & \text{if } \ k = 0 \ \text{ and } \ p = 0, \\ r^k \cos(k\theta - p\pi/2), & \text{if } \ k \geq 1 \ \text{ and } \ p = 0, 1. \end{cases} \tag{100}$$

In order to have coherent notation, we set $\mathfrak{s}_0^{k,p} := \mathfrak{s}^{k,p}$. Each $\mathfrak{s}_0^{k,p}$ belongs to S^k and is the leading part of the singular function $\mathfrak{S}^{k,p}$ defined by

$$\mathfrak{S}^{k,p}(r,\theta) = \sum_{j\geq 0} (\mathrm{i}\zeta^2)^j \mathfrak{s}_j^{k,p}(r,\theta). \tag{101}$$

For $j \geq 1$, the terms $\mathfrak{s}_j^{k,p}$ in the previous series are the *shadow terms of order* j. According to the sequence of problems (98), the function $\mathfrak{s}_j^{k,p}$ is searched in S^{k+2j} as a particular solution to the following problem:

$$\begin{cases} \Delta\mathfrak{s}_j^{k,p\,+} = 0, & \text{in } \mathcal{S}_+, \\ \Delta\mathfrak{s}_j^{k,p\,-} = 4\mathfrak{s}_{j-1}^{k,p\,-}, & \text{in } \mathcal{S}_-. \end{cases} \tag{102}$$

Belonging to S^{k+2j} includes the following transmission conditions on $\mathcal{G}$:

$$\begin{cases} \mathfrak{s}_j^{k,p\,+}|_{\mathcal{G}} = \mathfrak{s}_j^{k,p\,-}|_{\mathcal{G}}, \\ \partial_\theta\mathfrak{s}_j^{k,p\,+}|_{\mathcal{G}} = \partial_\theta\mathfrak{s}_j^{k,p\,-}|_{\mathcal{G}}. \end{cases} \tag{103}$$

Lemma 2.1. *Let $(k,p) = (0,0)$ or $(k,p) \in \mathrm{N}^* \times \{0,1\}$. Let $\mathfrak{s}_0^{k,p}$ be defined as*

$$\mathfrak{s}_0^{k,p}(r,\theta) = \begin{cases} 1, & \textit{if } \ k = 0 \ \textit{ and } \ p = 0, \\ r^k \cos(k\theta - p\pi/2), & \textit{if } \ k \geq 1 \ \textit{ and } \ p = 0, 1. \end{cases}$$

Then, for any $j \geq 1$, there exists $\mathfrak{s}_j^{k,p} \in \mathsf{S}^{k+2j}$ satisfying (102)–(103). *Moreover* $\deg \mathfrak{s}_j^{k,p} \leq j$. *When $p = 0$, we choose $\mathfrak{s}_j^{k,p}$ as an even function of θ and when $p = 1$, $\mathfrak{s}_j^{k,p}$ is chosen to be odd.*

These definitions being set, we can write the corner expansion of the solution to problem (93) as

$$\mathcal{A}(r,\theta) \underset{r\to 0}{\sim} \Lambda^{0,0}\mathfrak{S}^{0,0}(r,\theta) + \sum_{k\geq 1}\sum_{p\in\{0,1\}} \Lambda^{k,p}\mathfrak{S}^{k,p}(r,\theta). \tag{104}$$

For any $(k,p) \in \mathrm{N}^* \times \{0,1\}$ or $(k,p) = (0,0)$, the singular function $\mathfrak{S}^{k,p}$ writes as the formal serie

$$\mathfrak{S}^{k,p}(r,\theta) = r^k \sum_{j\geq 0} (\mathrm{i}\zeta^2)^j\, r^{2j} \sum_{n=0}^{j} \log^n r\, \Phi_{j,n}^{k,p}(\theta), \tag{105}$$

where the angular functions $\Phi_{j,n}^{k,p}$ are $\mathcal{C}^1$ functions of θ globally in $\mathbb{R}/(2\pi\mathbb{Z})$ (and piecewise analytic).

2.1.c. *Principles of the construction of the dual singularities.* Setting $\mathfrak{k}_0^{k,p} = \mathfrak{k}^{k,p}$, the dual singularities of $\mathscr{L}_\zeta$ are given by the series

$$\mathfrak{K}^{k,p}(r,\theta) = \sum_{j\geq 0} (\mathrm{i}\zeta^2)^j \mathfrak{k}_j^{k,p}(r,\theta), \tag{106}$$

where, for $j \geq 1$, the shadow terms $\mathfrak{k}_j^{k,p}$ are solutions in S^{-k+2j} to

$$\begin{cases} \Delta \mathfrak{k}_j^{k,p\,+} = 0, & \text{in } \mathcal{S}_+\,, \\ \Delta \mathfrak{k}_j^{k,p\,-} = 4\mathfrak{k}_{j-1}^{k,p\,-}, & \text{in } \mathcal{S}_-\,, \end{cases} \tag{107}$$

with the same transmission conditions as (103). We have the following lemma:

Lemma 2.2. *Let $(k,p) = (0,0)$ or $(k,p) \in \mathrm{N}^* \times \{0,1\}$. Let $\mathfrak{k}_0^{k,p}$ be defined as*

$$\mathfrak{k}_0^{k,p}(r,\theta) = \begin{cases} -\dfrac{1}{2\pi}\,\log r, & \text{if } \ k=0,\ p=0, \\ \dfrac{1}{2k\pi}\, r^{-k}\cos(k\theta - p\pi/2), & \text{if } \ k\geq 1,\ p=0,1\,. \end{cases}$$

Then, for any $j \geq 1$, there exists $\mathfrak{k}_j^{k,p} \in \mathsf{S}^{-k+2j}$ satisfying (107). *Moreover, if j is odd, or if j is even and $2j < k$, then $\deg \mathfrak{k}_j^{k,p} \leq j$. Otherwise (i.e. if j is even and $2j \geq k$) then $\deg \mathfrak{k}_j^{k,p} \leq j+1$. When $p = 0$, we choose $\mathfrak{k}_j^{k,p}$ as an even function of θ and when $p = 1$, $\mathfrak{k}_j^{k,p}$ is chosen to be odd.*

From which we infer that the dual singular function $\mathfrak{K}^{k,p}$ writes as formal series

$$\mathfrak{K}^{k,p}(r,\theta) = \begin{cases} r^{-k} \displaystyle\sum_{j\geq 0} (\mathrm{i}\zeta^2)^j\, r^{2j} \sum_{n=0}^{j} \log^n r\, \Psi_{j,n}^{k,p}(\theta) & (k \text{ odd}), \\ r^{-k}\Big(\displaystyle\sum_{0\leq j<k/2} (\mathrm{i}\zeta^2)^j\, r^{2j} \sum_{n=0}^{j} \log^n r\, \Psi_{j,n}^{k,p}(\theta) + \sum_{j\geq k/2} (\mathrm{i}\zeta^2)^j\, r^{2j} \sum_{n=0}^{j+1} \log^n r\, \Psi_{j,n}^{k,p}(\theta)\Big) & (k \text{ even}). \end{cases} \tag{108}$$

where the angular functions $\Psi_{j,n}^{k,p}$ are $\mathcal{C}^1$ functions of θ globally in $\mathbb{R}/(2\pi\mathbb{Z})$ (and piecewise analytic).

2.1.d. *Extraction of singular coefficients by the method of quasi-dual functions.* In order to extract the singular coefficients we define the anti-symmetric bilinear form $\mathcal{J}_R$ over a circle of radius $R > 0$ by

$$\mathcal{J}_R(K,A) := \int_{r=R} (K\partial_r A - A\partial_r K)\ R\mathrm{d}\theta. \tag{109}$$

For the Laplace operator, it is usual to use the exact dual singularity to obtain straighforwardly the singular coefficients, thanks to a nice property of orthogonality of the dual and primal singular functions for the Laplacian. This method cannot be used here since first the singular functions are not orthogonal, and second they are described as infinite series, which prevents the use of the full dual singularity for numerical purpose.

Instead, we use the *quasi-dual* functions $\mathfrak{K}_m^{k,p}$, which are the truncated series of (106):

$$\mathfrak{K}_m^{k,p}(r,\theta) := \sum_{j=0}^{m} (\mathrm{i}\zeta^2)^j \mathfrak{k}_j^{k,p}(r,\theta). \tag{110}$$

Here, m is a non–negative integer, which is the order of the quasi-dual function. By construction

$$\mathscr{L}_\zeta \mathfrak{K}_m^{k,p} = 4\mathrm{i}\zeta^2 (\mathrm{i}\zeta^2)^m \mathfrak{k}_m^{k,p}\, \mathbb{1}_{\mathcal{S}_-}, \tag{111}$$

which is not zero, but smaller and smaller as $r \to 0$ when m is increased. The extraction of coefficients $\Lambda^{k,p}$ in expansion (104) is performed through the evaluation of quantities

$$\mathcal{J}_R(\mathfrak{K}_m^{k,p}, \mathcal{A}), \quad k = 0, 1, 2, \ldots$$

and corresponding $p \in \{0, 1\}$, for suitable values of $m \in \{0, 1, \ldots\}$. The quasi-dual function method was introduced in [30] for straight edges and developed in [99] for circular edges and homogeneous operators with constant coefficients. The expansions considered there do not contain any logarithmic terms. In [31], we revisit this theory in our framework where, on the contrary, we have an accumulation of logarithmic terms. The main result follows.

THEOREM 2.3. *Let $\mathcal{A}$ be the solution to problem* (93)*, under the assumptions of the introduction. Let $k \in \mathrm{N}$ and $p \in \{0, 1\}$ ($p = 0$ if $k = 0$). Let m such that $2m + 2 > k$. For the extraction quantity $\mathcal{J}_R(\mathfrak{K}_m^{k,p}, \mathcal{A})$ defined through* (109) *and* (110)*, there exist coefficients $\mathcal{J}^{k,p;k',p'}$ independent of R and $\mathcal{A}$ such that*

$$\mathcal{J}_R(\mathfrak{K}_m^{k,p}, \mathcal{A}) \underset{R\to 0}{=} \Lambda^{k,p} + \sum_{\ell=1}^{[k/2]} \mathcal{J}^{k,p\,;\,k-2\ell,p} \Lambda^{k-2\ell,p} + \mathcal{O}(R^{-k} R_0^{2m+2} \log R)\,, \tag{112}$$

where R_0 is defined by

$$\boxed{R_0 = \zeta R\,(1 + \sqrt{|\log R|})} \tag{113}$$

If $p = 1$, the remainder is improved to $\mathcal{O}(R^{1-k} R_0^{2m+2} \log R)$. The extra term $\log R$ disappears if k is odd.

REMARK 2.4. *The collection of equations* (112) *for $p \in \{0, 1\}$, and k belonging to $\{0, 2, \ldots, 2L\}$ or to $\{1, 3, \ldots, 2L + 1\}$, with $L \in \mathrm{N}$, forms a lower triangular system with invertible diagonal.*

PROPOSITION 2.5. *Let $k \in \mathrm{N} \setminus \{0, 1\}$ and $p \in \{0, 1\}$. For any $\ell \in 1, \ldots, [k/2]$, the coefficients $\mathcal{J}^{k,p\,;k-2\ell,p}$ introduced in* (112) *are given recursively by*

$$\mathcal{J}^{k,p\,;\,k-2\ell,p} = (\mathrm{i}\zeta^2)^\ell \sum_{j=0}^{\ell} \int_0^{2\pi} \Psi_{j,0}^{k,p}(\theta) \left[2(k-2j)\Phi_{\ell-j,0}^{k-2\ell,p}(\theta) + \Phi_{\ell-j,1}^{k-2\ell,p}(\theta)\right] - \Psi_{j,1}^{k,p}(\theta)\Phi_{\ell-j,0}^{k-2\ell,p}(\theta)\, d\theta, \tag{114}$$

with the convention that $\Phi_{0,1}^{k-2\ell,p} = 0$ and $\Psi_{0,1}^{k,p} = 0$.

2.1.e. *Numerical validation of the corner expansion.* In Figure 5, we perform a qualitative description of the isovalues of $\mathfrak{A}$ close to the corner comparing the finite element solution and, successively,

- expansion (104) restricted to a composite order 1, *i.e.*

$$\mathcal{J}_{R_{\mathrm{small}}}(\mathfrak{K}_1^{0,0}, \mathcal{A}) + \mathcal{J}_{R_{\mathrm{small}}}(\mathfrak{K}_1^{1,0}, \mathcal{A})\mathfrak{s}_0^{1,0},$$

- expansion (104) restricted to a composite order 2, *i.e.*

$$\mathcal{J}_{R_{\mathrm{small}}}(\mathfrak{K}_1^{0,0}, \mathcal{A})(1 + \mathrm{i}\zeta^2\mathfrak{s}_1^{0,0}) + \mathcal{J}_{R_{\mathrm{small}}}(\mathfrak{K}_1^{1,0}, \mathcal{A})\mathfrak{s}_0^{1,0} + \left(\mathcal{J}_{R_{\mathrm{small}}}(\mathfrak{K}_1^{2,0}, \mathcal{A}) - \mathcal{J}^{2,0;0,0}\mathcal{J}_{R_{\mathrm{small}}}(\mathfrak{K}_1^{0,0}, \mathcal{A})\right)\mathfrak{s}_0^{2,0},$$

- expansion (104) restricted to a composite order 3, *i.e.* adding to the expression above the term

$$\left(\mathcal{J}_{R_{\mathrm{small}}}(\mathfrak{K}_1^{3,0}, \mathcal{A}) - \mathcal{J}^{3,0;1,0}\mathcal{J}_{R_{\mathrm{small}}}(\mathfrak{K}_1^{1,0}, \mathcal{A})\right)\mathfrak{s}_0^{3,0},$$

and replacing $\mathfrak{s}_0^{1,0}$ by $\mathfrak{s}_0^{1,0} + \mathrm{i}\zeta^2\mathfrak{s}_1^{1,0}$. Computing integrals, we obtain

$$\mathcal{J}^{3,0;1,0} \approx \mathrm{i}\zeta^2 1.522117 \cdot 10^{-9}\ .$$

The reference value for $\mathcal{J}_{R_{\mathrm{small}}}(\mathfrak{K}_1^{3,0}, \mathcal{A})$ is $(93037.6253 - \mathrm{i}\,154720.669)$.

For the composite order 1, only the constant and linear terms with respect to r are collected in the Kondratiev–type expansion. For the composite order 2, the terms which behave as r^2 and $r^2 \log r$ are added. Adding then the terms which behave as r^3 and $r^3 \log r$ leads to the composite order 3.

On both real and imaginary parts, we observe in Figure 5 as expected that the increase of the order enables to increase the accuracy.

2.2. Heuristics of the asymptotics for the high conductivity, in a domain with corner singularity. Now we go back to the initial problem (93) with the parameter δ which tends to 0. This subsection is devoted to the formal derivation of the first order approximation of $\mathcal{A}_\delta$ for small δ. The principle of these asymptotics consist of a localization of the effect of the singularity thanks to a truncature function, which vanishes at a corner distance smaller than δ and which equals 1 near 2δ.

Therefore, far from the corner, $\mathcal{A}_\delta$ is approached as in the smooth case, while near the corner we perform a rescaling in $1/\delta$ which makes appear a bidimensional profile problem, in a sectorial domain. In the smooth case, the construction of the asymptotics can be done step by step [79], however in the case of corner, it is necessary to determine *a priori* the desired order of the expansion, since corner asymptotics will be involved in the expansion, and will be mixed to the δ–expansion.

In [17], we provide the first order terms of the expansion. Denote by $\mathcal{A}_0$ the magnetic potential for the perfect conducting case:

$$\begin{cases} -\Delta \mathcal{A}_0^+ = \mu_0 J \text{ in } \Omega_+, \\ \quad \mathcal{A}_0^+ = 0 \text{ on } \Sigma, \qquad \mathcal{A}_0^- = 0, \text{ in } \Omega_-. \\ \quad \mathcal{A}_0^+ = 0 \text{ on } \Gamma, \end{cases}$$

Let φ be a radial truncature function, that vanishes near the corner, then, far from the corner, $\mathcal{A}_\delta$ is approached by

$$\mathcal{A}_\delta = \varphi(\cdot/\delta)\mathcal{A}_0 + r_\delta^0.$$

The function r_δ^0 is then solution to a problem whose source term is localized near the corner. Thanks to the Kondratiev's asymptotics of $\mathcal{A}_0$ in singular function near the corner, we get

$$\mathcal{A}_0^+ \sim_{\rho\to 0} a_1 \rho^\alpha \sin(\alpha(\theta-\omega)), \quad \text{with} \quad \alpha = \pi/(2\pi-\omega),$$

which makes it possible to exhibit the profile V_α defined in $\mathbb{R}^2$ by:

$$\begin{aligned} &-\Delta_X V_\alpha = [\Delta_X;\varphi]\left(R^\alpha \sin(\alpha(\theta-\omega))\right), \text{ in } S_+, \\ &-\Delta_X V_\alpha + 2\mathrm{i} V_\alpha = 0, \text{ in } S_-, \\ &[V_\alpha]_{\mathcal{G}} = 0, \quad \left[\frac{1}{R}\partial_\theta V_\alpha\right]_{\mathcal{G}} = \alpha\varphi R^{\alpha-1}, \\ &V_\alpha \to_{|X|\to+\infty} 0, \end{aligned}$$

and then $\mathcal{A}_\delta$ writes

$$\mathcal{A}_\delta = \varphi\left(\frac{\cdot}{\delta}\right)\mathcal{A}_0 + (1-\varphi)a_1\delta^\alpha V_\alpha\left(\frac{\cdot}{\delta}\right) + r_\alpha^\delta.$$

According to the expansion, the surface impedance Z_δ close to the corner can be approximated by:

$$Z_\delta = Z_s \frac{1+\mathrm{i}}{\delta}\frac{\mathcal{A}_\delta}{\partial_n \mathcal{A}_\delta} \underset{\rho\to 0}{\simeq} Z_s(1+\mathrm{i})\frac{V_\alpha(\cdot/\delta)}{(\partial_n V_\alpha)(\cdot/\delta)}, \tag{115}$$

therefore for any σ and f such that δ is small enough, the function $Z_\delta(\delta\cdot)/|Z_s|$ behaves close to zero as $\sqrt{2}\mathrm{i}V_\alpha/(\partial_n V_\alpha)$. Figure 6 where the "impedance" from the profile function is compared to the real impedance for two values of δ, where f and σ are different.

It is worth noting that this asymptotics results are preliminary and they have to be rigorously stated, and the order of accuracy at any order should be proven in forthcoming works, however from the point of view of the engineering applications, these preliminary results provide nice tools to tackle address the eddy current problem in domain with corners. In particular, one important feature of this work is the justification that Leontovitch type conditions is not relevant for domains with singular geometry. According to our results, near the corner, it is necessary to compute the profile term V_α which satisfies a PDE problem set in the whole plan.

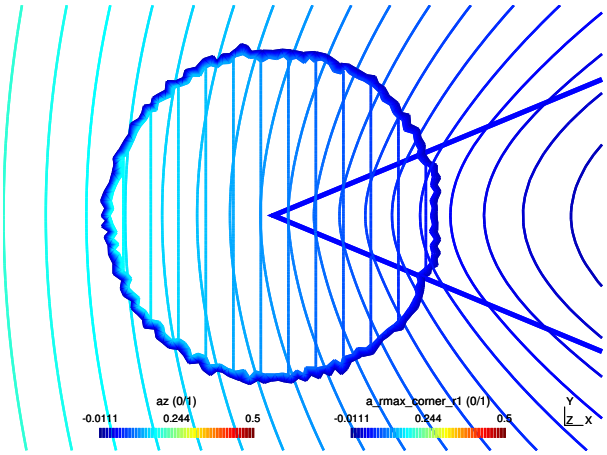

(a) Expansion restricted to composite order 1. Real part.

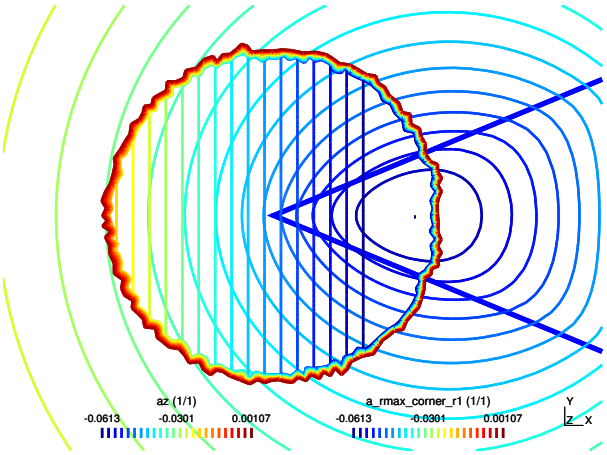

(b) Expansion restricted to composite order 1. Imaginary part.

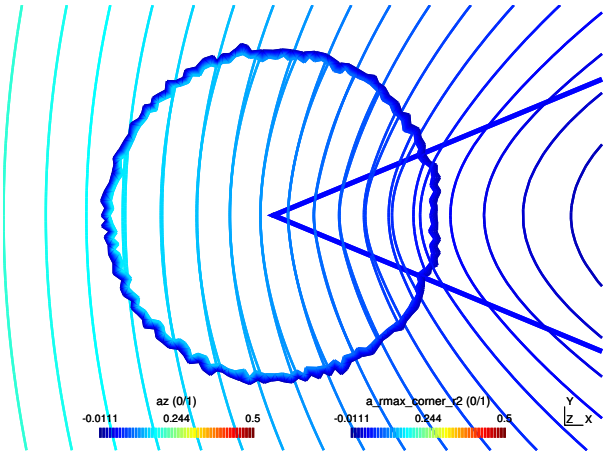

(c) Expansion restricted to composite order 2. Real part.

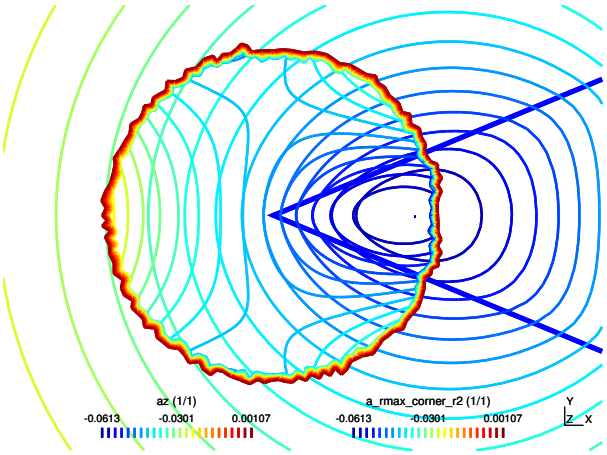

(d) Expansion restricted to composite order 2. Imaginary part.

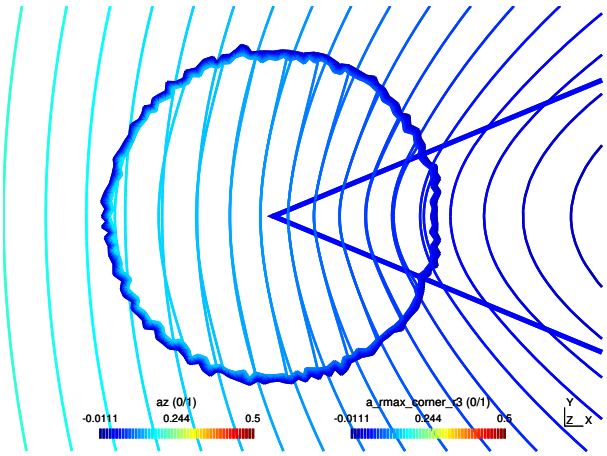

(e) Expansion restricted to composite order 3. Real part.

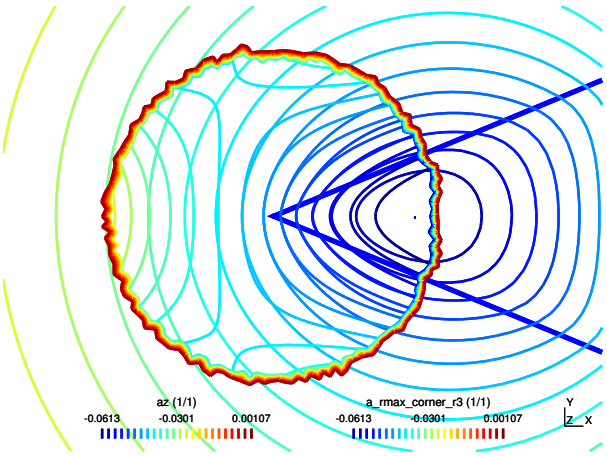

(f) Expansion restricted to composite order 3. Imaginary part.

FIGURE 5. Comparison of the finite element solution and of the local expansion.

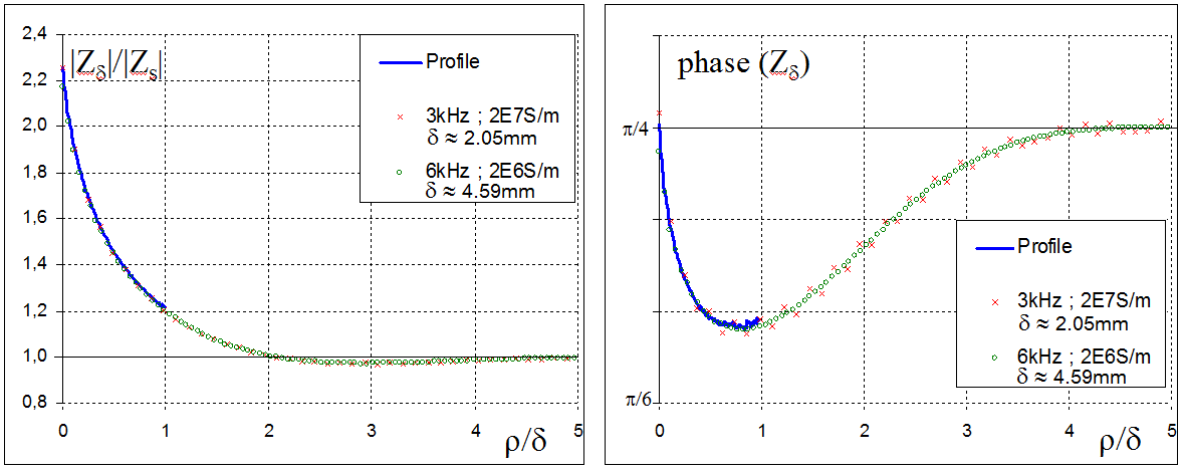

FIGURE 6. Behavior of $Z_\delta/|Z_s|$ vs ρ/δ. The domain characteristic length L is here 0.1m, then δ/L is between 2 and 4.6% for the considered situations.

3. Concluding remarks and publications related to the chapter

In this chapter, we have presented asymptotics results for two different problems: the steady-state potential in domain with rough thin layer of periodic roughness and the eddy current problem in domain with corner singularity.

For each problem, we exhibit profile terms which satisfy a PDE either in a thin perdiodic strip, for the rough thin layer, or in the whole plan $\mathbb{R}^2$ for the eddy current problem. We also provide the corner asymptotics of the magnetic potential in the case of given conductivity for the eddy current problem. Numerical simulations that corroborate the theoretical reasoning play a crucial role in the transmission of our results to the electrical engineering community.

Even though my main interests are now focused on mathematical biology, and on modeling, I would like to continue the asymptotics results towards two directions:

- First, it is important to provide rigorous justification of the asymptotic expansion of the eddy current problem as δ goes to zero. The theoretical tools should be similar to the tools used in G. Vial's PhD thesis [115], and also presented in [18]. Roughly speaking, Mellin transform and the use of exponential decay of the solution in the conducting domain should be used to justify the expansion of $\mathcal{A}_\delta$.
- The second research subject that I would like to consider deals with asymptotically close corners for the steady state problem. In particular it is interesting for eletrical considerations to understand how the gradient of the potential behaves near the corners as the distance between the corner goes to zero.

3.1. Publications related to this chapter.

3.1.a. *Publications related to rough thin layers.*

- **Poignard, C.** (2009), *Approximate transmission conditions through a weakly oscillating thin layer*, Math.Meth.Appl.Sci., 32(4):435-453.
- Ciuperca, I. S.; Perrussel, R.; **Poignard, C.** & Saut, O. (2010), *Influence of a Rough Thin Layer on the Potential*, IEEE Trans. on Mag., 46(8):2823-2826.
- Ciuperca, I. S.; Perrussel, R.; **Poignard, C.** & Saut, O. (2010), *Approximate Transmission Conditions through a rough thin layer. The case of the periodic roughness*, EJAM, 21(1):51-75.
- Ciuperca, I. S.; Perrussel, R.; **Poignard, C.** & Saut, O. (2011), *Two-scale analysis for very rough thin layers. An explicit characterization of the polarization tensor*, JMPA, 95(3):227-295.
- **Poignard, C.** (2011), *Explicit characterization of the polarization tensor for rough thin layers*, EJAM, 22:1-6.

- **Poignard, C.** (2013), *Boundary Layer Correctors and Generalized Polarization Tensor for Periodic Rough Thin Layers. A Review for the Conductivity Problem*, ESAIM:Proceedings, 37:136-165.

3.1.b. *Publications related to corner singularities.*

- Krähenbühl, L.; Buret, F.; Perrussel, R.; Voyer, D.; Dular, P.; Péron, V.; **Poignard, C.** (2011) *Numerical treatment of rounded and sharp corners in the modeling of 2D electrostatic fields*, J.Microwaves and OptoElectroMag. , 10(1):66-81.
- Buret, F, Dauge, M.; Dular, P.; Krähenbühl, L.; Péron, V.; Perrussel, R.; **Poignard, C.**; Voyer, D. (2012) *Eddy currents and corner singularities*, IEEE Trans. on Mag., 48(2):679-682.
- Dauge, M.; Dular, P.; Krähenbühl, L.; Péron, V.; Perrussel, R.; **Poignard, C.** (2013) *Corner asymptotics of the magnetic potential in the eddy-current model*, Math.Meth.Appl.Sci., published on-line.

Publications

Submitted Preprints.

- Joie, J.; Y. Lei; Colin, T.; Durrieu, M.-C.; **Poignard, C.** & Saut, O. (2013), *Modeling of migration and orientation of endothelial cells on micropatterned polymers*, Inria-RR 8252, Submitted.
- Leguèbe, M., **Poignard, C.** & Weynans, L., (2013), *"A second Order Cartesian Method for the simulation of electropermeabilization cell models*, Inria Research Report RR-8302, Submitted.
- Colin, T., Gallinato, O., **Poignard, C.**, Saut, O. (2014), *Tumor growth model for ductal carcinoma: from* **in situ** *phase to stroma invasion.* Inria Research Report RR–8502, Submitted.

Accepted or published papers.

(24) Leguèbe, M., Silve, A., Mir, L.M, & **Poignard, C.**, (2014) *Conducting and Permeable States Membrane Submitted to High Voltage Pulses. Mathematical and Numerical Studies Validated by the Experiments*, Inria Research Report RR-8496, Accepted in Jnl. Th. Biol.

(23) **Poignard, C.** & Silve, A. (2014), *Différence de potentiel transmembranaire des cellules biologiques*, Revue 3EI, n^{o}75.

(22) Duruflé, M., Péron, V. & **Poignard, C.** (2014), *Thin layers in electromagnetism*, To appear in CiCP. http://www.dx.doi.org/10.4208/cicp.120813.100114a.

(21) Perrussel, R. & **Poignard, C.** (2013), *Asymptotic Expansion of Steady-State Potential in a High Contrast Medium with a Thin Resistive Layer*, Applied Mathematics and Computation, 221:48-65.

(20) Colin, T.; Durrieu, M.-C.; Joie, J.; Lei, Y.; Mammeri, Y.; **Poignard, C.** & Saut, O. (2013), *Modelling of the migration of endothelial cells on bioactive micropatterned polymers*, Math. BioSci. Eng., 10(4):997-1015.

(19) **Poignard, C.** (2013), *Boundary Layer Correctors and Generalized Polarization Tensor for Periodic Rough Thin Layers. A Review for the Conductivity Problem*, ESAIM:Proceedings, 37:136-165.

(18) Dauge, M.; Dular, P.; Krähenbühl, L.; Péron, V.; Perrussel, R.; **Poignard, C.** (2013) *Corner asymptotics of the magnetic potential in the eddy-current model*, Math.Meth.Appl.Sci., published on-line.

(17) Buret, F, Dauge, M.; Dular, P.; Krähenbühl, L.; Péron, V.; Perrussel, R.; **Poignard, C.**; Voyer, D. (2012) *Eddy currents and corner singularities*, IEEE Trans. on Mag., 48(2):679-682.

(16) Kavian, O.; Leguèbe, M.; **Poignard, C.** & Weynans, L. (2012), *"Classical" electropermeabilization modeling at the cell scale*, Journal of Mathematical Biology.

(15) Ciuperca, I. S.; Perrussel, R.; **Poignard, C.** & Saut, O. (2011), *Two-scale analysis for very rough thin layers. An explicit characterization of the polarization tensor*, JMPA, 95(3):227-295.

(14) **Poignard, C.** (2011), *Explicit characterization of the polarization tensor for rough thin layers*, EJAM, 22:1-6.

(13) **Poignard, C.** (2009), *About the transmembrane voltage potential of a biological cell in time-harmonic regime*, ESAIM: Proceedings, 26:16-179.

(12) Cindea, N.; Fabrèges, B.; De Gournay, F. & **Poignard, C.** (2010), *Optimal placement of electrodes in an electroporation process*, ESAIM: Proceedings, 30:34-43.

(11) Duruflé, M.; Péron, V. & **Poignard, C.** (2011), *Time-harmonic Maxwell equations in biological cells. The differential form formalism to treat the thin layer*, Confluentes Mathematici, 3(2): 325-357.

(10) **Poignard, C.**; Silve, A.; Campion, F.; Mir, L., M.; Saut, O. & Schwartz, L. (2011), *Ion flux, transmembrane potential, and osmotic stabilization: A new electrophysiological dynamic model for Eukaryotic cells*, European Biophysics Journal, 40(3): 235-246.

(9) Krähenbühl, L.; Buret, F.; Perrussel, R.; Voyer, D.; Dular, P.; Péron, V.; **Poignard, C.** (2011) *Numerical treatment of rounded and sharp corners in the modeling of 2D electrostatic fields*, J.Microwaves and OptoElectroMag. , 10(1):66-81.

(8) Ciuperca, I. S.; Perrussel, R.; **Poignard, C.** & Saut, O. (2010), *Influence of a Rough Thin Layer on the Potential*, IEEE Trans. on Mag., 46(8):2823-2826.

(7) Ciuperca, I. S.; Perrussel, R.; **Poignard, C.** & Saut, O. (2010), *Approximate Transmission Conditions through a rough thin layer. The case of the periodic roughness*, EJAM, 21(1):51-75.

(6) **Poignard, C.** (2009), *Approximate transmission conditions through a weakly oscillating thin layer*, Math.Meth.Appl.Sci., 32(4):435-453.

(5) **Poignard, C.** (2008), *Asymptotics for steady state voltage potentials in a bidimensional highly contrasted medium with thin layer*, Math.Meth.Appl.Sci., 31(4):443-479.

(4) **Poignard, C.** (2007), *Generalized impedance boundary condition at high frequency for a domain with thin layer: the circular case.*, Appl. Anal., 86(12):1549-1568

(3) **Poignard, C.** , Dular, P.; Perrussel,R.; Krähenbühl, L.; Nicolas, L.; Schatzman, M. (2008) *Approximate conditions replacing thin layers*, IEEE Trans on Mag. , 44(6):1154-1157.

(2) Hansen, D.J.; **Poignard, C.**; Vogelius, M.S. (2007), *Asymptotically precise norm estimates of scattering from a small circular inhomogeneity.*, Appl. Anal., 86(4):433-458.

(1) Perrussel,R.; Nicolas, L.; Musy, F.; Krähenbühl, L.; Schatzman, M.; **Poignard, C.** (2006) *Approximate conditions replacing thin layers*, IEEE Trans on Mag. , 44(6):1154-1157.

Bibliography

[1] T. Abboud and H. Ammari. Diffraction at a curved grating: TM and TE cases, homogenization. *J. Math. Anal. Appl.*, 202(3):995–1026, 1996.

[2] Y. Achdou and O. Pironneau. Domain decomposition and wall laws. *C. R. Acad. Sci. Paris Sér. I Math.*, 320(5):541–547, 1995.

[3] G. Allaire and M. Amar. Boundary layer tails in periodic homogenization. *ESAIM Control Optim. Calc. Var.*, 4:209–243 (electronic), 1999.

[4] M. Amar, D. Andreucci, P. Bisegna, and R. Gianni. A hierarchy of models for the electrical conduction in biological tissues via two-scale convergence: the nonlinear case. *Differential Integral Equations*, 26(9-10):885–912, 2013.

[5] D. Ambrosi and L. Preziosi. On the closure of mass balance models for tumor growth. *Mathematical Models and Methods in Applied Sciences., Vol. 12, No. 5*, pages 737–754, 2002.

[6] H. Ammari and H. Kang. *Reconstruction of Small Inhomogeneities from Boundary Measurements*. Lecture Notes in Mathematics, No. 1846. Springer-Verlag, Berlin, 2004.

[7] H. Ammari and H. Kang. *Polarization and moment tensors*, volume 162 of *Applied Mathematical Sciences*. Springer, New York, 2007. With applications to inverse problems and effective medium theory.

[8] A. Basson and D. Gérard-Varet. Wall laws for fluid flows at a boundary with random roughness. *Comm. Pure Applied Math.*, 61(7), 2008.

[9] R. Benz, F. Beckers, and U. Zimmermann. Reversible electrical breakdown of lipid bilayer membranes: a charge pulse relaxation study. *J. Memb. Biol.*, 48(2):181–204, 1979.

[10] E. Beretta and E. Francini. Asymptotic formulas for perturbations in the electromagnetic fields due to the presence of thin inhomogeneities. In *Inverse problems: theory and applications (Cortona/Pisa, 2002)*, volume 333 of *Contemp. Math.*, pages 49–62. Amer. Math. Soc., Providence, RI, 2003.

[11] E. Beretta, E. Francini, and M. S. Vogelius. Asymptotic formulas for steady state voltage potentials in the presence of thin inhomogeneities. A rigorous error analysis. *J. Math. Pures Appl. (9)*, 82(10):1277–1301, 2003.

[12] F. Billy, B. Ribba, O. Saut, H. Morre-Trouilhet, T. Colin, D. Bresh, J-P. Boissel, E. Grenier, and J-P. Flandrois. A pharmacologically based multiscale mathematical model of angiogenesis and its use in investigating the efficacy of a new cancer treatment strategy. *J Theor Biol., 260(4)*, pages 545–562, 2009.

[13] M.J. Bissell and W.C. Hines. Why don't we get more cancer ? A proposed role of the microenvironment in restrainning cancer progression. *Nat Med., 17*, pages 320–329, 2011.

[14] D. Bresch, T. Colin, E. Grenier, B. Ribba, and O. Saut. A viscoelastic model for avascular tumor growth. *Discrete and continuous dynamical systems, supplement 2009*, pages 101–108, 2009.

[15] D. Bresch, T. Colin, E. Grenier, B. Ribba, and O. Saut. Computational modeling of solid tumor growth : the avascular stage. *SIAM Journal on Scientific Computing, 32(4)*, pages 2321–2344, 2010.

[16] O. Brummer, S. Athar, L. Riethdorf, T. Löning, and H. Herbst. Matrix-metallo-proteinases 1, 2 and 3 and their tissue inhibitors 1 and 2 in benign and malignant breast lesions : an in situ hybridization study. *Virchows Arch., 435*, pages 566–573, 1999.

[17] F. Buret, M. Dauge, P. Dular, L. Krähenbühl, V. Peron, R. Perrussel, C. Poignard, and D. Voyer. Eddy currents and corner singularities. *Magnetics, IEEE Transactions on*, 48(2):679–682, Feb 2012.

[18] Gabriel Caloz, Martin Costabel, Monique Dauge, and Grégory Vial. Asymptotic expansion of the solution of an interface problem in a polygonal domain with thin layer. *Asymptot. Anal.*, 50(1-2):121–173, 2006.

[19] Y. Capdeboscq and M. S. Vogelius. A general representation formula for boundary voltage perturbations caused by internal conductivity inhomogeneities of low volume fraction. *M2AN Math. Model. Numer. Anal.*, 37(1):159–173, 2003.

[20] Y. Chen, B.C. Lagerholm, B. Yang, and K. Jacobson. Methods to measure the lateral diffusion of membrane lipids and proteins. *Methods*, 39(2):147–153, 2006.

[21] M.A. Cichon, A.C. Degnim, D.W. Visscher, and D.C. Radisky. Microenvironmental influences that drive progression from benign breast disease to invasive breast cancer. *J Mammary Gland Biol Neoplasia, 15*, pages 389–397, 2010.

[22] M. Cisternino and L. Weynans. A parallel second order cartesian method for elliptic interface problems. *Commun. Comput. Phys.*, 12, 2012.

[23] I.S. Ciuperca, M. Jai, and C. Poignard. Approximate transmission conditions through a rough thin layer. The case of periodic roughness. *Euro. Jnl of Applied Mathematics*, 21(1):51–75, 2010.

[24] I.S. Ciuperca, R. Perrussel, and C. Poignard. Influence of a Rough Thin Layer on the Steady-state Potential. *IEEE Trans. on Mag.*, 46(8), 2010.

[25] I.S. Ciuperca, R. Perrussel, and C. Poignard. Two-scale analysis for very rough thin layers. An explicit characterization of the polarization tensor. *Journal de Mathématiques Pures et Appliquées*, 95(3):277–295, 2011.

[26] T. Colin, M.-C. Durrieu, J. Joie, Y. Lei, Y. Mammeri, C. Poignard, and O. Saut. Modeling of the migration of endothelial cells on bioactive micropatterned polymers. *Mathematical biosciences and engineering*, to appear, 2012.

[27] T. Colin, M.-C. Durrieu, J. Joie, Y. Lei, Y. Mammeri, C. Poignard, and O. Saut. Modelling of the migration of endothelial cells on bioactive micropatterned polymers. *Mathematical Biosciences and Engineering*, 10(4):997–1015, 2013.

[28] T. Colin, O. Gallinato, C. Poignard, and O. Saut. Tumor growth model for ductal carcinoma: from **in situ** phase to stroma invasion. Inria Research report RR–8502, Submitted, 2014.

[29] Piero Colli Franzone and Giuseppe Savaré. Degenerate evolution systems modeling the cardiac electric field at micro- and macroscopic level. In *Evolution equations, semigroups and functional analysis (Milano, 2000)*, volume 50 of *Progr. Nonlinear Differential Equations Appl.*, pages 49–78. Birkhäuser, Basel, 2002.

[30] M. Costabel, M. Dauge, and Z. Yosibash. A quasidual function method for extracting edge stress intensity functions. *SIAM Jour. Math. Anal.*, 35(5):1177–1202, 2004.

[31] Monique Dauge, Patrick Dular, Laurent Krähenbühl, Victor P´ eron, Ronan Perrussel, and Clair Poignard. Corner asymptotics of the magnetic potential in the eddy-current model. *Mathematical Methods in the Applied Sciences*, 2013.

[32] K. DeBruin and W. Krassowska. Modelling electroporation in a single cell. I. Effects of field strength and rest potential. *Biophys. J.*, 77(3):1213–1224, 1999.

[33] D. Drasdo, S. Dormann, S. Hoehme, and A. Deutsch. Cell-based models of avascular tumor growth. In *Function and Regulation of Cellular Systems*, Mathematics and Biosciences in Interaction, pages 367–378. Birkhäuser Basel, 2004.

[34] D. Drasdo and S. Höhme. A single-cell-based model of tumor growth in vitro: monolayers and spheroids. *Phys Biol., 2*, pages 133–147, 2005.

[35] M.J. Duffy, T.M. Maguire, A. Hill, and E. McDermott. Metalloproteinases: role in breast carcinogenesis, invasion and metastasis. *Breast Cancer Res., 2*, pages 252–257, 2000.

[36] Marc Duruflé, Victor Péron, and Clair Poignard. Time-harmonic Maxwell equations in biological cells—the differential form formalism to treat the thin layer. *Confluentes Math.*, 3(2):325–357, 2011.

[37] Marc Duruflé, Victor Péron, and Clair Poignard. Thin layer models for electromagnetism. *To appear in CiCP*, 2014.

[38] P. F. Fahey and W. W. Webb. Lateral diffusion in phospholipid bilayer membranes and multilamellar liquid crystals. *Biochemistry*, 17(15):3046–3053, 1978.

[39] E.C. Fear and M.A. Stuchly. Modelling assemblies of biological cells exposed to electric fields. *IEEE Trans Biomed Eng*, 45(10):1259–1271, Oct 1998.

[40] E.C. Fear and M.A. Stuchly. A novel equivalent circuit model for gap-connected cells. *Phys Med Biol*, 43(6):1439–1448, Jun 1998.

[41] American Society for Cell Biology. Externally applied forces can phenotypically revert malignant breast epithelial structures. In *ASCB, 2012 annual meeting abstracts*, pages 983, No.1673, Dec 17, 2012. http://www.ascb.org/files/Past-AM-Meetings/2012_Abstracts.pdf.

[42] K.R. Foster and H.P. Schwan. Dielectric properties of tissues and biological materials: a critical review. *CRC in Biomedical Engineering*, 17(1):25–104, 1989.

[43] S.J. Franks, H.M. Byrne, J.R. King, J.C.E. Underwood, and C.E. Lewis. Modelling the early growth of ductal carcinoma in situ of the breast. *J Math Biol., 47*, pages 424–452, 2003.

[44] C. Geuzaine and J. F. Remacle. Gmsh a three-dimensional finite element mesh generator with built-in pre- and post-processing facilities. *International Journal for Numerical Methods in Engineering*, 79:1309, 31, 2009.

[45] M. Glogauer, W. Lee, and C.A.G. McCulloch. Induced endocytosis in human fibroblasts by electrical fields. *Exp. Cell Res.*, 208(1):232 – 240, 1993.

[46] Grégory Guyomarc'h, Chang-Ock Lee, and Kiwan Jeon. A discontinuous Galerkin method for elliptic interface problems with application to electroporation. *Comm. Numer. Methods Engrg.*, 25(10):991–1008, 2009.

[47] A. Hamaï, J. Muret, A. Cavalcanti, S. Bonvalot, and S. Chouaïb. Le facteur de nécrose tumorale : de la biologie à la thérapie oncologique. *Hématologie, 15(4)*, pages 291–304, 2009.

[48] S. Harakawa, N. Inoue, T. Hori, K. Tochio, T. Kariya, K. Takahashi, F. Doge, H. Suzuki, and H. Nagasawa. Effects of a 50 hz electric field on plasma lipid peroxide level and antioxidant activity in rats. *Bioelectromagnetics*, 26(7):589–594, 2005.

[49] M. Hu and K. Polyak. Microenvironmental regulation of cancer development. *Curr Opin Genet Dev., 18(1)*, pages 27–34, 2008.

[50] M. Hu, J. Yao, D.K. Carroll, S. Weremowicz, H. Chen, D. Carrasco, A. Richardson, S. Violette, T. Nikolskaya, Y. Nikolsky, E. Bauerlein, W.C. Hahn, R.S. Gelman, C. Allred, M.J. Bissel, S. Schnitt, and K. Polyak. Regulation of in situ to invasive breast carcinoma transition. *Cancer Cell, 13*, pages 394–406, 2008.

[51] Tatsuo Iguchi. On the irrotational flow of incompressible ideal fluid in a circular domain with free surface. *Publ. Res. Inst. Math. Sci.*, 34(6):525–565, 1998.

[52] A. Ivorra, J. Villemejane, and L.M. Mir. Electrical modeling of the influence of medium conductivity on electroporation. *Physical Chemistry Chemical Physics*, 12(34):10055–10064, 2010.

[53] W. Jäger, A. Mikelić, and N. Neuss. Asymptotic analysis of the laminar viscous flow over a porous bed. *SIAM J. Sci. Comput.*, 22(6):2006–2028 (electronic), 2000.

[54] J. Joie, Y. Lei, T. Colin, M.-C. Durrieu, C. Poignard, and O. Saut. Modeling of migration and orientation of endothelial cells on micropatterned polymers: a simple model based on classical mechanics approach. *Inria Research Report RR-8252. Submitted*, 2013.

[55] M. Kargol. A more general form of Kedem and Katchalsky's practical equations. *J. Biol. Phys.*, 22(1):15–26, 1996.

[56] O. Kavian, M. Leguèbe, C. Poignard, and L. Weynans. "Classical" Electropermeabilization Modeling at the Cell Scale. *Journal of Mathematical Biology*, 2012.

[57] F.W. Kleinhans. Membrane permeability modeling : Kedem-Katchalsky vs a two-parameter formalism. *Cryobiology, 37*, pages 271–289, 1998.

[58] A. Köhrmann, U. Kammerer, M. Kapp, J. Dietl, and J. Anacker. Expression of matrix metalloproteinases (MMPs) in primary human breast cancer and breast cancer cell lines: new findings and review of the literature. *BMC Cancer, 9:188*, 2009.

[59] V. A. Kondratiev. Boundary value problems for elliptic equations in domains with conical or angular points. *Trudy Moskov. Mat. Obšč.*, 16:209–292, 1967.

[60] Jens H Kroeger, Dan Vernon, and Martin Grant. Curvature-driven pore growth in charged membranes during charge-pulse and voltage-clamp experiments. *Biophysical journal*, 96(3):907–916, February

2009. PMID: 19186129.
[61] M. Leguèbe, C. Poignard, and L. Weynans. A second-order Cartesian method for the simulation of electropermeabilization cell models. Research report RR-8302, INRIA, 2013.
[62] M. Leguèbe, A. Silve, L.M. Mir, and C. Poignard. Conducting and permeable states of cell membrane submitted to high voltage pulses. mathematical and numerical studies validated by the experiments. Inria Research Report RR-8496, 2014.
[63] Y. Lei. *Biochemical and microscale modification of polymer for endothelial cell angiogenesis*. PhD thesis, Université Bordeaux 1, 2012.
[64] Y. Lei, O.F. Zouani, L. Rami, C. Chanseau, and M.-C. Durrieu. Modulation of lumen formation by microgeometrical bioactive cues and migration mode of actin machinery. *Small*, doi:10.1002/smll.201202410, 2012.
[65] M. A. Leontovitch. Approximate boundary condition for the electromagnetic field on the surface of a good conductor. *Investigations on Radiowave Propagation, PtII, Printing House of the Acad. of Science*, pages 5–12, 1948.
[66] A-C. Lesart, B. van der Sanden, L. Hamard, F. Estève, and A. Stéphanou. On the importance of the submicrovascular network in a computational model of tumour growth. *Microvascular Research, 84*, pages 188–204, 2012.
[67] P. Macklin, M.E. Edgerton, A.M. Thompson, and V. Cristini. Patient-calibrated agent-based modelling of ductal carcinoma in situ (DCIS) : from microscopic measurements to macroscopic predictions of clinical progression. *J Theor Biol., 301*, pages 122–140, 2012.
[68] M. Meyer, A. Barr, H. Lee, and M. Desbrun. Generalized barycentric coordinates on irregular polygons. *J. Graph. Tools*, 7(1):13–22, 2002.
[69] D. Miklavčič, D. Šermov, H. Mekid, and L.M. Mir. A validated model of in vivo electric field distribution in tissues for electrochemotherapy and for DNA electrotransfer for gene therapy. *Biochimica et Biophysica Acta*, 1523:73–83, 2000.
[70] C. Min and F. Gibou. A second order accurate level set method on non-graded adaptive cartesian grids. *Journal of Computational Physics*, 225:300–321, 1997.
[71] L.M. Mir. Therapeutic perspectives of *in vivo* cell electropermeabilization. *Bioelectrochemistry*, 53:1–10, 2001.
[72] J. Neu and W. Krassowska. Asymptotic model of electroporation. *Physical Review E*, 53(3):3471–3482, Mar 1999.
[73] E. Neumann. Membrane electroporation and direct gene transfer. *Bioelectrochemistry and Bioenergetics*, 1992.
[74] B. Nikolova, M. Georgieva, D. Savu, and I. Tsoneva. Cell membrane alteration by weak alternating electric field at low frequency. *Rom. Rep. Phys.*, 64(4):1046–1052, 2012.
[75] Breast Pathology on the Web, May 2013. Website : www.breastpathology.info.
[76] C. Osborne, P. Wilson, and D. Tripathy. Oncogenes and tumor suppressor genes in breast cancer: potential diagnostic and therapeutic applications. *The Oncologist, 9*, pages 361–377, 2004.
[77] S. Osher and J. A. Sethian. Fronts propagating with curvature-dependent speed: Algorithms based on hamilton-jacobi formulations. *J. Comput. Phys.*, 79(12), 1988.
[78] C.M. Overall and C. López-Otín. Strategies for MMP inhibition in cancer: innovations for the post-trial era. *Nat Rev Cancer, Vol. 2*, pages 657–672, 2002.
[79] V. Péron. *Description de l'effet de peau par un développement asymptotique*. PhD thesis, Université Rennes 1, 2009. In preparation.
[80] R. Perrussel and C. Poignard. Asymptotic expansion of steady-state potential in a high contrast medium with a thin resistive layer. *Applied Mathematics and Computation*, pages 48–65, 2013.
[81] R. Perrussel and C. Poignard. Asymptotic expansion of steady-state potential in high contrast medium with a thin resisitive layer. *ACM*, 221:997–1015, 2013.
[82] C. Poignard. About the transmembrane voltage potential of a biological cell in time-harmonic regime. *ESAIM: Proceedings*, 26:162–179, 2009.
[83] C. Poignard. Approximate transmission conditions through a weakly oscillating thin layer. *Math. Meth. App. Sci.*, 32(4):435–453, 2009.

[84] C. Poignard. Explicit characterization of the polarization tensor for rough thin layers. *European J. Appl. Math.*, 22(1):1–6, 2011.
[85] C. Poignard. Boundary Layer Correctors and Generalized Polarization Tensor for Periodic Rough Thin Layers. A Review for the Conductivity Problem. *ESAIM: Proceedings*, 37:136–165, 2012.
[86] C. Poignard and A. Silve. Différence de potentiel induite par un champ électrique sur la membrane d'une cellule biologique. *La Revue 3EI*, 75:11–20, 2014. http://www.hal.inria.fr/hal-00977590.
[87] T. Portet and R. Dimova. A new method for measuring edge tensions and stability of lipid bilayers: effect of membrane composition. *Biophys. J.*, 84:3263–3273, 2010.
[88] G. Pucihar, T. Kotnik, M. Kanduer, and D. Miklavčič. The influence of medium conductivity on electropermeabilization and survival of cells in vitro. *Bioelectrochemistry*, 54(2):107–115, Nov 2001.
[89] G. Pucihar, T. Kotnik, B. Valič, and D. Miklavčič. Numerical determination of transmembrane voltage induced on irregularly shaped cells. *Ann Biomed Eng*, 34(4):642–652, Apr 2006.
[90] Y. Renard and J. Pommier, 2010. Getfem finite element library. *http://home.gna.org/getfem*.
[91] S.Y. Rha, J.H. Kim, J.K. Roh, K.S. Lee, J.S. Min, B.S. Kim, and H.C. Chung. Sequential production and activation of matrix-metalloproteinase-9 (MMP-9) with breast cancer progression. *Breast Cancer Researsh and Treatment, 43*, pages 175–181, 1997.
[92] B. Ribba, O. Saut, T. Colin, D. Bresh, E. Grenier, and J-P. Boissel. A multiscale mathematical model of avascular tumor growth to investigate the therapeutic benefit of anti-invasive agents. *J Theor Biol., 243(4)*, pages 532–541, 2006.
[93] M.P. Rols, C. Delteil, M. Golzio, and J. Teissié. Control by ATP and ADP of voltage-induced mammalian-cell-membrane permeabilization, gene ransfer and resulting expression. *Eur. J. of Biochem.*, 254(2):382–388, 1998.
[94] R. Ryham, I. Berezovik, and F.S. Cohen. Aqueous viscosity is the primary source of friction in lipidic pore dynamics. *Biophys. J.*, 101, 2011.
[95] R.A. Sakr. Carcinomes canalaires in situ du sein : rôle potentiel de la biologie moléculaire. *Gynécologie Obstétrique & Fertilité, 41*, pages 45–53, 2012.
[96] O. Sandre, L. Moreaux, and F. Brochard-Wyart. Dynamics of transient pores in stretched vesicles. *Proc. Natl. Acad. Sci*, 96:10591–10596, 1999.
[97] S. Šatkauskas, F.M. André, M.F. Bureau, D. Scherman, D. Miklavčič, and L.M. Mir. Electrophoretic component of electric pulses determines the efficacy of in vivo DNA electrotransfer. *Hum. Gene Ther.*, 16(10):1194–1201, 2005.
[98] G. Serša. Application of electroporation in electrochemotherapy of tumors. In *Electroporation based Technologies and Treatment: proceedings of the international scientific workshop and postgraduate course*, pages 42–45, 14-20 November 2005. Ljubljana, SLOVENIA.
[99] S. Shannon, Z. Yosibash, M. Dauge, and M. Costabel. Extracting generalized edge flux intensity functions by the quasidual function method along circular 3-d edges. Preprint HAL available at http://hal.archives-ouvertes.fr/hal-00725928., 2012.
[100] A. Silve, A. Giumerà Brunet, A. Ivorra, and L.M. Mir. Comparison of the effects of the repetition rate between microsecond and nanosecond pulses: Electropermeabilisation-induced electro-desensitization? Submitted, 2014.
[101] M.A. Stuchly and S.S. Stuchly. Electrical properties of biological substances. *Biological Effects and Medical Applications of Electromagnetic Energy*, 1990.
[102] S.I. Sukharev, V.A Klenchin, S.M. Serov, Chernomordik L.V., and Chizmadzhev Y.A. Electroporation and electrophoretic DNA transfer into cells: The effect of DNA interaction with electropores. *Biophys J.*, 63:1320–1327, 1992.
[103] V.L. Sukhoroukov, H. Mussauer, and U. Zimmermann. The effect of electrical deformation forces on the electropermeabilization of erythrocyte membranes in low- and high-conductivity media. *Journal of Membrane Biology*, 1998.
[104] M. Tarek. Membrane Electroporation: A Molecular Dynamics Simulation. *Biophys. J.*, 88(6):4045–4053, 2005.
[105] J. Teissié, M. Golzio, and M.P. Rols. Mechanisms of cell membrane electropermeabilization: A minireview of our present (lack of?) knownledge. *Biochimica et Biophysica Acta*, 1724:270–280, 2005.

[106] J. Teissié and C. Ramos. Correlation between Electric Field Pulse Induced Long-Lived Permeabilization and Fusogenicity in Cell Membranes. *Biophys. J.*, 74(4):1889–1898, 1998.
[107] D. Thanoon. *Computational framework for local breast cancer treatment.* PhD thesis, Université de Bordeaux 1 & University of Houston, 2011.
[108] D.P. Tieleman. The molecular bases of electroporation. *BMC Biochem.*, 5(10):1–12, 2004.
[109] J.-F. Tocanne, L. Dupou-Cézanne, and A. Lopez. Lateral diffusion of lipids in model and natural membranes. *Prog. Lip. Res.*, 33(3):203–237, 1994.
[110] T.-H. Tsai. Simulations of endothelial cells clusters migration in angiogenesis. *The SIJ Transactions on Computer Science Engineering & its Applications (CSEA)*, 1(4):111–115, 2013.
[111] J.M. Tse, G. Cheng, J.A. Tyrrell, S.A. Wilcox-Adelman, Y. Boucher, R.K. Jain, and L.L. Munn. Mechanical compression drives cancer toward invasive phenotype. *PNAS, Vol.109, No.3*, pages 911–916, Jan 2012.
[112] T.Y. Tsong. Electroporation of cell membranes. *Biophys J.*, 60:297–306, 1991.
[113] Johns Hopkins Medicine (Johns Hopkins University), Oct 2013. http://pathology.jhu.edu/breast/diagnosis.php.
[114] W.L.C. Vaz, F. Goodsaid-Zalduondo, and K. Jacobson. Lateral diffusion of lipids and proteins in bilayer membranes. *FEBS Lett.*, 174(2):199–207, 1984.
[115] G. Vial. *Analyse multi-échelle et conditions aux limites approchées pour un problème avec couche mince dans un domaine à coin.* PhD thesis, Université Rennes1, Juin 2003. Thesis.
[116] D. Šel, D. Cukjati, D. Batiuskaite, T. Slivnik, L.M. Mir, and D. Miklavčič. Sequential finite element model of tissue electropermeabilization. *IEEE Trans. Bio. Eng.*, 52(5):816–827, 2005.
[117] A. Waterston and M. Bower. TNF and cancer : good or bad ? *Cancer Therapy, vol 2*, pages 131–148, 2004.
[118] J.C Weaver. Electroporation of cells and tissues. *IEEE Trans. on Plasma Sci.*, 28, 2000.
[119] J.C Weaver and Y.A. Chimazdzhev. Theory of electroporation: A review. *Bioelectrochemistry and Bioenergetics*, 41, 1996.
[120] L.H. Wegner, B. Flickinger, C. Eing, T. Berghoefer, P. Hohenberger, W. Frey, and P. Nick. A patch clamp study on the electro-permeabilization of higher plant cells: Supra-physiological voltages induce a high-conductance, k+ selective state of the plasma membrane. *Biochimica et Biophysica Acta*, 1808, 2011.
[121] S. Yang. To revert breast cancer cells, give them the squeeze. *UC Berkeley News Center*, Dec 17, 2012. http://newscenter.berkeley.edu/.